FABRICATION, CHARACTERIZATION, AND APPLICATION OF MICRORESONATORS AND RESONANT STRUCTURES

By

Gregory A. Cohoon

A Dissertation Submitted to the Faculty of the

DEPARTMENT OF OPTICAL SCIENCES

In Partial Fulfillment of the Requirements

For the Degree of

DOCTOR OF PHILOSOPHY

In the Graduate College

THE UNIVERSITY OF ARIZONA

2016

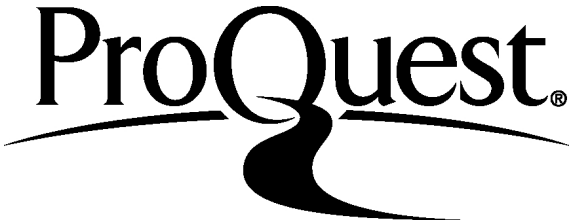

THE UNIVERSITY OF ARIZONA

GRADUATE COLLEGE

As members of the Dissertation Committee, we certify that we have read the dissertation prepared by Gregory Cohoon, titled Fabrication, Characterization, and Application of Microresonators and Resonant Structures and recommend that it be accepted as fulfilling the dissertation requirement for the Degree of Doctor of Philosophy.

_____

Robert A. Norwood Date: 12/17/2015

_____

Masud Mansuripur Date: 12/17/2015

_____

Khanh Kieu Date: 12/17/2015

Final approval and acceptance of this dissertation is contingent upon the candidate's submission of the final copies of the dissertation to the Graduate College.

I hereby certify that I have read this dissertation prepared under my direction and recommend that it be accepted as fulfilling the dissertation requirement.

_____

Date: 12/17/2015
Dissertation Director: Robert A. Norwood

STATEMENT BY AUTHOR

This dissertation has been submitted in partial fulfillment of the requirements for an advanced degree at the University of Arizona and is deposited in the University Library to be made available to borrowers under rules of the Library.

Brief quotations from this dissertation are allowable without special permission, provided that an accurate acknowledgement of the source is made. Requests for permission for extended quotation from or reproduction of this manuscript in whole or in part may be granted by the head of the major department or the Dean of the Graduate College when in his or her judgment the proposed use of the material is in the interests of scholarship. In all other instances, however, permission must be obtained from the author.

SIGNED: Gregory A. Cohoon

Acknowledgements and Dedication

I dedicate this work to my family and friends who have supported and my mentors who have encouraged me.

Table of Contents

Table of Figures

Abstract

Optical resonators are structures that allow light to circulate and store energy for a duration of time. This work explores the fabrication, characterization, and application of whispering gallery mode microresonators and the analysis of organic photonic crystal-like structures and simulation of their resonant effects.

Whispering gallery mode (WGM) microresonators are a class of cylindrically symmetric optical resonator which light circulates around the equator of the structure. These resonators are named after acoustic whispering galleries, where a whisper can be heard anywhere along the perimeter of a circular room. These optical structures are known for their ultra high Q-factor and their low mode volume. Q-factor describes the photon lifetime in the cavity and is responsible for the energy buildup within the cavity and sharp spectral characteristics of WGM resonators. The energy buildup is ideal for non-linear optics and the sharp spectral features are beneficial for sensing applications. Characterization of microbubble resonators is done by coupling light from a tunable laser source via tapered optical fiber into the cavity. The fabrication of quality tapered optical fiber on the order of 1-2 μm is critical to working on WGM resonators. The measurement of Q-factors up to $2x10^8$ and mode spectra are possible with these resonators and experimental techniques.

This work focuses on microdisk and microbubble WGM resonators. The microdisk resonators are fabricated by femtosecond laser micromachining. The micromachined resonators are fabricated by ablating rotating optical fiber to generate the disk shape and then heated to reflow the surface to improve optical quality. These resonators have a spares mode spectrum and display a Q factor as

high a $2x10^6$. The microbubble resonators are hollow microresonators fabricated by heating a pressurized capillary tube which forms a bubble in the area exposed to heat. These have a wall thickness of 2-5 μm and a diameter of 200-400 μm. Applications in pressure sensing and two-photon fluorescence of dye in microbubble resonators is explored.

Photonic crystals can have engineered resonant properties by tuning photonic band gaps and introducing defects to create cavities in the photonic structure. In this work, a natural photonic crystal structure is analyzed in the form of diatoms. Diatoms are a type of phytoplankton which are identified by unique ornamentation of each species silica shell, called a frustule. The frustule is composed of a quasi-periodic lattice of pores which closely resembles manmade photonic crystals. The diatom frustules are analyzed using image processing techniques to determine pore-to-pore spacing and identify defects in the quasi-periodic structure which may contribute to optical filtering and photonic band gap effects. The data gathered is used to simulate light propagation through the diatom structure at different incident angles and with different material properties and to verify data gathered experimentally

Chapter 1: Introduction to resonant structures

1.1 What are resonant structures

In recent years, resonant structures have become an important part of research in photonics and the field of non-linear optics[1–5]. Resonant structures, in an optical sense, are structures which can confine light and allow it to circulate for an extended period of time. The condition for resonance in an optical resonator is that the light field recreates itself in phase every round trip. This criteria allows for constructive interference in the cavity which leads to a build up of circulating light intensity[6].

Typically this is achieved by two parallel mirrors of a Fabry Perot cavity. This is the standard configuration of a free space laser cavity. Other free space, macroscale resonators, can be arranged in a bowtie, ring, or other complex configurations. Resonant structures can also exist on the microscale. This is achieved by patterning plasmonic materials or photonic crystal structures. Resonators more analogous to an optical cavity can be fabricated on the microscale in the shape of spheres, disks, bubbles, and toroids. This group of resonator geometries constitutes a class called whispering gallery mode resonators.

A typical application of optical resonators is to provide field enhancement to improve the efficiency of physical processes such as: fluorescence[7], multiphoton excitation, and Raman scattering[3,8]. They can also be used as optical sensors by measuring the microresonator's optical response to external

stimuli. These can be temperature, pressure, or biological[9–11]. Sensors made using optical resonators can make use of simple methods such as tracking the resonant frequency or analyzing Q-factor. For example, there are certain sensors which measure the Brillouin scattering of material surrounding the resonator to determine the properties and composition of the sample by measuring the speed of the acoustic waves propagating in the material[12,13].

1.2 Whispering gallery mode resonators

This thesis primarily considers a class of microresonators called whispering gallery microresonators. Whispering gallery microresonators are at minimum a cylindrically symmetric class of resonator in which light circulates about the equator of the resonator geometry. These geometries are typically: spheres, disks, toroids, or bubbles[14–16]. Linear resonators consist of a collection of mirrors to circulate the optical path; whispering gallery mode resonators, in a geometric sense, operate on total internal reflection of light between the glass-air interface. The confinement however is better described with a full treatment of Maxwell's Equations.

Whispering gallery mode resonators have been a current topic of research since the first major experiments on microsphere resonators in 1989[17]. These resonators were attractive due to their small size and extremely high Q-factor. This brought on a plethora of research investigating these structures to better understand the physics of whispering gallery mode resonators: coupling of light in and out of the resonators[18,19], what contributes to the Q-factor[20], and applications of the microsphere in non-linear optics and sensing[1,3,4,9]. Subsequent research began investigating other fabrication methods and resonator geometries. The most notable of these was the microtoroid resonator developed at

Caltech by K. Valhalla[21]. The microtoroid resonator is made lithographically and has a remarkably high Q-factor, small footprint, and is made on chip, which was further encouraged by lab-on-a-chip efforts.

1.3 What is the Q-factor

The Q-factor is a parameter that defines the damping of a resonant system. The Q-factor is a characteristic of any resonant system: a simple mass spring system, an RLC circuit, an optical microresonator, or even a bell. The concept of Q-factor can be viewed through two domains: time and frequency. In the time domain the Q-factor describes the response to an impulse. For example, striking a bell with a hammer transfers mechanical energy to the bell and it rings for some time as the energy is dissipated by the bell. The duration of the ringing is related to the Q-factor. In the frequency domain the Q-factor describes the bandwidth of an oscillator or a filter. In the optical domain this is the linewidth of the resonance and is defined as $Q = \frac{f}{\delta f}$.[14]

There are a few parameters which contribute to the Q-factor in a whispering gallery mode resonator. TIR at a flat interface is lossless; in a whispering gallery mode resonator things are slightly complicated as solving Maxwell's equations is necessary. When solving Maxwell's equations it is found that some of the energy is radiated. This is related to the intrinsic or geometric Q-factor of the resonator[14,15,20].

The other contributions are more straightforward. Surface scattering is a major contribution and is not included in the geometric Q-factor as it is typically not built in to the wave equation model. This typically comes from defects in manufacturing like scratches or debris deposited on the surface which is common

in micromachining fabrication in resonators. Surface scattering can also be engineered to reduce Q-factor by adding porous coatings to the surface.

The last notable contribution is material absorption. In order to have a high-Q whispering gallery mode cavity it is important to use low-loss materials. Glasses like fused silica (SiO_2) are typically used in microsphere resonators as the glass is easily available with ultra low loss the form of optical fiber. SiO_2 can also be readily deposited on surfaces and substrates for fabricating on chip resonators, such as microtoroid resonators[21]. Other materials often used are crystalline CaF_2, MgF_2, and $LiNbO_3$ in diamond turned microdisk resonators[4,22–24]. These resonators have extremely high Q-factors on the order of 10^{10} due to the remarkably low loss of the material[4,24]. They are also generally fabricated on the millimeter scale and as such have far less radiation loss since the bend radius is much larger than that of a micrometer scale microsphere[4,24]. Droplets of liquid can also be used as microresonators; some materials, such as ethanol, can provide remarkably high Q-factors, but a free space droplet resonator is not a robust platform for most experiments[25,26].

1.4 Biological photonic crystals

Photonic crystals are periodically patterned structures which allow the dispersion of light propagating through the photonic crystal structure to be tailored by manipulation of physical spacing and arrangement. The patterns can be altered by adding defects to confine light and create waveguides and resonant structures which exhibit significant enhancement in the defect area.

1.5 Outline of resonators discussed and applications

Microdisk resonators fabricated using femtosecond lasers are first looked at. This process is similar to that of a traditional mechanical lathe where a glass fiber is rotated about its symmetric axis and ablated to form a disk structure. The disk structure is then treated with a reflow process to smooth the surface and enhance the optical quality. Here we discuss the fabrication process and analysis of mode structure and improvement of the Q-factor of the resonator.

Second, microbubble resonators are examined. Microbubble resonators are a class of opto-fluidic resonators made from a thin walled fused silica capillary tube. The tube is pressurized and heated. The heat causes the walls to become molten and expand forming a bubble shape which is the basis for the resonator geometry. The resonator is demonstrated as a sensitive aerostatic pressure sensor and as a platform for non-linear optics in liquids.

Lastly, the concept of biological photonic crystals is explored. Diatoms are examined due to their shell which has a unique ornamentation of pores which resemble manmade photonic crystals. Our group has looked at the propagation of light experimentally. In this work digital image analysis of the diatom structure is performed to develop a better understanding of the potential photonic properties as well as biological properties of that derive from the shape of the diatom shells. These simulations are used to support experimental data. The structural data is also used to develop models of the diatom frustule which are suitable for simulation of light propagation using FDTD software. These FDTD simulations, performed with Lumerical FDTD software, closely match the experiments performed on diatom shells.

Digitally analyzing the images of diatom frustules also may allow us to pursue future work in understanding the biology of diatoms. Using this method, the morphology of the pore network of the diatom frustule can be quantitatively analyzed. This can potentially lead to better identification of diatom species and quantitatively describing the effects of environmental growth conditions which may cause deformities in a population of diatoms. These methods can be coupled with other imaging methods, such as multiphoton microscopy and fluorescence imaging, to extract further information about how the diatom's morphological structure may dictate its biology.

Chapter 2: Tapered optical fiber

2.1 Coupling into microresonators

To most effectively use a whispering gallery mode microresonator it is important to efficiently couple light into the microresonator by some means. There are a variety of methods for coupling light into a WGM resonator with the most common being prism coupling[17] and taper coupling[18,19,27]. Both methods involve generating an evanescent field whose propagation constant matches that of the whispering gallery mode supported by the resonator. In the prism coupling case, this is optimized by the angle of the incident laser light and its wavelength. Prism coupling is typically used for larger scale resonators and requires a complex alignment strategy as well as collection optics[23].

Taper coupling is performed by using an adiabatically tapered optical fiber. A tapered fiber is a fiber that has been pulled down to a thin radius on the order of a few micrometers. In standard optical fiber, light is guided by the index difference between the core and cladding. When the fiber is pulled down to the scale of a tapered fiber the light is now guided by the interface between the tapered waist (fused silica, index of 1.45) and the air. This causes the numerical aperture (NA) of the fiber to increase. The NA of optical fiber is defined as:

$$NA = \sqrt{n_{core}^2 - n_{cladding}^2} \qquad (2.1)$$

Typical communications fiber has an NA between .1 and .14, where for the tapered fiber case the NA can be as high as 1. This huge increase in NA can change

the number of modes supported by the optical fiber. The generalized frequency, or V-parameter, of the optical fiber is given by

$$V = \frac{2\pi}{\lambda} a\, NA \qquad (2.2)$$

In this equation *a,* is the radius of the core of the optical fiber. By examining this equation for high NA, we see that in order for the tapered optical fiber to support a single waveguide mode it is necessary for it to have a very small diameter taper. This can be unrealistic due to the fabrication limits of sub-micron tapers and by the necessity for suitable propagation constant matching of the tapered optical fiber and the WGM resonator.

To get around this limitation the solution is to fabricate adiabatic tapered optical fibers. Adiabatic fiber tapers are tapered fibers with a shallow transition angle. This shallow transition angle prevents coupling into higher order modes by insuring that the overlap between higher order modes is minimal and on the order of an optical cycle. In this sense, the tapered region is adiabatically converting the optical fiber mode to the tapered fiber mode without coupling light into the higher order modes[28]. When light is coupled into a higher order mode, it follows a different effective path through the tapered fiber. When the light returns to the standard dimension optical fiber the two modes interfere. This structure is similar to a Mach Zehnder interferometer, thereby making the detected signal dependent on stress and temperature[29,30]. While this is useful for sensor applications, it is not ideal for coupling light into to WGM resonators. Light coupled into higher order modes can prevent efficient coupling into the WGM resonator, increase the noise and difficulty of the measurement of resonator parameters, and may also excite unintended modes.

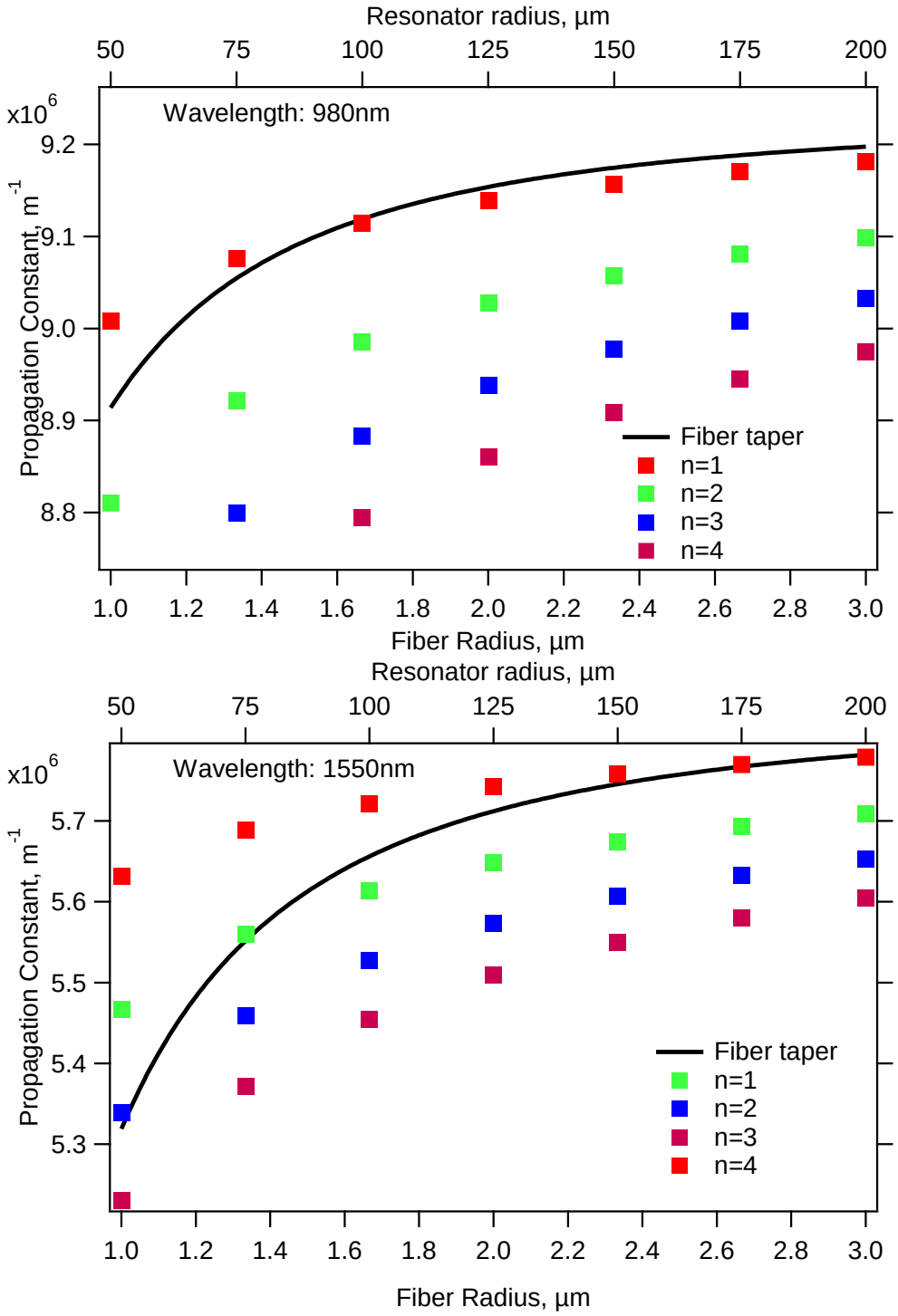

Figure 2.1: Propagation constants for microresonators and fiber tapers of a given radius at 980nm (top) and 1550nm (bottom). The fundamental mode of the fiber taper and the first four radial modes of the microresonator are plotted.

To match the propagation constants of the whispering gallery mode and the tapered optical fiber mode it is important to take into consideration the

parameters of the materials used, the dimensions of the two waveguide structures, and the wavelength of light used to excite the microresonator. This is detailed by Knight et. al. in Reference [19].

The taper diameter is chosen based on the results of this analysis. In Figure 2.1 we can see the propagation constant of taper radii and resonator radii for the two main wavelengths used for experiments: 1550nm and 980nm. This plot can be read by identifying the radius of the microresonator diameter and mode under test and matching the propagation constant to the corresponding taper diameter. For example, at 980 nm the ideal fiber diameter for coupling to the n=1 mode of a 125 μm radius microresonator is about 1.8 μm. At a longer operating wavelength, the radius of the tapered fiber can be substantially larger; at 1550 nm the fiber taper should have a radius of 2.4 μm.

2.2 Fabrication of tapered optical fiber

The fabrication of tapered optical fiber is a simple procedure, but requires fine process control to produce high quality tapered fibers suitable for coupling light into microresonators. Tapered fibers are fabricated by stretching optical fiber while heating it with a butane or hydrogen torch. The flame is moved across the fiber in a brushing motion to create an extended waist. This technique is known as flame brushing[28,31–34].

The shape of tapered optical fibers depends on the extent of the flame brushing region during the fiber tapering process. In general, the flame brushing region can stay constant or change. If the flame brushing region, L, is constant the taper transition profile will be exponential decreasing from the initial fiber radius, r_0, and follow the equation[31]:

$$r(z) = r_0 e^{-\frac{z}{L}} \qquad (2.3)$$

With a non-stationary hot zone customized profiles can be fabricated. By decreasing the size of the hot zone as the taper is elongated a linear taper transition can be generated. This is ideal for adiabatic tapers as the angle of the transition region can be controlled to be less than that required by the adiabatic criteria[28]. It is a complex process that requires very high precision stages and motion algorithms to work properly. Tapers fabricated in this fashion can be on the nanometer scale; the technique is outlined in detail by Lutzler[32]. Note that this type of control is not necessary for tapers used for microresonator coupling. Tapers fabricated in this fashion have been used for quantum optics experiments[35–37].

There are two configurations suitable for fabrication with each configuration composed of primary and secondary stages[32,38]. Primary stages are responsible for the tapering process itself, and the secondary stage is responsible for presenting the flame to the optical fiber and removing it when tapering is complete. The first configuration requires three primary stages and one secondary stage. Two of the primary stages slowly elongate the fiber while the third stage brushes the flame across the length of the fiber. The second configuration requires only two primary stages and one secondary stage. In this configuration, the flame is stationary and the brushing and elongation both happen due to the motion of the two primary stages. The stages are synchronized to move back and forth, which takes care of the flame brushing. The two stages are also set in motion away from each other, which takes care of the elongation. The equations of motion for this configuration are:

$$x_1(t) = \frac{\mathrm{L}}{2}\sin\left(\frac{2\pi v_{flame}}{L}t\right) + v_{pull}t \qquad (2.4)$$

$$x_2(t) = \frac{\mathrm{L}}{2}\sin\left(\frac{2\pi v_{flame}}{L}t\right) - v_{pull}t \qquad (2.5)$$

Parameters for describing exponential tapers are: waist length (mm), overall length (mm), waist diameter (μm), and fiber diameter (μm). For fabrication these are distilled to the hot zone length and pull length. Flame and pulling velocity are independent of the shape, but choosing appropriate values is important for maintaining a high quality taper. The pulling velocity should be very slow and is typically chosen to be between 100 to 250 μm/s, while the flame velocity should typically chosen to be around 2 mm/s.

Tapers with exponential profiles are fabricated by pulling with a constant hot zone. The equation which describes the taper profile parameters is nominally described by:

$$L_{pull} = 2L_0 \ln\left(\frac{125}{d_w}\right) \qquad (2.6)$$

In this equation L_0 is the hot zone length, d_w, is the waist diameter, and L_{pull} is the total fiber pull length. To make a fiber taper with a waist diameter of 2μm with a 5mm hot zone, the fiber must be stretched 41.35 mm. This takes 207 seconds when pulling at a rate of 200 μm/s.

The slow pulling rate is to insure that the fiber is not elongated too much during a roundtrip of the flame so that the brushed flame looks like a continuous hot zone. This is limited by the speed of the flame brushing, which as before, is typically chosen to be around 2 mm/s. The absolute value is not important, but it is limited on the upper end by the ability for heat to be transferred to the optical fiber. If the pulling rate is too fast the taper will have unwanted steps in the profile and deviate from the expected exponential curve.

2.3 Temperature considerations

There are a few considerations for temperature of the fused silica during tapering. Fused silica is the amorphous state of quartz. At room temperature there are crystalline states that may be favored after heating and cooling the fused silica to a certain temperature. This can occur when heating above 1550°C in which case crystalline β-quartz is formed which causes a loss in transmission. In order for tapering to occur the fiber must be deformable but not sag under its own weight. This discussion calls for the introduction of two concepts: the annealing and softening point. The softening point is the temperature at which the viscosity of the fiber is lowered to the point where it can deform under its own weight and the annealing point is the temperature at which the internal stresses of the glass are relieved. For fused silica the annealing point is 1140°C and the softening point is 1665°C. So fabrication at temperatures above the annealing point, but below the temperature at which the fused silica may crystallize into quartz are important for fabricating robust tapers with accurate shape profiles and low loss. This is not necessarily a straight forward metric to achieve.

A butane flame burns in air at 1970°C which is far above the softening point of fused silica. To control the temperature at the fiber the distance from the flame to the fiber must be controlled. This can either be done with a thermocouple to measure the absolute temperature, or simply through trial and error as the window for tapering is rather generous.

Another consideration when using a butane flame is the type of flame that is produced. Typically when using a standard butane torch the torch will produce a jetting flame. This type of flame is not ideal for fabricating tapered fibers. Not only is this much hotter than required, but it also causes significant turbulent

airflow around the taper. When the taper is brought down to dimensions below 20 μm these currents will cause the taper to deform ruining the profile and transmission of the fiber. It is ideal to use a flame which is air starved, generating a small candle like flame which does not cause any turbulence. A suitable flame is shown in Figure 2.2.

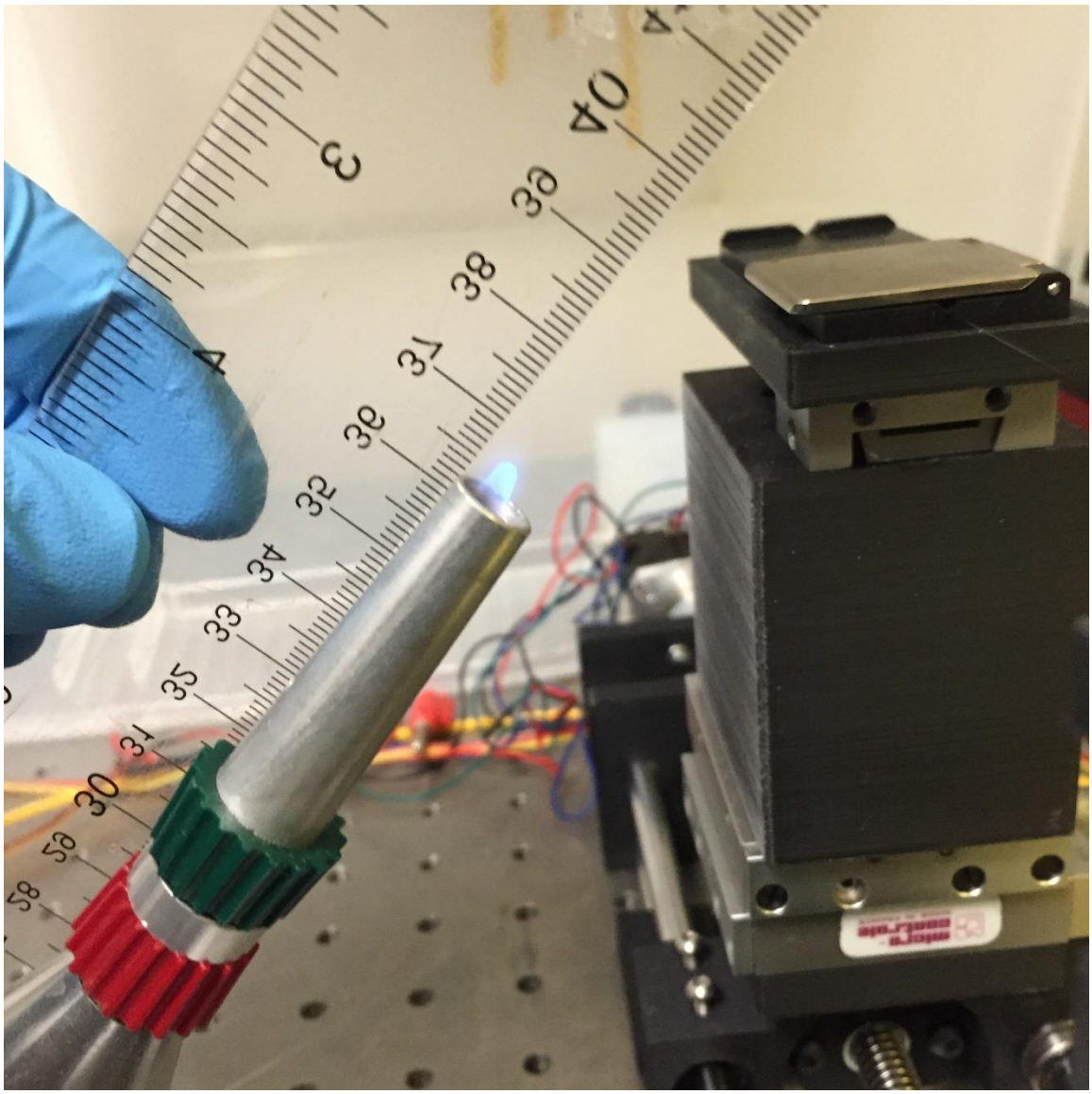

Figure 2.2: Oxygen limited butane flame suitable for tapering optical fiber. The flame is generated with a Microflam brand torch which has adjustable air and gas levels. The flame is approximately 4mm tall.

When working with a flame this low it is important to also control the air currents in the room. Any minor air current in the room can alter or extinguish the flame so protecting it is important. Air currents in the room can also move the tapered fiber during the tapering process causing a poor taper profile. The tapering system should be enclosed in a box to reduce air turbulence and also protect the system from dust.

2.4 Fiber preparation

Preparing the optical fiber is an important step in tapering optical fiber. In order to fabricate a good taper the fiber surface must be free of debris and damage. If there is debris on the fiber while it is being stretched the debris will disjoint the taper profile and ruin the transmission of the tapered fiber. The fiber is prepared by mechanically stripping 35mm from some portion of the fiber. Using a high quality fiber stripper is important. Mechanical fiber stripping can cause microfractures in the fiber which can lead to a poor final taper result. The stripped region is wiped clean with ethanol to remove most of the debris, then it is carefully wiped with acetone such that the polymer coating is not in contact with the solvent. Finally the region is gently wiped again with ethanol and loaded into the fiber chucks of the tapering apparatus. This three step cleaning process ensures that the fiber is free of debris. The initial ethanol wipe removes most bulk debris. The acetone wipe further removes polymer from the surface by slightly dissolving the polymer and lifting it from the fiber surface. Avoiding touching the bulk polymer coating prevents transferring some of that polymer onto the surface of the fiber. The final ethanol wipe removes any final debris and polymer.

2.5 3D Printed linear stages

Commercial motorized stages and motion controllers can cost multiple thousands of dollars. In order to make this apparatus affordable, the motorized stages were designed and fabricated using 3D printed parts. The motion control electronics were built using an Arduino microcontroller. The principle of operation of linear motion is relatively simple. A lead screw is rotated by a motor. The lead nut is constrained from rotation by a bearing rail. This defines the direction of motion. As the lead screw is rotated the lead nut travels across the screw. The lead screw is rotated by use of a stepper motor. Using a stepper motor is ideal in this type of system as each step rotates the motor a certain amount. In the case of the stepper motors used this was 1.8^{o} per step. This can further be improved by using stepper motor driver electronics which allow for microstepping. These electronics can provide 32X microstepping which will brings this figure down to $.05625^{o}$ per step allowing for very accurate positioning. The benefit of stepper motors is that positioning can be determined by counting the number of steps given to the motor since each step moves a specified amount. This gives precise relative positioning without the need of expensive and complicated encoders used in servo or other DC motors. Furthermore, error in the stepping of a stepper motor does not accumulate allowing for high accuracy positioning.

The stages were designed using parametric open source CAD software called OpenSCAD[39] and printed on a Reprap style 3D printer[40]. Reprap is an open source lineage of 3D printer designs. The idea behind Reprap is to make self-replicating machines—a 3D printer that prints 3D printers. In reality this manifests itself as designs that rely heavily on 3D printed components as well as mass produced hardware and electronics to build the next design. As such, each Reprap

3D printer has been built using components from a previous generation or sister 3D printer.

The 3D printer design used is called the Mendel90 and was built by a kit including hardware and 3D printed parts. The stages were designed for printing on a 3D printer and take the limitations and capabilities of fused deposition modeling (FDM) into consideration. FDM is a 3D printing method in which a thermoplastic polymer filament is extruded layer by layer. The 3d printer extrudes layers .3mm thick at a time, which limits the resolution along the *z*-axis. The resolution in the *xy*-plane is much better and as such features that require higher resolution should be printed in this direction. A second consideration is to design in such a way that limits overhangs. Since the printer prints layer by layer in the *z*-axis it is important to make sure that there is some material supporting the next layer as the model is built. This can either be by design or by generating support material for overhangs which exceed a certain angle. The typical point to consider using support material is when overhangs deviate greater than 45^{o} from the *z*-axis.

The toolchain for the process has a few steps. First a 3D model must be generated using CAD software such as Solidworks or OpenSCAD. This model is then exported as an STL file. STL files break the model up into many triangles which describe the 3D structure of the model. The STL file is imported into software called a slicer. There are a handful of different slicer software options available with different feature set; the software we used is called Slic3r[41]. This software chops the STL file up into layers and generates a file which describes the movement of the 3D printer nozzle, extrusion, and temperatures using G code. G code is the standard code to describe motion for CNC manufacturing machines[42]. Once the G code is generated it can then be uploaded to the 3D

printer using some type of interface software. The firmware on the 3D printer interprets the G code and prints the object.

The material used for 3D printing the linear stages is polylactic acid or PLA. This is one of the two standard 3D printing materials, the other being acrylonitrile butadiene styrene or ABS. PLA was chosen over ABS since it is more rigid than ABS and is less prone to warping during the printing process. Both of these properties are crucial to producing a high quality linear stage. ABS however does have the advantage of having a higher glass transition temperature and is suitable for making components that may have to withstand heat such as parts which house the hot extruder in 3D printers[43].

PLA is extruded at a temperature of 180^{o}C and the glass build plate of the 3d printer is kept at 60^{o}C which is around the T_{glass} for PLA. This promotes adhesion of the first layer to the print surface to ensure a successful print. First layer adhesion is critical to successful 3D printing. If the part delaminates during the printing process the print will completely fail. In order to combat this not only is a heated build plate used, but also a thin layer of PVA is spread on the glass prior to printing. This solution is made by diluted standard PVA glue (Elmer's brand, etc) at a ratio of 1 part glue to 10 parts water and spreading it on the build plate with a wipe. The PVA greatly improves adhesion of PLA on glass allowing for a high yield.

The stages are designed using five 3D printed pieces. These pieces define the axis of linear motion and provide mounting of the motor, taper mounts, and the stage itself to the table. The stage consists of a: motor mount, front lead screw plate, end plate, carriage, and mounting plate. Each 3D printed component can be seen rendered in its approximate position in Figure 2.4. The different segments are connected by 8mm hardened steel rails which give the stage its structure and

provide constraints for the bearings and carriage to ride on. The plates are designed to work with the 3D printer by avoiding over hangs and having high precision features in the *xy* plane of the print bed. There were two major design iterations used and built for fabricated tapered optical fibers. The major features of the first design are a square and centered profile and side slit tightening friction supports to mount the steel rails. The carriage which holds the linear bearing, lead nut, and mounting holes for optics is a monolithic unit. This design was used for a majority of the tapering work, but after some time the design was upgraded to the current design. The side slit tightening causes some warping since a screw causes the tabs to bend in to increase the friction force on the rods. The bending is undesirable for squaring the stages with themselves.

The lead screw attaches to the motor by means of a spiral flex coupling. This type of coupling is desirable over a rigid coupling as it allows for small angular misalignments between the motor shaft and the lead screw. The lead screw is supported by a bearing which is embedded in the so-called lead screw mount. The lead screw has thread diameter of 3/16″ and 1/4″ input shaft; between these two diameters is a 5/16″ shoulder. This shoulder fits in the bearing and supports the lead screw. The lead screw is allowed be free on the opposite end. If the far end of the lead screw is supported it can lead to over constraint in the system since the linear motion is being defined by three points rather than two. Supporting the far end increases the rigidity of the system and allows for higher speeds of travel at the cost of higher precision in alignment of the linear rails and lead screw. For fiber tapering a slow steady speed is necessary. Since we are lower costs by not using high precision machining freeing the system is the easiest option. The stage design allows for support on the far ends of the lead screw if wanted. This simply requires a more tedious alignment of the linear shafts and lead screw, driving a lighter load,

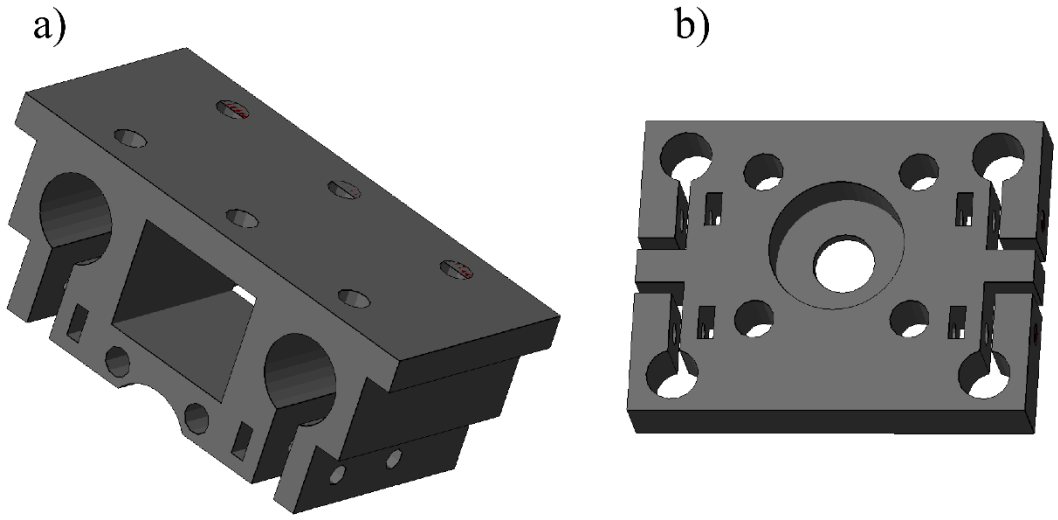

Figure 2.3: 3D renderings of components of the version 1 design showing off the square design and side fastening in the a) carriage and b) main lead screw and end plates.

and using motors with higher torque or a smaller microstepping amount to increase the torque provided to the lead screw to avoid binding due to over constraint. Examples of the tightening method, bearing plate, and the monolithic carriage can be seen in Figure 2.3. An image of the final fabricated stage design can be seen in Figure 2.5.

The second version was designed to have a lower rectangular profile and a carriage which had attachable mounting plates. The carriage has a set of four holes arranged in an 11mm square pattern for use of these different platforms. This was done to be compatible with Thorlabs' line of flexure stage accessories as well as easily attaching unique optics hardware to the stages such as manual micrometers with non-standard mounting holes. The low profile was used to keep the taper fabrication lower to the optical table and keep the final system design more compact. The side slit friction tightening method for clamping the rods to the 3D printed parts was replaced with set screws. This provides an easier adjustment and does not warp the plastic pieces. It also provides a cleaner overall look as the

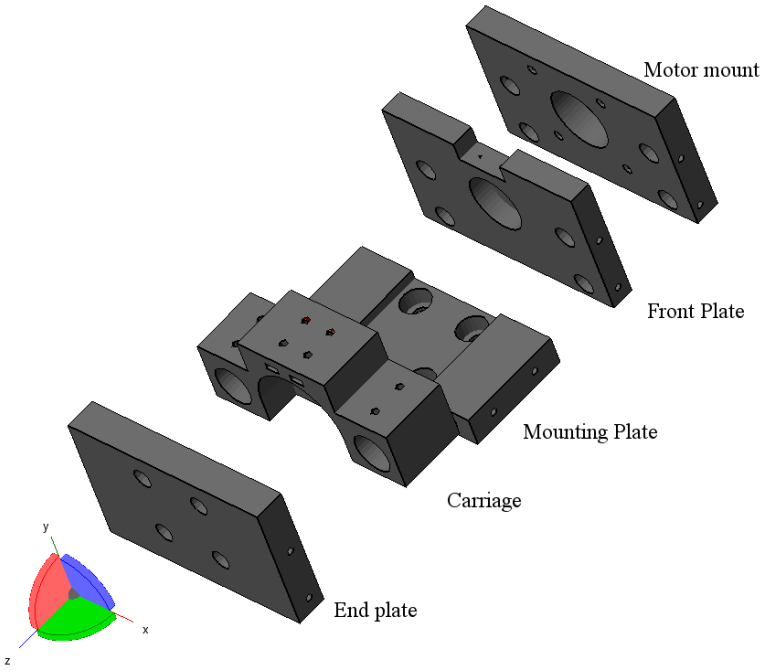

Figure 2.4: OpenSCAD rendering of 3d printed pieces of linear stage. Hardware such as motors, screws, rails, and bearings are not included.

mounting hardware is slightly recessed into the 3D printed pieces. This not only makes the stages more aesthetically pleasing, but also allows for flat surfaces for alignment and squaring of the stages during mounting. The CAD design of the 3D printed parts can be seen in Figure 2.4 and an image of the fabricated stage is in Figure 2.6. A bill of materials for the hardware components used in making the version 2 design is listed in Table 2.1.

Table 2.1: Bill of Materials for Linear Stage Design v2

Part	Quantity
Nema 17 motor	1
Endstop microswitch	1
5mm to 6.35mm flexible coupling	1
608 bearing 8x22x7mm	1
Lead screw 3/8”x12	1
Lead nut 3/8”x12	1
8mm x 200mm hardened steel rail	4
LM8UU style linear bearing	2
M3x6mm set screw	20
M4x25x screw	2
M4 Nylon locking nut	2
3d printed parts and plates	5

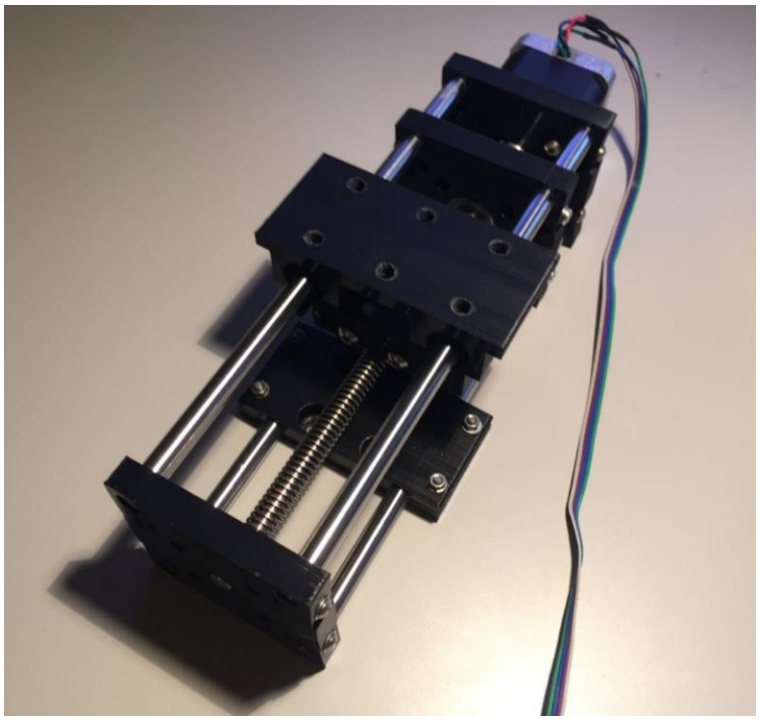

Figure 2.5: First design of stages used for tapering optical fiber

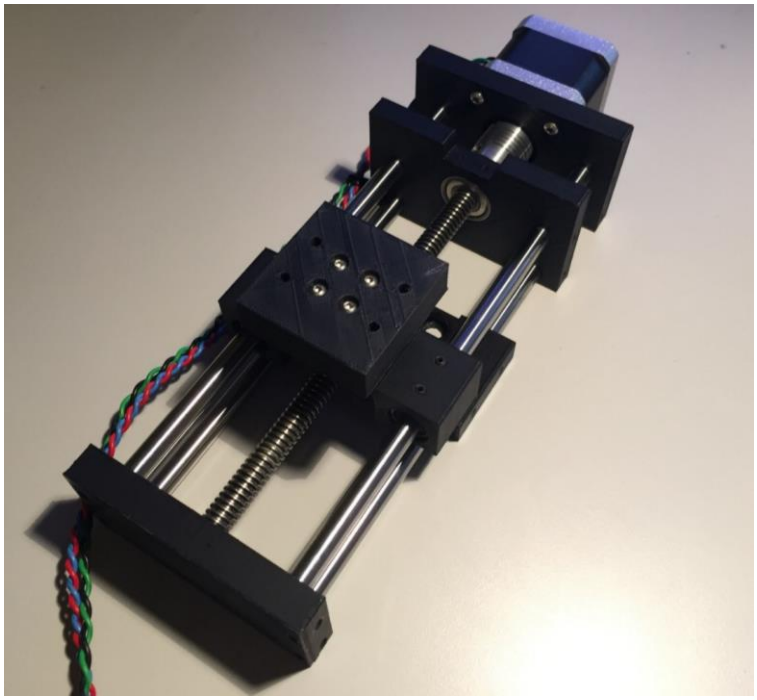

Figure 2.6: Second design of stages for tapering optical fiber. This stage features mounting holes for a custom stage plate for mounting various optics and fiber mounts. It also has an inset for endstops for precise positioning.

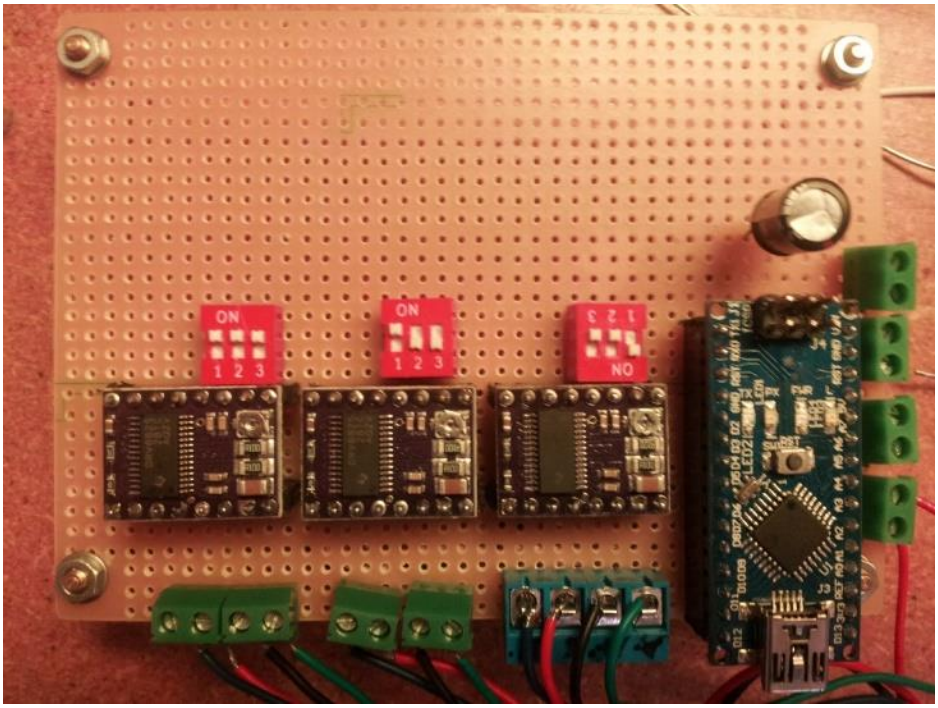

Figure 2.7: Prototype electronics board for motion control.

The motion control electronics are based around an Arduino microcontroller development board. There have been multiple iterations of the firmware used to drive the linear stages with various levels of complexity in timing and functionality for generating the motion needed to adequately taper optical fibers. The stepper motor drivers used are based on the DRV8825 chip by Texas Instruments. A breakout board which includes current setting controls was used for interfacing with the motors. This breakout board is available from Pololu Robotics & Electronics. The stepper motor driver module can provide 1.5 A of current per motor coil and drive motors up to 45 V. It can also provide microstepping resolution down to 1/32-step. Using the 12 thread per inch lead screw this can provide a theoretical step resolution of 330.7 nm/step. However this is completely overshadowed by backlash in the lead screw and nut, but still provides a good metric for having good stepping accuracy over 10 to 20μm of linear movement. The Arduino is programmed to control 3 stepper motors drivers simultaneously driving four stages. Two stages stretch the optical fiber, one stage

performs the flame brushing, and a final stage is used to present and remove the flame to the optical fiber at the beginning and end of the tapering process as described above. The stages used for pulling the optical fiber are wired to the same stepper motor driver to insure that they move together at the same rate. The stepper motors phases are wired in series to insure the same current through each motor. A simple serial protocol was developed to communicate commands between the Arduino and a PC computer running a specialized LabVIEW program. The prototype electronics board layout is seen in Figure 2.7.

2.6 Experimental tapering results and discussion

Testing the tapering system is a time consuming process that requires a good deal of trial and error to optimize the parameters discussed earlier in this chapter. In this section, different taper profiles are shown that have been fabricated with the 3D printed tapering system.

The taper profiles shown below are measured with a digital video measurement microscope which can provide accurate and semi-automated measurements of edge profiles of objects. The primary goal in this exercise is to find tapers with a good exponential profile without any bumps or discontinuities that might affect the optical transmission and mode distribution of the tapered fiber.

A few taper profiles are shown in Figure 2.8. These tapers are designed to be 5μm at the waist region. The profiles are shown alongside a corresponding logarithmic scale to show the exponential profile of the tapered fiber's transition region. In a logarithmic scale the transmission region should be a straight line. By viewing this region in this fashion non-exponential profiles can be identified and

errors in the fabrication process can be identified. In Figure 2.8.c there are major discontinuities between the two halves as well as a non-linear profile in the second half of the taper. This is due to the hot zone being too large and the flame speed and pull rate product too high causing regions to be pulled asymmetrically as described in Section 2.2

These methods have been used to fabricate tapered optical fibers for coupling light into microresonators discuss throughout this thesis. The standard parameters used for tapering are outlined in Section 2.2 To fabricate a 2 μm taper with a 5mm hot zone the fiber is stretched 41.35mm. These typically produce fibers suitable for use at 980nm. A smaller hot zone may be used and the fiber stretch time will be accordingly reduced.

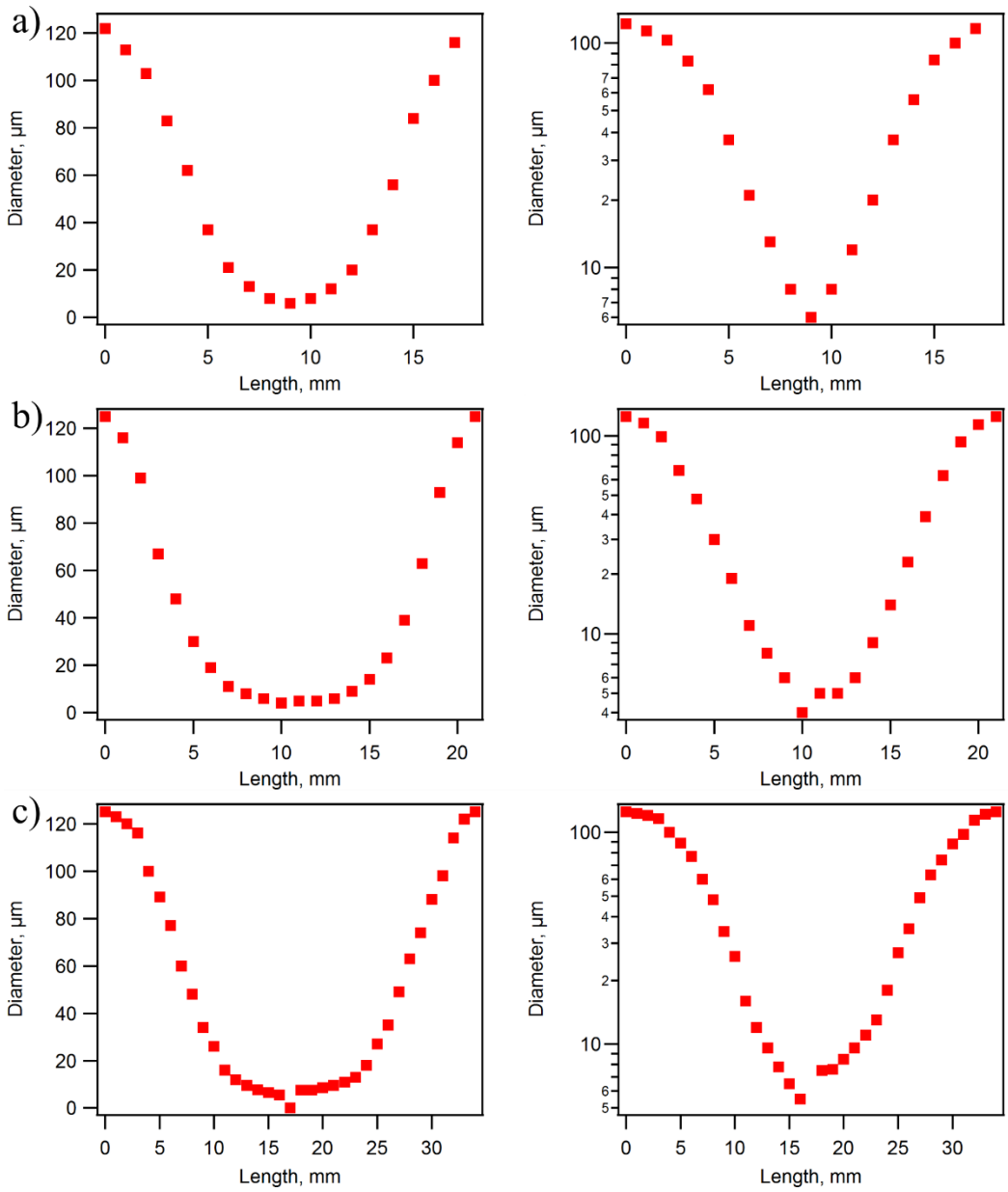

Figure 2.8: Measured profiles of tapered optical fibers fabricated with different parameters with both linear and log scaling. The goal taper waist width for each taper is 5µm with a varying hot zone size. The hot zone size is 3mm, 4mm, and 5mm for a to c respectively.

Chapter 3: Characterizing whispering gallery mode resonators

3.1 Optical whispering gallery mode resonators and microspheres

WGM resonators share many qualities with conventional standing wave optical resonators. The most well-known resonator of this class is the Fabry-Perot cavity. A Fabry-Perot cavity(FP) is composed of two highly reflective mirrors separated by a distance, L. Light launched into a FP cavity is said to be resonating when an integer number of half-wavelengths fit in the cavity. Satisfying this resonance condition allows the electromagnetic field to constructively interfere leading to field enhancement within the cavity. The analogous condition for resonance in a WGM resonator is fitting an integer number of half-wavelengths inside the circumference of the sphere or ring.

Resonators are often characterized by two characteristics: free spectral range(FSR) and quality factor(Q-factor). The Q-factor quantifies how well the cavity stores energy; the higher the Q-factor the more energy is stored in the cavity and therefore the field enhancement is greater. In the case of optical resonators Q-factor can be calculated by: $Q = f/\Delta f$ where f is the resonant frequency and Δf is the full-width at half maximum of the resonance. Q-factor is determined by the material and fabrication of the resonator. In a FP cavity made out of two high-reflecting mirrors, the Q-factor is often not much above 10^3[6]. On the other hand, silica microspheres have extremely high-Q due to the fabrication process creating

such a perfectly spherical surface and silica having very low loss. Experimentally, Q-factors of 10^7-10^8 are easily obtainable[17]; the theoretical limit for silica microspheres is greater than 10^{11}[20]. In a high-Q WGM resonator it is quite possible to have a resonant field enhancement of many watts from an input field of one hundred microwatts.

Free spectral range is the spectral spacing between resonant modes; this is determined by the length of the cavity and is given by: $f_{FSR} = \frac{C}{2L}$ or $\lambda_{FSR} \approx \frac{\lambda^2}{2L}$. These parameters are also used in WGM resonators. The FSR can be estimated coarsely by assuming the effective cavity length is approximately equal to the optical path length around the circumference of the resonator: $f_{FSR} = \frac{c}{n\pi D}$. This deviates slightly from the exact value due to mode propagation occurring inside the circumference of the resonator[1,6,15].

In a perfect FP cavity the only modes that exist are due to the single dimension of freedom. Microspheres are three dimensional and thus have at the very least three variables that define the actual mode structure. The modes that exist are from the length of the resonator (dependence on polar angle) and the spatial profile of the mode (dependence on radial position and azimuthal angle). These mode combinations exist for both TE and TM light propagating in the microresonator[6,15,44].

The basic FSR described above in this case is determined by the fundamental mode spacing (wavelengths around the equator) and seen by the repetition of the spectral pattern of the modes. For small diameter and highly spherical microspheres the FSR is very large, and with careful control of polarization and coupling the spectral density of modes is very sparse due to a large amount of degeneracy in higher order modes. The higher order modes

become non-degenerate due to eccentricity in the microsphere and surface defects. Microrings, disks, and toroids are beneficial due to the reduced dimensionality of the resonator supporting very few modes when compared to a microsphere. This is especially useful when looking at wavelength tracking and Q-factor measurements for sensing experiments.

WGM resonators are also praised for their very low mode volume. Mode volume is a measure of how much physical space a mode occupies by looking at how much of the mode's intensity is concentrated around the intensity maxima. A low mode volume corresponds to a very tightly confined mode; in microspheres the modes are confined around the equator of the sphere. The mode volume of a microsphere is approximated as [17]:

$$V_{eff} \approx 3.4\pi^{\frac{3}{2}}\left(\frac{\lambda}{2\pi n}\right)^{3}\left(\frac{\pi n D}{\lambda}\right)^{\frac{11}{6}} \qquad (3.1)$$

3.2 Fabrication of microsphere resonators

Microsphere resonators are ideal for test experiments due to their ease of fabrication, ease of use and handling, and superb quality as optical resonators. This makes silica microspheres a perfect platform for testing different techniques for coating, depositing materials, and interrogating nonlinear properties of other materials. The high Q-factor lets us access phenomena usually limited to high powers such as multi-photon absorption, Raman scattering[3], and other nonlinear effects[17]. The low spectral density of modes allows us to interrogate single modes of a microsphere and determine how coating and deposition alter the Q-factor of the microsphere.

Microspheres are fabricated using fused silica optical fiber (Corning SMF-28). The fiber is pulled to a thin taper by heating with a butane torch. The taper

is cleaved in half and then heated with the electric arc from a fusion splicer (Ericsson FSU995) to form the sphere. Microsphere diameter ranges from 30μm to 150μm and is controlled by taper width, arc position on the fiber, and arc intensity and duration. Microspheres formed on the end of an optical fiber are much easier to handle; the stem adds a very small perturbation to the mode structure of the sphere. Since the mode volume of whispering gallery modes is very low the response of the microsphere is almost unaltered from a perfect sphere.

3.3 Experimental characterization of WGM resonators

The simplest method for coupling light into a microsphere, or any silica whispering gallery mode resonator, is by use of tapered optical fiber. An optical fiber taper is a thin segment of optical fiber on the order of one to ten microns. Light in a tapered region of fiber is guided by a fiber-air interface. This large difference in index allows for an evanescent wave to exist multiple microns from the surface of the taper. This evanescent wave can be coupled into the microsphere by bringing the sphere close to the taper by use of a piezo-actuated stage. The

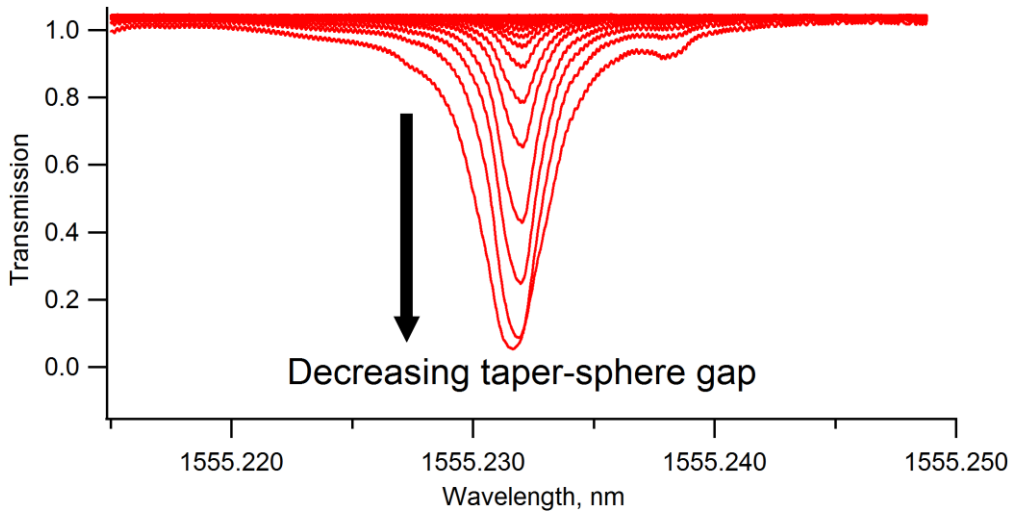

Figure 3.1: Zoom in on single resonance transmission showing increased light coupling into the sphere as a result of decreasing the taper-sphere gap.

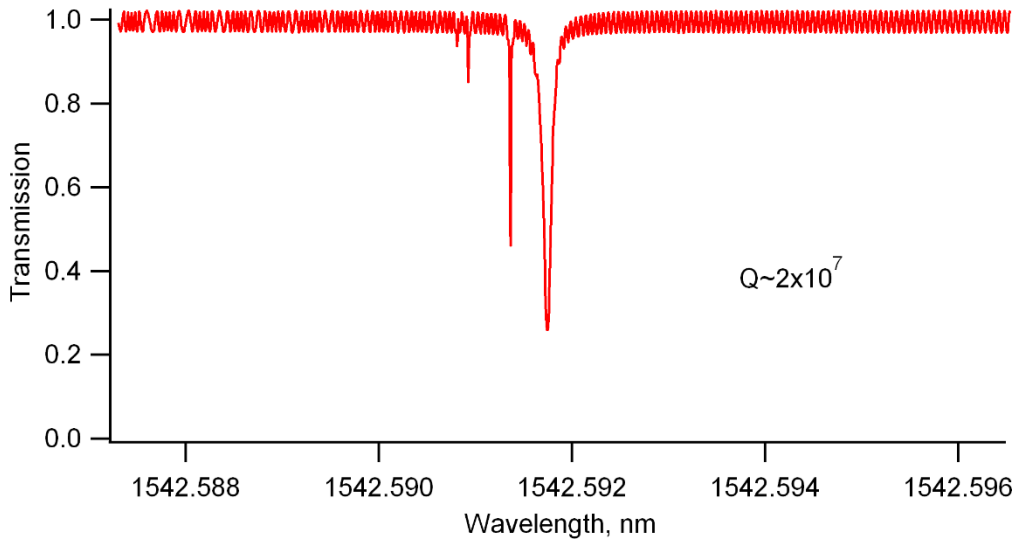

Figure 3.2: Fundamental resonance with higher order resonances. Q-factor of fundamental $2x10^7$.

taper-microsphere gap determines the coupling efficiency of light into the microsphere.

Coupling can be optimized by positioning the microsphere so that transmission through the taper-microsphere system on resonance is minimized—most of the light is coupled into the mode on resonance. The test bed consists of a microsphere on a piezo positioning stage with 20nm resolution and a section of tapered optical fiber. We couple the light from a tunable laser at 1550nm (Agilent 8164b/81600b) or 980nm (New Focus 6328) and optimize the light coupling into the microsphere by moving it with the piezo stage. Polarization can also be controlled to increase coupling efficiency.

The transmission is recorded; resonant frequencies can be found and Q-factors measured by looking at dips in the transmission and calculating the FWHM of the dip. The system also has two microscopes which provide a top and side view to aid in alignment of the fiber taper to the equator of the microsphere or other whispering gallery mode resonator such as microbubbles or microdisk resonators.

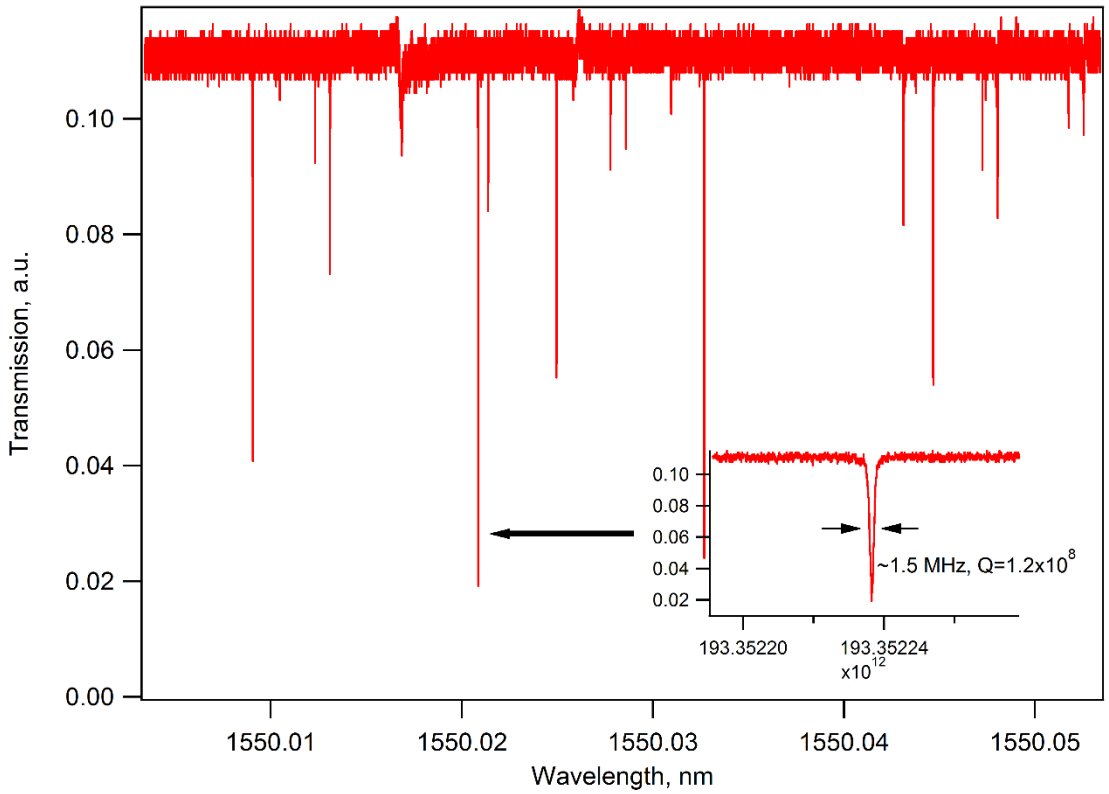

Figure 3.3: Microsphere modes and inset linewidth measurement shows Q-factor of 1.2x10^8

All of the components are mounted on rails and can easily be switched out to accommodate necessary functionality to include other measurement devices, such as photodetectors, or spectrometers.

The fundamental attribute to measure when working with WGM resonators, as heavily stressed throughout this text, is the Q-factor. This measurement is done as calculated and described in Section 3.1 Light is coupled into the microresonator by means of tapered optical fiber and the frequency is tuned to view the resonance. The linewidth of the mode under question is measured and the Q-factor is calculated by $Q = \frac{f}{\delta f}$. When interrogating microresonators for Q-factor it is important to use very low input power; power less than 100 μW is ideal to prevent loading of the cavity which will cause

linewidth broadening from thermal heating of the cavity due to the high Q-factor causing a high circulating power[17,45,46].

The Q-factor can also be used to calculate the photon lifetime as: $Q = \omega\tau/2$. This can be broken up into two decay rates that describe loss mechanisms of the resonant mode: intrinsic and extrinsic. Intrinsic lifetime, τ_0, refers to the rate of absorption and radiation processes in the microresonator which cause loss. The extrinsic lifetime, τ_e, refers to the coupling rate between the resonator-taper and the taper pathway. This rate is primarily defined by the tapered fiber parameters and more directly by the separation of the tapered optical fiber from the microresonator[27]. The overall Q-factor can be written as

$$\frac{1}{Q} = \frac{1}{Q_0} + \frac{1}{Q_e} \qquad (3.2)$$

when taking both lifetimes into account[14].

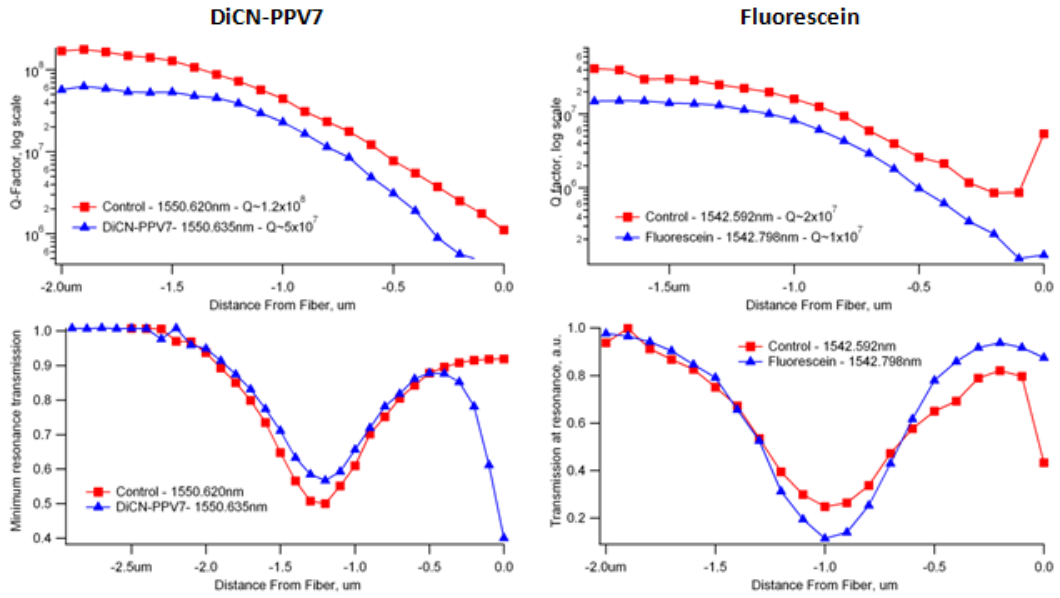

Figure 3.4: Coupling at Q-factor of microresonators as a function of taper distance. Each graphs shows the same microresonator clean and subsequently dip coated in a dye. Critical coupling can be observed at 1.2μm and 1.2μm from the surface of the resoantor.

There are three regimes of coupling: under coupled, critically coupled, and over coupled. They are defined by the relationship of the intrinsic photon lifetime to the extrinsic photon lifetime. The under coupled regime is when the intrinsic lifetime is less than the extrinsic lifetime; light leaves the resonator faster than it can be coupled into the resonator. This occurs when the tapered fiber is significantly far away from the microresonator. Critical coupling occurs when the extrinsic lifetime and the intrinsic lifetime are equal. Power transferred from the taper is maximal at this point. Over coupling occurs when the intrinsic lifetime is greater than the extrinsic lifetime. In this regime light is coupled out into the tapered fiber at a faster rate than it is lost via radiation or absorption. Critical coupling locations can be seen in Figure 3.4. This is measured by identifying a mode and moving the microresonator closer to the taper with a piezo translation stage. The measured Q-factor is slightly higher in the under-coupled regime, but in this regime very little light is actually coupled into the microresonator. At critical coupling the microresonators have the maximal amount of light circulating due to the balance of coupling losses.

3.4 Using microresonators to calibrate laser dithering

Calibration of the dithering range of the laser is important to accurately measure Q-factor of WGM microresonators. When using a low input optical power the absolute frequency of the resonances will be stable. To calibrate the system the laser is dithered by a function generator and a single resonance is observed. The voltage corresponding to the resonance center is measured. The laser center frequency is slightly changed and another data point is observed. This results in a calibration curve relating the frequency of detuning to the voltage applied to the input of the tunable laser. This calibration is shown in Figure 3.5.

3.5 Conclusion

Measuring Q-factor and coupling light into WGM mciroresonators is critical for studying these optical devices. These basic measurements and techniques have been outlined and are important for future work which includes analyzing novel geometries of microresonators and looking at the nonlinear properties of some resonators and materials.

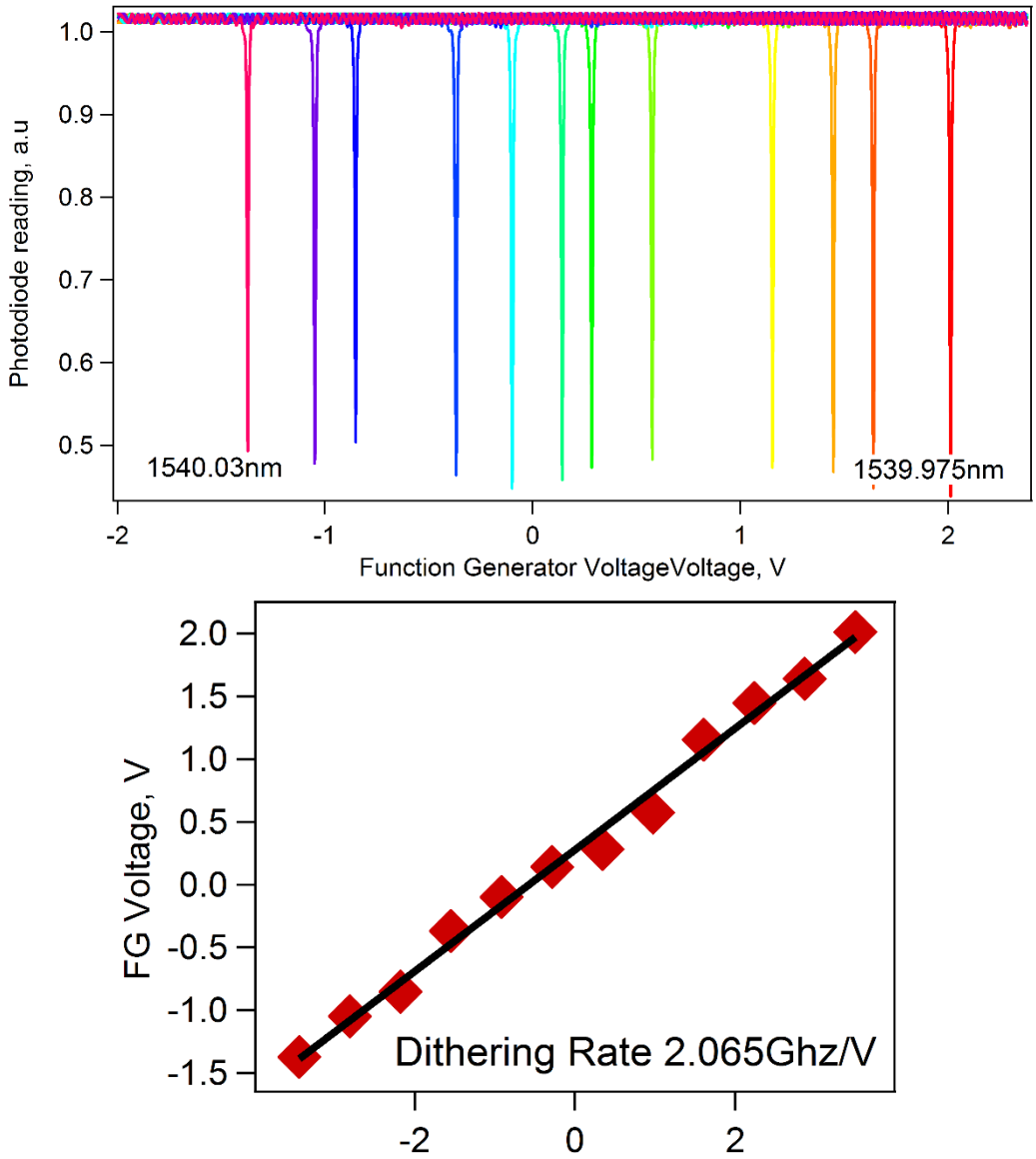

Figure 3.5: Resonator mode identification and calibration curve of Agilent 1550nm tunable laser.

Whispering gallery mode microresonators are an attractive platform for exploring nonlinear optics due to their intrinsic high-Q factor and low mode volume. A low mode volume brings a higher localized field intensity (W/m^2) per Q-factor since the same amount of circulating power exists in a smaller spatial region. This is especially important for nonlinear optics as many of the phenomena rely on the localized field intensity. This is explored further when looking at multiphoton fluorescence in microbubble resonators.

Chapter 4: Fabrication and application of microbubble resonators

4.1 Fabrication methods of microbubble resonators

Microresonator fabrication has been demonstrated using many different methods including lithography [21], micromachining [54], diamond turning [4], and thermo-mechanical [17,55,56] processes allowing for a wide range of microresonator geometries which make them suitable for various applications.

The microsphere and microtoroid have been standards in the community for some time, but recently novel geometries like the microbottle [57], liquid core optical ring resonator [58], and microbubble resonator [34,56,59,60] have shown interesting and novel properties. Liquid core optical ring resonators (LCORR) and microbubble resonators have immediate applications to optofluidics due to being formed with a hollow cavity suitable for the introduction of fluids. Microbubble resonators are fabricated by pressurizing a thin walled capillary and exposing it to heat by CO_2 laser illumination [13] or arc discharge [60]. Most demonstrations of the microbubble resonator have focused on tuning resonant wavelengths by pressure [34], stress [56,61], and refractive index [60,62]. Recently dye lasers [59,63], optomechanical oscillation [12] and various biosensing schemes [58] have been demonstrated in these microfluidic resonators.

Microbubble resonators are a relatively new type of resonator. This geometry is particularly interesting because it is fabricated in a capillary tube and allows liquids and gasses to be filled into the core region of the resonator.

Microbubble resonators are formed by heating a small section of capillary tubing under pressure. As the capillary tube becomes molten it expands as it tries to reach an equilibrium pressure. The microbubble resonator was originally demonstrated by Sumetsky et. al. in [56]. Sumetsky et. al. fabricated their microbubble resonators with absorptive heating via a CO_2 laser; this is an ideal method for fabricating microbubble resonators. As the resonator expands the wall thickness in the bubble region drops due to conservation of mass. As the wall thickness drops the light from the CO_2 laser is not absorbed as much and does not create as much heat due to Beer's law[6]:

$$I = I_o e^{-\alpha d} \qquad (4.1)$$

This makes the fabrication process highly reproducible and self-limiting. Fabrication using a CO_2 laser is not the only option for fabrication. Microbubble resonators can also be fabricated using an electric arc. This has been demonstrated [60] and is similar to the method used and outlined in this thesis.

4.2 Electric arc fabrication of microbubble resonators

Microbubble resonators fabricated for this dissertation work are fabricated with the electric arc from a fusion splicer[60]. In order to reliably fabricate microbubbles of adequate quality and size multiple parameters must be optimized: arc power, arc duration, and pressure.

In our initial efforts, we attempted to fabricate microbubbles from borosilicate glass capillary tubes. This material proved to be unsuitable for microbubble resonators due to a low softening point (821°C) making it difficult to shape the microbubble. The softening point of borosilicate is 821°C. The electric arc generated by a standard optical fiber fusion splicer is typically used for fused

silica fibers making it difficult to find parameters that are suitable for a material with such a low softening point. This led us to use fused silica capillaries which have a softening point of 1660°C[64]. The capillary tubes used were procured from Produstrial, have a wall thickness of 15μm and an outer diameter of 80 μm. This was the highest ratio of wall thickness to diameter that could be found on the micrometer scale. This geometry allows for expansion which results in a small bubble wall thickness. The goal wall thickness is between 1μm and 5μm and the diameter should be around 200μm to 300μm. The system for fabricating microbubble resonators consists of a fusion splicer (Fitel S147), a connection from a compressed air supply, a low pressure regulator, pressure gauge, and valves. Fabricating microbubble resonators can be thought of as microscale glass blowing. The thin capillary is connected to the regulated compressed air supply that provides pressures in the neighborhood of 40kPa, approximately 5.8 psi. The pressure can be controlled down to 1kPa with a regulator. The supply outputs to a ¼ inch air tube. To interface with the small diameter microbubble resonator a Luer lock adapter is used. This allows for a Luer lock style syringe fitting to be used with rest of the system. This is ideal as it inherently provides an interface with both pressure lines as well as liquid syringes for later experiments. A 30 gauge blunt Luer lock syringe liquid tip is used with Tygon PVC microbore medical tubing.

This tubing has an inner diameter of 0.010″ or 254μm, which brings the whole system down to the scale of the capillary tubing. The 80μm capillary is inserted into the opening of the microbore tubing and an air tight seal is created with UV curing epoxy. The opposing end of the capillary tube is sealed by melting the end

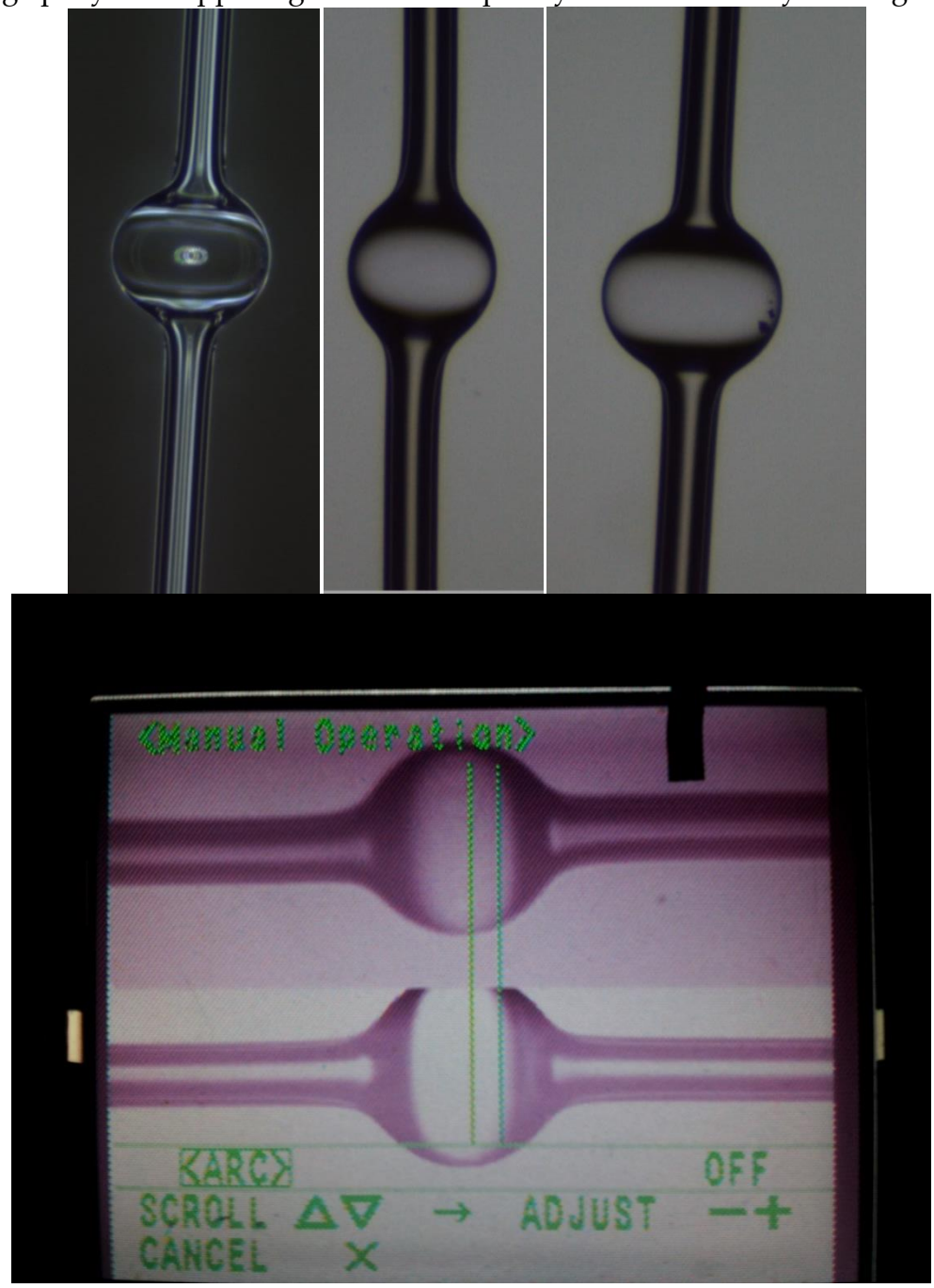

Figure 4.1: Formed microbubble resonators. Top row diameters are 280μm,250μm, and 210μm respectively. The bottom resonator shows the resonator from both top and side view as seen in by the microscope in the fusion splicer.

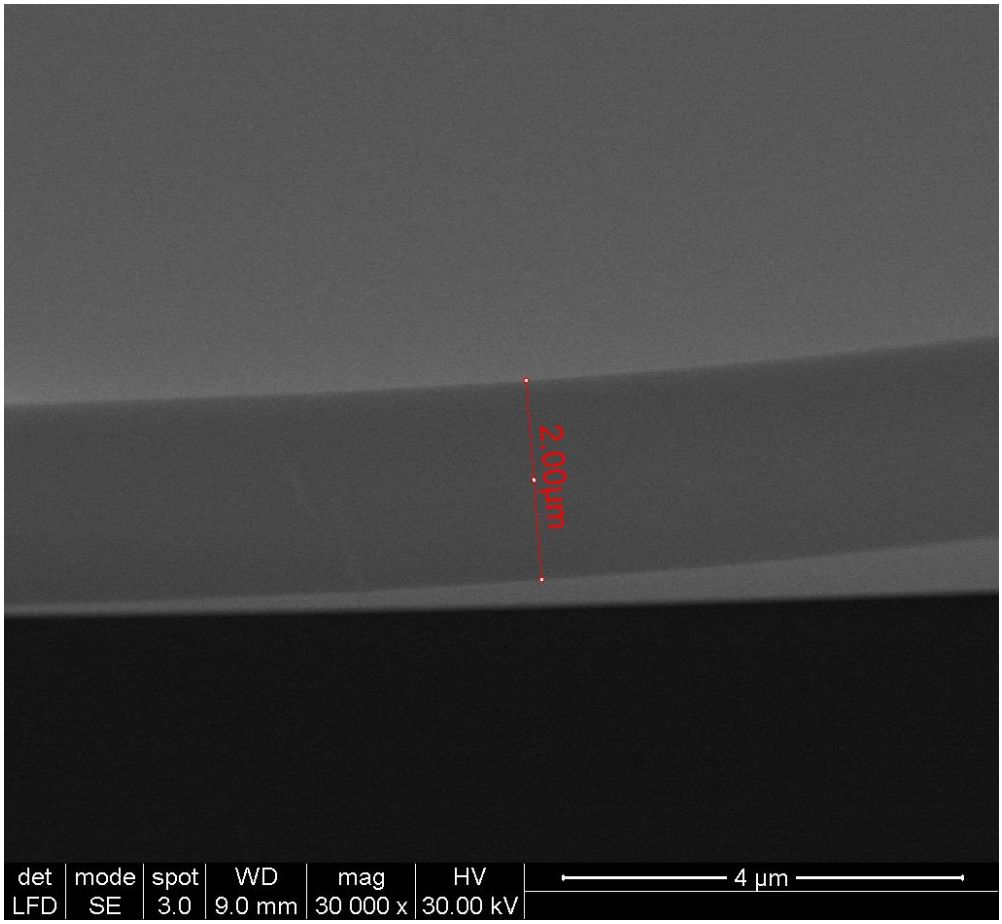

Figure 4.2: SEM image of broken microbubble resonator for measuring wall thickness. SEM image of broken microbubble resonator for measuring wall thickness.

with the fusion splicer. With both ends sealed, the outside of the capillary tube is cleaned with ethanol and a lint free wipe.

The capillary tube is placed in the fusion splicer and supported on both sides from the fiber chucks of the fusion splicer. The input pressure is increased to 40kPa and then the electric arc is applied. When the arc is applied the capillary softens and the pressure differential between the capillary and the atmosphere causes a bubble to form as it attempts to reach an equilibrium pressure. There are three parameters to be adjusted: arc duration, arc power, and pressure. The fusion splicer used references power as a number representing a portion of the maximum

possible arc power. This makes it difficult to relate this value to an actual power applied.

After the bubble if fabricated it is mounted in a 3D printed holder with epoxy. If the intended application involves passing liquid through the resonator the sealed end will be removed and a segment of the microbore tubing will be fixed and fed to a waste container. At this point the microbubble diameter can be measured. Larger diameter microbubbles are typically better as a larger diameter resonator has a higher Q-factor and a larger diameter bubble will have a smaller wall thickness. To first order the wall thickness, Δr_f, is:

$$\Delta r_f = r_{of} - \sqrt{r_{of}^2 - (r_{oi}^2 - r_{ii}^2)} \qquad (4.2)$$

where r_{oi} and r_{ii} are the outer and inner wall radii respectively, and r_{of} is the final outer radius. This is based on simple conservation of mass for two infinitesimal cylindrical shells. However, this approximation slightly over estimates the final wall thickness at the center of the bubble. A microbubble with a 140μm radius is expected to have a wall thickness of 3.5μm, putting most of the microbubbles fabricated with this method well within the ideal wall dimensions of 2μm to 5μm. The typical bubbles fabricated range from 3μm to 3.5μm with some outliers down to 2μm. There was not strict adherence to this simple model and microbubbles were often found to be smaller than expected. This could result from flow physics and mass distribution or simply variation of the initial bubble dimensions.

4.3 Improving wall thickness aspect ratio

Methods for achieving a thinner wall thickness have been explored, but have not been successful in this work. The first alternate idea was to taper a larger diameter higher aspect ratio capillary to a smaller diameter. This was feasible, but tapering the capillary is difficult since any airflow can cause the capillary cavity to collapse and blowing the bubble was difficult in this geometry as the tapered region was very fragile. The second idea was to etch the original 80μm capillaries with buffered oxide etch to give a thinner starting diameter and wall thickness. In order to test the feasibility and etch rate of the buffered oxide etch on the capillary tubes, multiple sealed capillaries were submerged in buffered oxide etch for 90 minutes. Approximately every 30 minutes a tube was removed and broken and then measured using SEM. There is some discrepency in the initial wall thickness from the manufacturers specifications. The approximate etch rate for this geometry is 103.4nm/min.

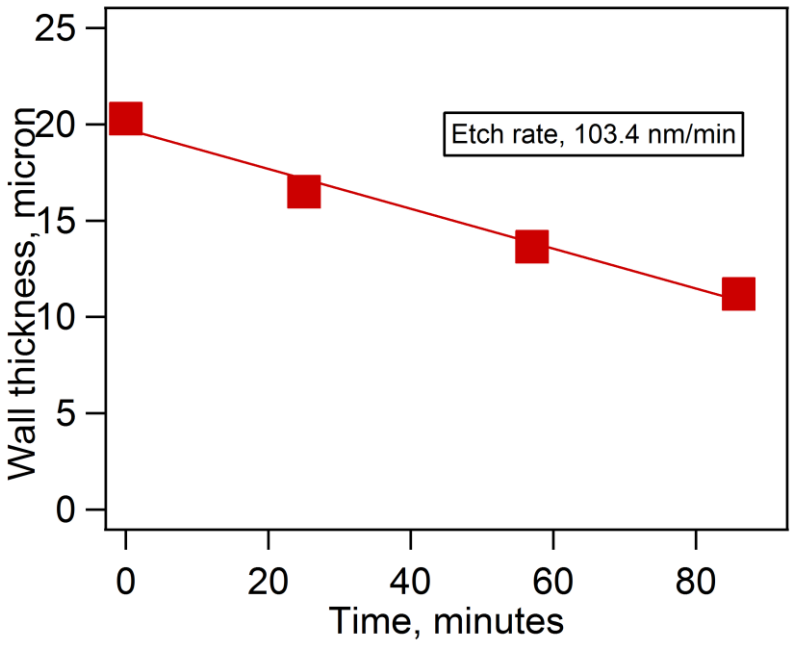

Figure 4.3: Etch rate of fused silica capillary tubes in buffered oxide etch.

4.4 Microbubble resonator mode spectrum.

After a microbubble resonator is fabricated it can be tested similar to any other whispering gallery mode resonator. A tapered optical fiber is brought to the equator of the bubble and light from a tunable laser is launched into the fiber and coupled to the bubble. The geometry of the experiment is similar to the rendering shown in Figure 4.4. The Q-factor and mode structure can be determined by analyzing the oscilloscope trace. The Q-factor of a typical empty microbubble resonator is $2x10^6$ with a relatively dense mode structure seen in Figure 4.5. By introducing different liquids into the microresonator the Q-factor and mode structure can change slightly. Liquids are pushed through the microresonator with a standard syringe. The waste is directed to a container and disposed. When ethanol is added to the microbubble resonator the Q-factor drops slightly to $1.5x10^6$ and the mode structure thins out as higher order modes are not coupled

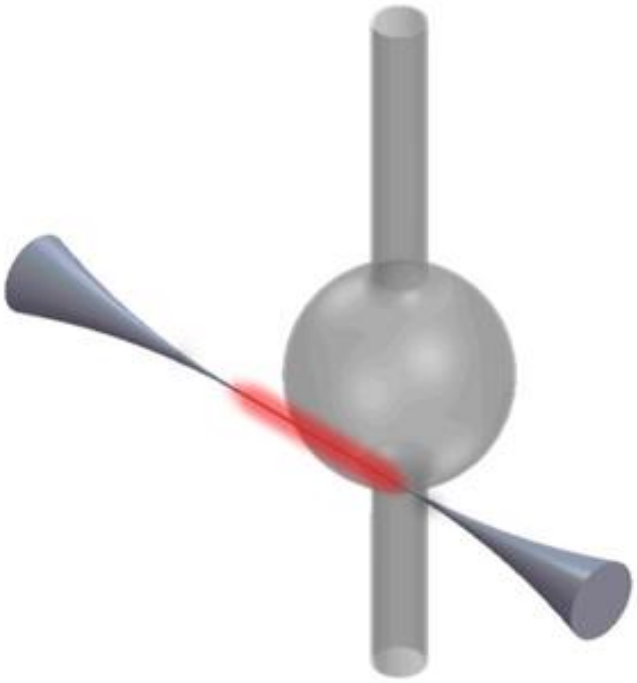

Figure 4.4: 3D rendering of microbubble and taper coupling experiment.

into as easily as seen in Figure 4.5. This very low reduction in Q-factor makes ethanol an ideal solvent for dyes in the microbubble resonator.

4.5 Microbubble resonator as a pressure sensor

The first experiment to perform when working with a microbubble resonator is to test for a dependence on input pressure. After fabrication this experiment is practically set up. The microbubble is mounted and left sealed at the end. It is then mounted on a 3D piezo translation stage and brought close to a tapered optical fiber. Light from a 980nm tunable laser (New Focus 6328) is used

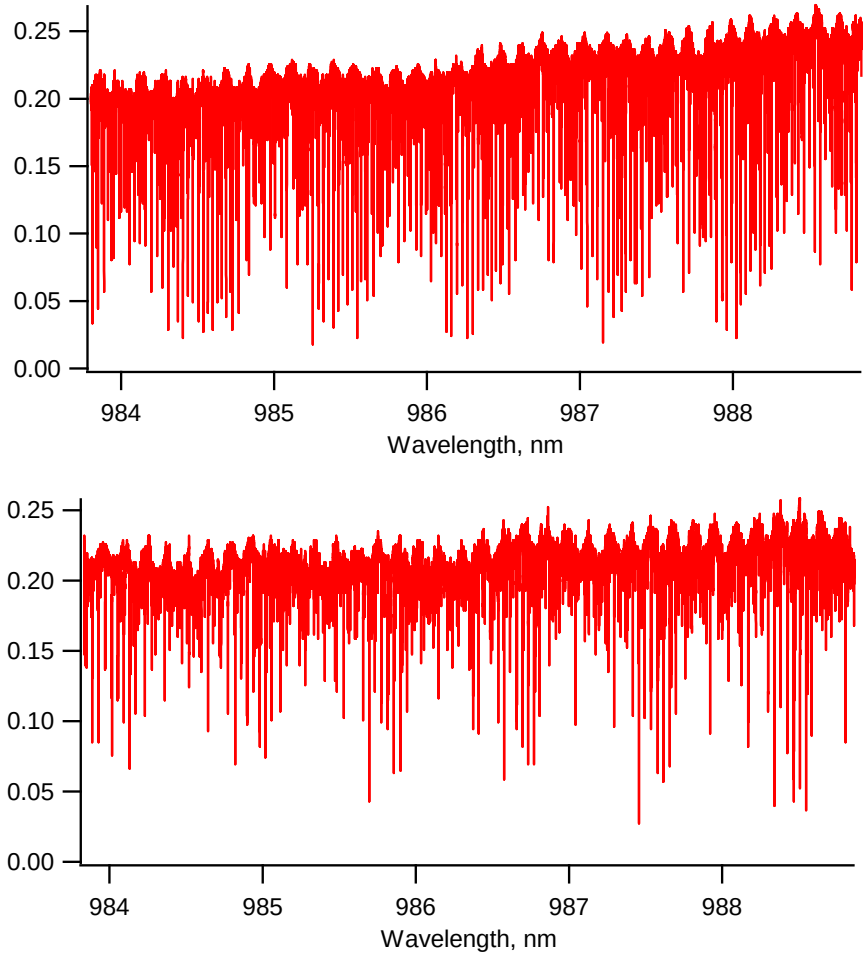

Figure 4.5: Top: Mode spectrum of empty microbubble resonator. Bottom: Mode spectrum of some resonator filled with ethanol. The initial Q-factor was $2x10^6$ when ethanol is added the Q-factor dropped slightly to $1.5x10^6$

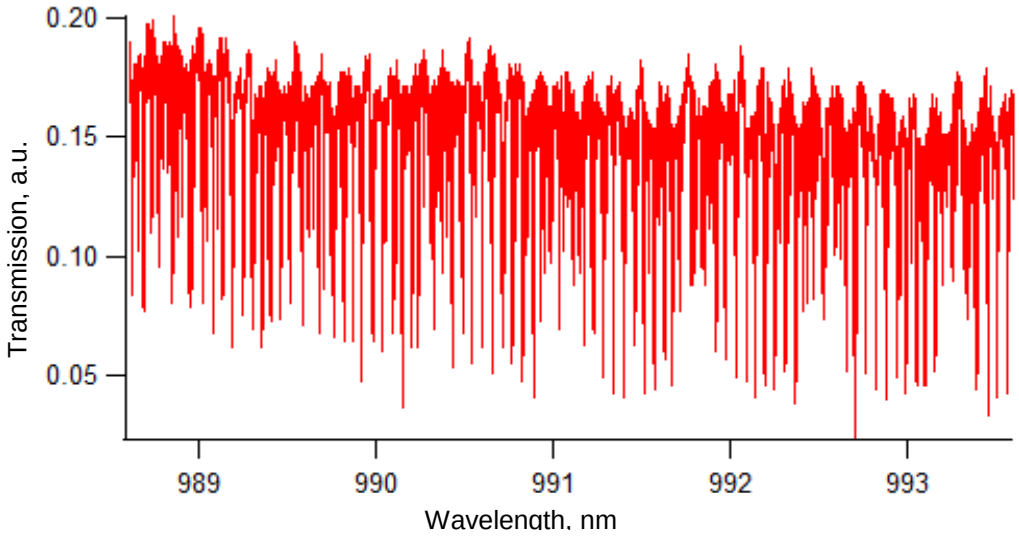

Figure 4.6: Mode spectrum of microbubble resonator used for pressure sensing.

to excite the resonances of the microbubble. The mode spectrum of the microbubble used for the data below is seen in Figure 4.6.

When pressure is applied to the microbubble resonator a change in resonance wavelength is expected. This is tracked by rapidly scanning the frequency of the laser using an external function generator. This captures only a handful of resonances as seen in Figure 4.7. Each sweep is captured by a computer and analyzed in a LabVIEW program. The software analyzes the trace and finds the location of the center of the peak. The applied pressure is also recorded with an on chip pressure sensor (MPX5050) and analog-to-digital converter. The pressure is swept up and down multiple cycles from 0kPa to 100kPa and the resonance center wavelength is recorded. The detuning from center as a function of pressure can be seen in Figure 4.8. The data is expanded in Figure 4.9 to show the tracking of wavelength and pressure with each cycle. The data points captured are fit to a line and show a correspondence of 0.2739picometers/kPa. The standard deviation of the fit is far lower than measureable with the equipment used, limited by laser stability and linewidth.

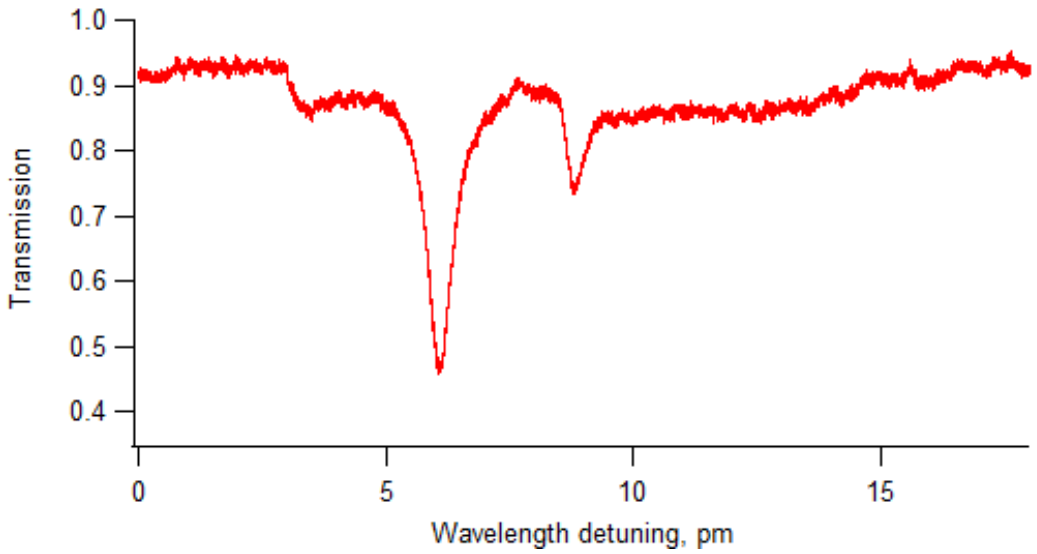

Figure 4.7: View of resonance seen when dithering wavelength frequency with function generator

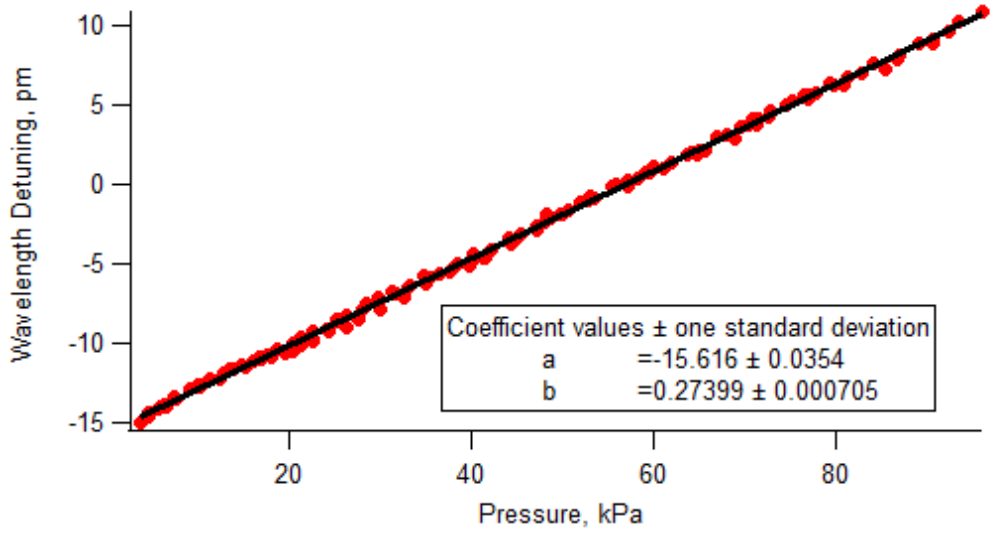

Figure 4.8: Wavelength detuning as pressure changes from 0 to 100kPa.

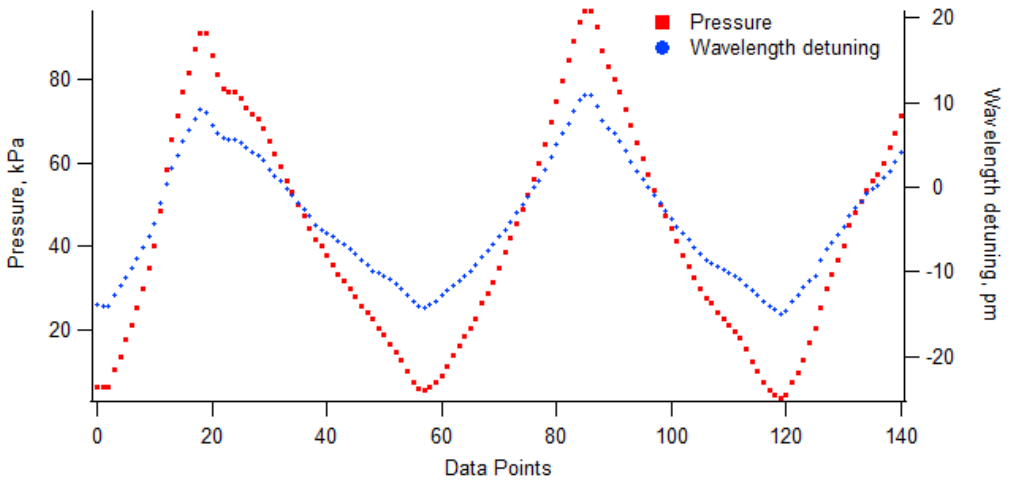

Figure 4.9: Pressure applied and wavelength detuning as a function of time. This shows the tracking of wavelength with the changing pressure over multiple cycles.

As the microbubble is pressurized it creates a change in the resonance wavelength. There are two primary candidates for this transduction: stress induced change in refractive index or a physical expansion of the radius of the microresonator. The most likely cause of this change is the physical expansion of the microresonator. We can estimate how much the resonator must expand by looking at basic resonator equations[6]. In this analysis, the free spectral range of the microbubble resonator in the frequency domain is:

$$fsr_o = \frac{c}{2\pi n R_o} \qquad (4.3)$$

The actual resonance frequency is an integer multiple, *m*, of the free spectral range:

$$f_o = m * fsr_o = m\frac{c}{2\pi n R_o} \qquad (4.4)$$

When the pressure changes we expect the radius to expand slightly causing a change in free spectral range:

$$\Delta f = m(fsr - fsr_o) = \frac{cm}{2\pi n}\left(\frac{1}{R_o+d} - \frac{1}{R_o}\right) = -\frac{cm}{2\pi n}\frac{d}{R_o(R_o+d)} = -f_o\frac{d}{R_o+d} \qquad (4.5)$$

In this case, d, is the deflection of the radius. This can be written as:

$$d = -R_o \frac{\Delta f}{f_o + \Delta f} \qquad (4.6)$$

The wavelength change in Figure 4.8 can be seen recast as a radius deflection in Figure 4.10. To further verify the source of the wavelength shift the physics of thin walled pressure vessel is investigated. The physics behind thin walled pressure vessels has been well analyzed for the field of gas handling[65]. Storage tanks for compressed gas use similar analysis. The stress on a pressurized sphere is:

$$\sigma_{sphere} = \frac{pr}{2t} \qquad (4.7)$$

where p is the pressure, r is the inner radius, and t, is the thickness. The increase in radius is then given by:

$$\Delta r = \frac{\sigma_{sphere} r(1-\nu)}{E} \qquad (4.8)$$

where E is the modulus of elasticity and ν is Poisson's ratio. Given the above equations[65] and the values in Table 4.1 the estimated elongation is 3.16nm which corresponds well to the total radius deflection based on the simplified free spectral range analysis shown in Figure 4.10 as 3.4nm. Improving the sensitivity of the microbubble pressure sensor can be achieved by increasing the radius of the resonator or decreasing the wall thickness.

Table 4.1: Parameters for estimating deflection of pressurized microbubble resonator

Parameter	Value
Sphere radius, r	132 μm
Internal pressure	96 kPa
Modulus of Elasticity, E	73 GPa
Poisson ratio, ν	0.17
Wall thickness, t	3 μm

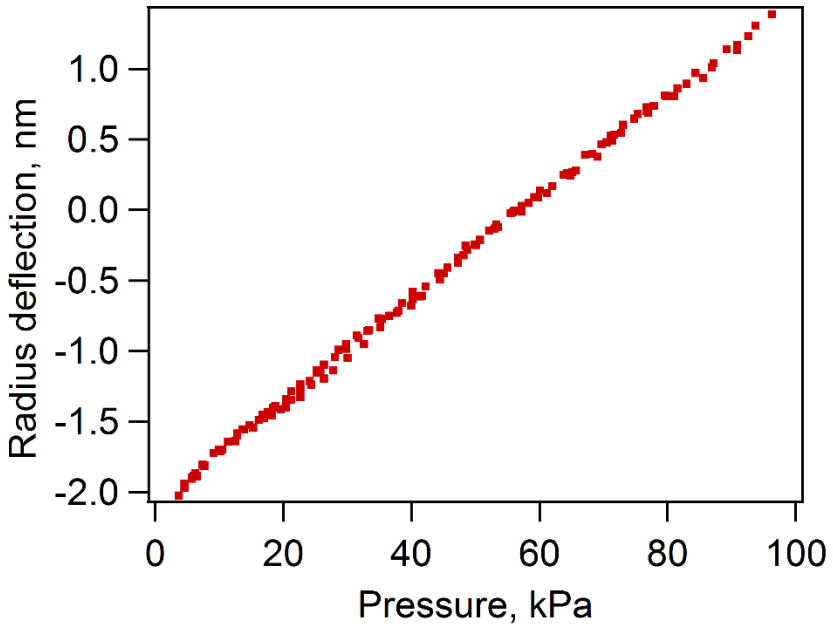

Figure 4.10: Radius deflection of microresonator as a function of pressure based on free spectral range calculations.

Chapter 5: Multi-photon absorption in microbubble resonators

5.1 Introduction

In this chapter we demonstrate two-photon fluorescence of Rhodamine 6G (R6G) in a microbubble resonator excited by a low power continuous wave 980nm laser diode. We rely on efficiently coupling light into the microresonator modes by means of an optimized tapered optical fiber to create a high intracavity field enhancement enabling access to the nonlinear photonics regime at extraordinarily low pump powers.

Two-photon fluorescence occurs when a molecule simultaneously absorbs two photons of light and is subsequently excited to a real energy state or band rather than a virtual energy band as in harmonic generation [66]. The efficiency of two-photon excitation depends largely on the two-photon absorption cross section of the specific molecule. Two-photon cross sections have been measured and cataloged thoroughly and accurately by multiple sources [67,68]. A thorough analysis of two-photon fluorescence of a Gaussian beam focused on a sample has been done by Xu and Webb [68]. They have derived a square law dependence of measured fluorescence on pump power for single-pass two-photon absorption:

$$\langle F(t)\rangle = \frac{1}{2}\phi\eta_2 C\sigma_2 \left\langle \frac{P_0}{A} \right\rangle^2 \int_V dV S^2(\boldsymbol{r}) \qquad (5.1)$$

where ϕ is the system's optical collection efficiency, η_2 is the two-photon fluorescence quantum efficiency, C is the absorber concentration, σ_2 is the two

photon absorption cross section, and S is the spatial distribution of light interacting with the two-photon absorber.

External cavities have been frequently used to increase the efficiency of nonlinear optical processes. Common applications of external cavity resonators include doubling for UV laser sources [69–71]. The concepts of external cavity nonlinear optics apply to the current experiment and can be used to better interpret the observed phenomena. The free space external cavity is analogous to the high-Q microbubble resonator where instead of second harmonic generation (SHG) from a crystal, two photon-absorption of R6G dye produces radiation through fluorescence.

The field enhancement of the circulating power and field localization due to the small mode volume in high-Q microresonators allows for much higher nonlinear conversion efficiency as compared to single pass operation. For the analogous case, the pump power dependence for SHG does not follow an exact square law as expected in single pass operation due to nonlinear losses in the cavity and pump depletion. The rigorous formulation of external cavity SHG for Gaussian beams was originally derived by Kleinman and Boyd [72]. The circulating power inside a simple resonator with a non-linear loss element is given by:

$$P_{circ} = P_i \frac{1-K}{\left(1-\sqrt{K(1-\delta-\gamma P_{circ})}\right)^2} \qquad (5.2)$$

where K relates to coupling coefficients, δ are the linear round trip losses, and γ corresponds to the nonlinear conversion efficiency. All of these terms can be directly related to the resonator Q-factor. In this situation we have an implicit dependence on circulating power which interacts with the nonlinear element on

the pump power, P_i. As pump power increases the effective Q-factor of the resonator decreases lowering the overall efficiency of the nonlinear process.

In the two photon absorption case the so-called non-linear conversion efficiency depends on the two-photon absorption cross section, absorber concentration, and spatial interaction volume. By evaluating the integral as the whispering gallery mode volume interacting with the core, we can cast this conversion efficiency as:

$$\gamma = C\sigma_2 \frac{(\pi D)^2}{V_{eff}} \Gamma \qquad (5.3)$$

Where V_{eff} is the resonator mode volume, Γ describes the confinement of light in the liquid core region of the resonator, and D is the resonator diameter.

5.2 Methods and results

The microbubble resonators used in this experiment are fabricated by an arc discharge method similar to Berneschi et al. [60]. The microbubbles are formed from a fused silica capillary tube with 50μm inner diameter and 80μm outer diameter. The capillaries used are supplied by Produstrial. The capillary is capped at one end by fusing it with an optical fiber fusion splicer (Fitel S148). The capillary is then cleaned thoroughly with ethanol, pressurized to approximately 50kPa, and then subjected to the electric arc generated by the fusion splicer. The glass becomes molten around the arc region and expands to form a bubble due to the pressure differential inside the capillary. Microbubble resonators fabricated in this fashion typically have a diameter between 200 μm and 300 μm and a wall thickness between 1 μm and 5 μm.

Light is coupled into the microbubble resonator by evanescently coupling light from a tapered optical fiber into the whispering gallery modes supported by the microbubble resonator as described by Knight [19]. The tapered fibers used are made from Fibercore SM800 fiber for single mode operation at 980nm. Tapering is performed with a flame brushing rig made with primarily 3D-printed parts [43]. Two of the computer controlled 3D-printed stages slowly pull the fiber while a third stage brushes a butane torch across the fiber to define the waist region. The effective hot zone can be varied during the tapering process to generate different taper profiles. The tapers used in this experiment are made with a constant hot zone of 10mm and pulled such that the waist diameter is on the order of 3μm [31,73]. The Q-factor of the resonator is calculated by measuring resonance linewidth with a tunable laser source (New Focus TLB-6320 Velocity Tunable Laser). The microbubble resonators tested and used for this experiment had a typical Q-factor of $2x10^6$ at 980nm.

A $5x10^{-3}$ M solution of R6G dye was prepared in an ethanol solvent. R6G was chosen as a model dye for its reasonably high two-photon absorption cross section at 980nm and high fluorescence efficiency [67,68]. Both ends of the

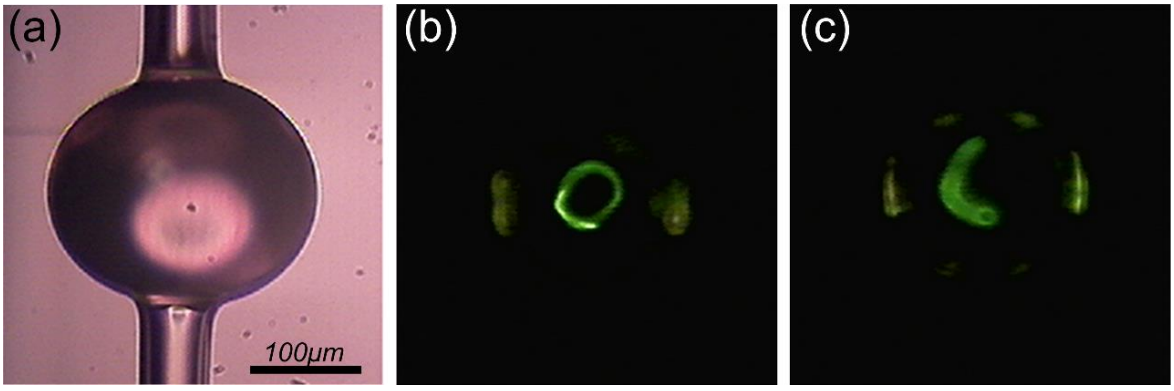

Figure 5.1: Left: Microbubble resonator mounted after fabrication. Middle and right: Microbubble resonator excited with 980nm pump light. The dye undergoes two-photon absorption and fluorescence generating green-yellow fluorescence along the light path. The center is the point of contact between the taper and the resonator. This coupling point is a major scattering point creating a green ring effect when imaged.

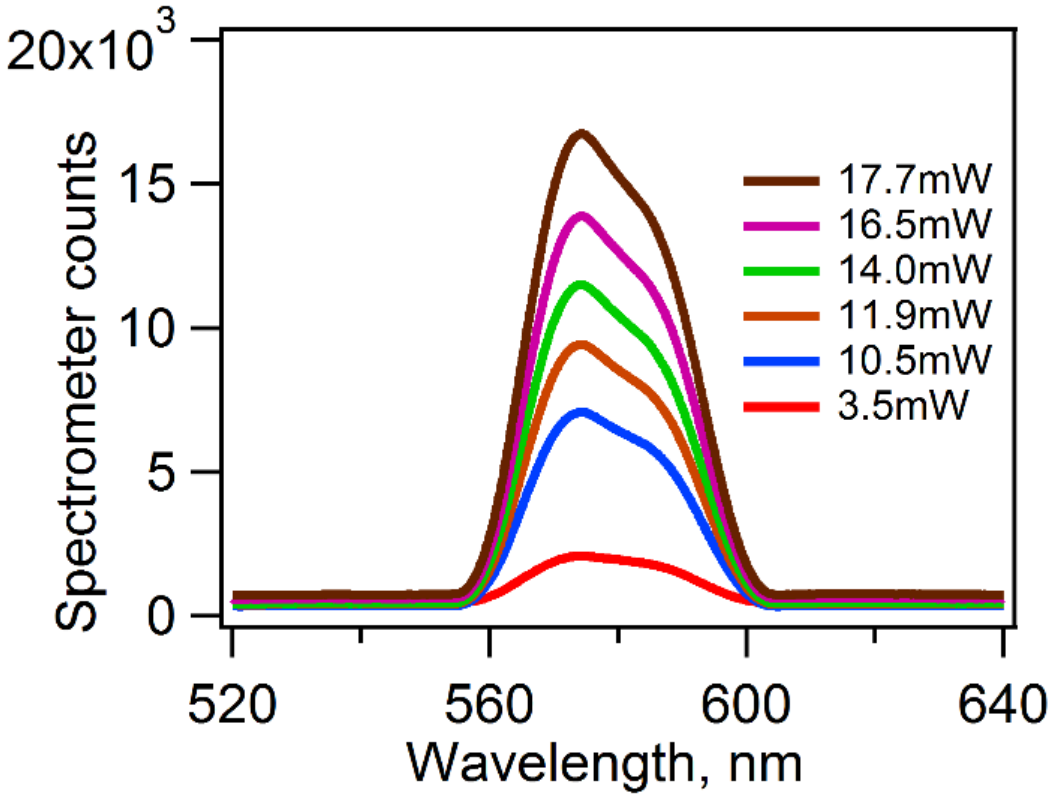

Figure 5.2: Spectrum of two-photon fluorescence of Rhodamine 6G with increasing pump power measured with an Ocean Optics spectrometer

microbubble are attached to Tygon® Microbore tubing with UV cure epoxy. One end of the tubing was connected to a syringe to slowly flow the R6G solution through the bubble. The solution is slowly flowed through the resonator at a rate of approximately 20 microliters per minute and fed into a waste container at the opposing end. The slow flow rate is due to the small diameter of capillary tube limiting flow.

The microbubble resonator is affixed to an XYZ piezo stage and brought to the waist region of the tapered optical fiber. The system is pumped by coupling light from a 980nm laser into a resonant mode of the microbubble. The system operates in the overcoupled regime with the tapered fiber in contact with the resonator to ease alignment of the system. The R6G dye solution is flowed through the bubble while the resonator is being pumped. Field enhancement from the high

Q-factor of the microbubble generates green-yellow light from multi-photon fluorescence of the dye.

The two-photon fluorescence is first visible to the naked eye at external pump powers as low as 700μW. This input pump power corresponds to a circulating power of approximately 200mW inside the resonator. The mode volume of a spherical microresonator can be approximated as:

$$V_{eff} \approx 3.4\pi^{\frac{3}{2}}\left(\frac{\lambda}{2\pi n}\right)^3\left(\frac{\pi n D}{\lambda}\right)^{\frac{11}{6}} \qquad (5.4)$$

as given by Braginsky et. al.[17]. In the case of the microbubble resonator filled with solution the mode volume can be roughly estimated as $1x10^{-8}cm^3$. This corresponds to a localized intensity of approximately $1.5MW/cm^2$.

Light from the two-photon fluorescence signal emitted by the microresonator is collected with a 0.1NA objective lens and analyzed using an Ocean Optics USB4000 spectrometer. The lens images the microbubble onto the spectrometer's collection fiber, and the light from the fluorescence signal is isolated using a short pass filter with a cut-off wavelength at 700nm (Thorlabs FESH0700). The measurements are taken with no background signal present. The spectrum is recorded with a 5 second integration time and 30 pixel boxcar smoothing. As the pump power is increased the measured fluorescence signal increases with a nonlinear dependence on pump power as expected for a two-photon fluorescence process. Figure 5.1 shows images of the experiment in progress with a CCD camera in place of the Ocean Optics spectrometer fiber.

When the microbubble resonator is pumped, light is coupled into a whispering gallery mode supported by the resonator; the thin wall of the microbubble allows the supported modes to extend into the hollow cavity. When

the microbubble cavity is filled with dye, resonator-enhanced two photon absorption occurs in the R6G molecules which subsequently fluoresce, with the fluorescence centered at 580nm with a 40nm width. The multi-photon spectrum seen in Figure 5.2 is close to that expected from R6G under single-photon pumping [67]. Note that as the pump power is increased the shape of the spectrum is retained. The fluorescence signal has a nonlinear dependence on pump power as expected with this process and is shown in Figure 5.3. The logarithmic trend of the fluorescence displays a slope of 1.51.

5.3 Discussion and analysis

Deviation from a perfect square-law dependence of fluorescence on pump power is due to nonlinear cavity losses as described above. The measured power dependence was fit to the proposed theory by combining 5.1 and 5.2. For the fitting routine 5.1 was generalized to:

$$\langle F \rangle = \frac{1}{2} A\gamma \langle P \rangle^2 \qquad (5.5)$$

This simplification is adopted to account for the parameters that cannot be accurately measured. The A term relates to the system parameters which include collection efficiency and spectrometer calibration. The γ term of (3) relates directly to the two-photon conversion efficiency and has units of W^{-1}. The computed fit matches well to the observed data. The fit parameter γ_{fit} was found to be 1.6×10^{-13} W^{-1}. This corresponds well with a calculated γ of $6 \times 10^{-14} W^{-1}$. While there is very little theoretical work on resonant enhanced two-photon fluorescence, similar experimental dependences on pump power are reported in external cavity frequency conversion experiments[74].

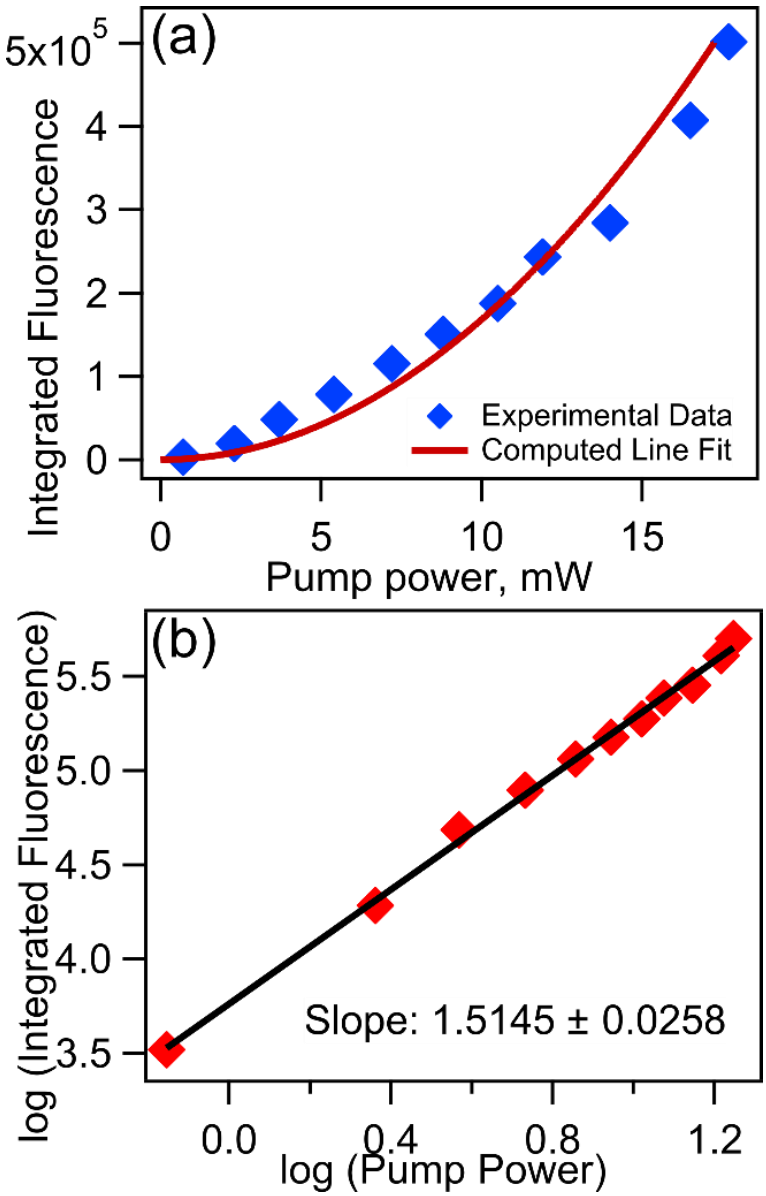

Figure 5.3: Top: As the pump power is increased, the total two-photon fluorescence signal generated increases non-linearly as expected for this process. Bottom: Log plot shows a non-linear power law dependence of 1.51

Some intriguing effects have also been observed due to secondary effects in the liquid. When the pump power is in excess of approximately 30mW, absorption induced heating causes the ethanol solvent to vaporize, creating gas bubbles. The complicated spatial dependence of the refractive index at the dynamic gas-liquid interface alters the mode structure of the resonator, increases scattering, and

creates excess loss which hinders the efficiency of the two-photon fluorescence process.

At much higher pump powers, around 80mW, we have observed a bright red glow from the resonator which ends with the tapered optical fiber breaking. This occurs on the time scale of approximately one minute and further experiments are planned to understand the origin of this phenomena. Due to the damage, glow, and other thermal effects at lower pump powers it is hypothesized that this is the effect of intense localized thermal heating of the resonator.

There was no evidence of line narrowing or mode filtering during the experiment to suggest that lasing was occurring. Modeling and previous work indicates that to achieve lasing higher peak power pumping will be necessary to provide gain while keeping a low average power to avoid unwanted thermal effects[75,76]. This can also be achieved by a higher resonator Q-factor and by reducing the diameter of the resonator to further decrease the mode volume and thus increase the localized field intensity.

We have demonstrated efficient generation of two-photon fluorescence signals easily visible to the human eye. This work gives better understanding of the interaction between light confined in whispering gallery mode resonators and nonlinear optical materials and liquids. Experimental limitations and undesirable effects which can arise when using liquids in microfluidic resonators have been identified, namely gas bubble formation and absorption induced heating, which will be the subject of further study.

Chapter 6: Digital image analysis of diatom frustules

6.1 Introduction

Diatoms are a type of ubiquitous phytoplankton which produce cell walls, called frustules, composed of nanostructured silica. The diatom frustule is composed of two valves and a series of connecting girdle bands. Valve structures in particular can have highly complex fundamental structure and ornamentation[77]. Characterizing the morphology of diatom frustules is important in understanding the biology of this class of organisms. Structural characteristics of the frustule have been implicated in providing robust mechanical properties[78,79], concentration of nutrients[80], adhesion[81] and interaction

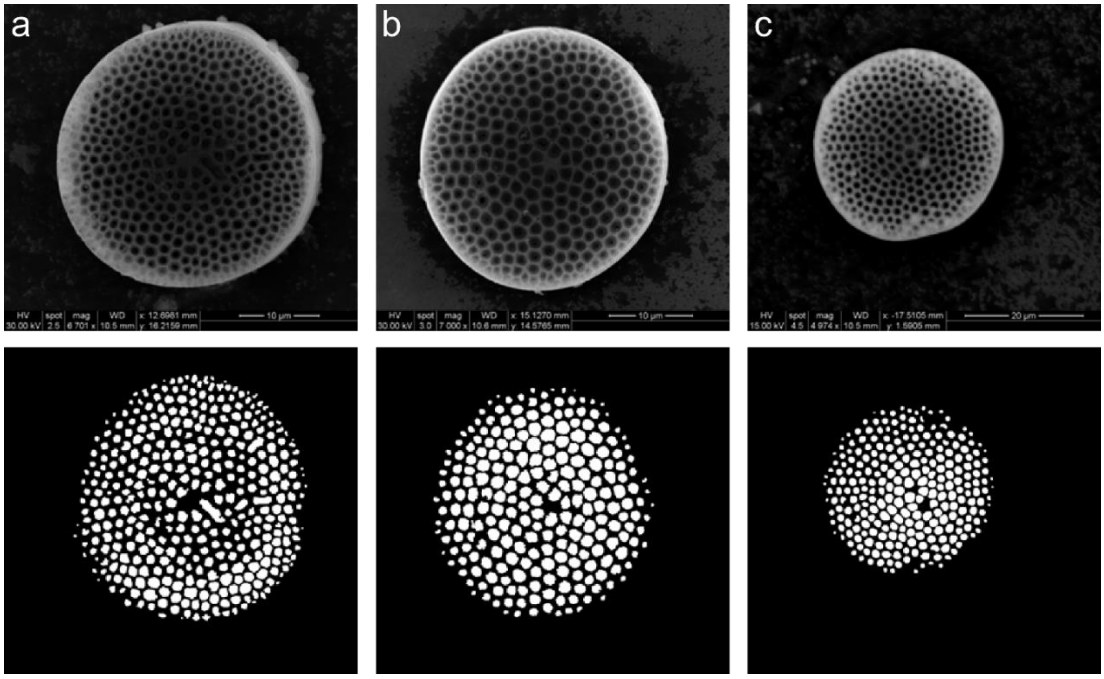

Figure 6.1: Top row: SEM images of *Coscinodiscus radiatus* diatom frustules. Bottom row: corresponding threshold binary images generated by our analysis.

with light [82–85]. Most valve morphology characterization is based on manual measurements of pore spacing and relative position to other key features of diatom valves and qualitative descriptions of valve structure[77,86,87]. These measurements can be adequate in many scenarios, but lack information from the full valve surface as well as substantial statistics of the feature measurements. They might also be subject to more variability related to the human factor making the measurements. Here, we have developed a digital image analysis to provide a systematic computer-based method of quantifying diatom morphology. The scope of this manuscript focuses on the ultrastructure of diatom valve pore-networks.

This manuscript examines the frustule ultrastructure as it best portrays the described technique's ability to handle a large number of pores with minimal outside intervention. Imaging and performing analysis on the nanostructure of some diatoms, such as Coscinodiscus wailesii, is possible. However, it requires destruction of the outer valve or is limited to small glimpses of the nanostructure through the pores of the ultrastructure. Imaging through the larger pores allows only a handful of pores for analysis and lacks insight into the large scale pore patterns and trends. We do show this technique is suitable for diatoms of any size from *Coscinodiscus rothii* (approx. 75 μm) and *Coscinodiscus radiatus* (approx. 30 μm) to *Thalassiosira pseudonana* (approx. 3 μm with nanometer features) and can adequately analyze the nanostructure of diatom species with suitable images.

Our primary interest in this research is to analyze diatom valves with periodic pore network structures. Pore networks are a description of how the pores of a diatom valve are distributed with respect to each other. Diatoms with periodic pore network structures, such as *C. wailesii*, have shown unique optical filtering properties[82] dictated by their microscopic pore structure. Having complete knowledge of the valve structure can improve simulations required to

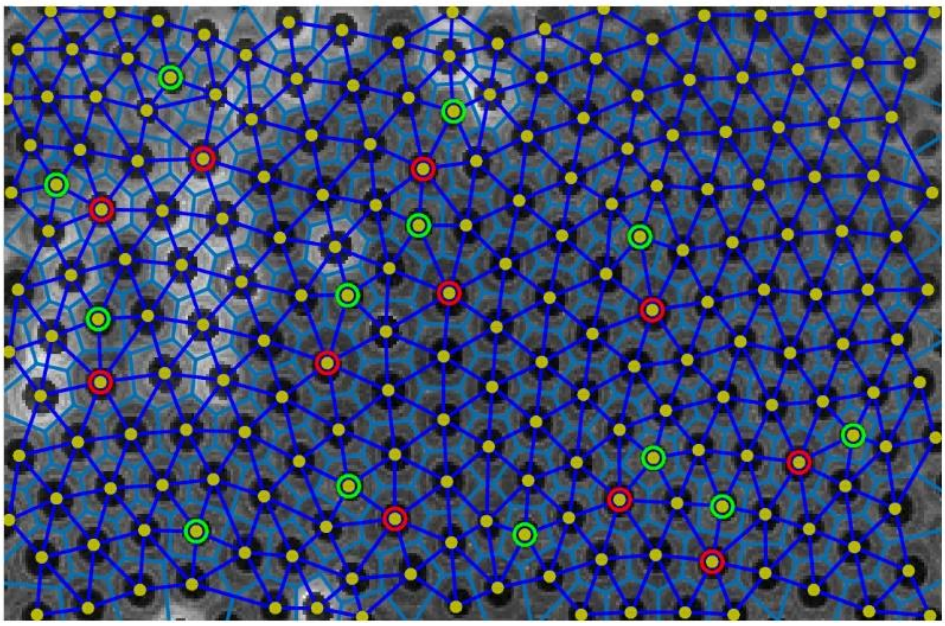

Figure 6.2: Inset of *Coscinodiscus wailesii* showing how connections are made and pore spacing. Each pore identified is marked and Delaunay triangulation connections are made in dark blue lines; the reciprocal Voronoi polygons are drawn with teal lines. Pores with 5 edge connections are outlined by a green circle and 7 edge connections are outlined by a red circle.

classify the photonic properties of the diatom valve[85]. These photonic properties may ultimately bear on the diatom's light gathering strategies for photosynthesis.

6.2 Methods

We use a set of numerical routines to analyze the different aspects of the periodic structures in diatom valves. The software routines extract pore location data from raw images of diatom valves and use this data to generate a lattice which connects each pore. The generated lattice is a mathematical graph which contains statistical information on pore spacing as well as defect pore locations in diatoms with periodic pore networks. This information can be used to describe the morphology of the diatom valve in a statistically rigorous fashion.

The structures of the diatom frustules are complex and require customized image processing techniques to be used for each studied diatom species. The same tuned algorithm will work for images of diatom valves from the same species

imaged under similar conditions. The images are typically acquired through scanning electron microscopy (SEM), but depending on the size of the species suitable images are also possible through optical microscopy[77,88,89]. The optical microscope images used were originally published by other groups in open repositories such as Plankton*Net by the Alfred Wegener Institute for Polar and Marine Research[90].

The raw grayscale images are converted to a segmented binary image[91] by thresholding the image. Ideally, the final binary image highlights the individual pore locations on the diatom frustule. The images gathered using SEM microscopy can have poor consistency with image contrast varying across the extent of the diatom valve. This is due to their large size and susceptibility to charging effects even under high vacuum and with gold coating.

The image segmentation routine isolates individual pores consists of an adaptive thresholding operation and, if necessary, a set of other common image processing routines in order to best isolate the pores in the image. Thresholding is a common technique used to segment digital images by converting a grayscale image to a binary image[92]. Each pixel in a grayscale image has a value which describes its intensity. When thresholding an image a pixel intensity cut off value is selected. Intensity values above this value are given a value of 1 and below the threshold value are given a value of 0. The threshold value is chosen to best segment the foreground from the background or isolate specific objects in the images. In many cases a single value can be used to segment an image, but in complex scenes with varying contrast across the image it is necessary to use an adaptive thresholding algorithm.

Adaptive thresholding algorithms generate individual threshold levels for each pixel in an image based on the local pixel intensity statistics of the image[92].

There are many available adaptive thresholding methods which work well for segmenting images of diatoms[93,94]. The adaptive thresholding we typically used for diatom pore segmentation is based on a sliding window that calculates the mean value of neighboring pixels. The local mean is then scaled to find a local threshold value which best segments the pores. This threshold scaling factor can be chosen or determined systematically by further analysis of local pixel statistics. For example, a good threshold value can be set as one standard deviation of pixel intensity below the mean. This simple method allows for adequate segmentation despite uneven contrast across the image by effectively normalizing the image contrast across the diatom valve. A second technique employed is to choose a threshold level based on the local minimum and maximum pixel intensities. In general, the specific routine parameters are customized for each diatom species to optimize pore segmentation.

The least amount of image processing operations should be performed to segment the image. Ideally, simply thresholding the image should isolate the pores, but this is usually not the case. Erosion and dilation routines can be performed to further segment the pores[92]. After the pores are well isolated, the most effective final step is to clean the image by filtering regions by area which removes lone pixels and larger areas which are obviously not pores. This requires some previous knowledge of pore size statistics; aggressive area filtering may not be suitable for certain applications.

After a suitable binary image is attained, it is analyzed to find the spatial location of each pore by identifying the centroid of each pore region isolated through the segmentation process. A Delaunay triangulation algorithm is run using the centroid data of each pore to generate graph edges between each pore. The triangulation algorithm generates triangles from a set of provided points that

form a connection between the points. It chooses the triangles in such a way that maximizes the smallest angle in the triangle; in other words, it tries to make triangles which are as close to an equilateral triangle as possible among the given points. The triangulation algorithm connects edges to points by forming circles by a set of three points. If there are no other points within the circle it connects these points with the edges of a triangle[95,96]. This forms a lattice of spatial points and non-crossing edges which enable us to analyze the resulting graph and gain quantitative insight into the morphology and quasi-periodic structure of the diatom frustule.

The two main parameters that describe the pore network structure of the diatom are pore spacing and regularity. The best visualization of periodicity comes from examining the graph's regularity. Regularity refers to the number of connections per node. In this case, deviations from the standard number of connections refer to an irregular node. The regular lattice configuration of the pores in *C. radiatus*, *C. rothii*, and *C. wailesii* is a hexagonal point symmetry. Hexagonal symmetry is one of the five two-dimensional point group symmetries[97]. In other words, it is possible to fill a plane with a hexagonal lattice of points similar to the pore network structure of certain diatoms. Symmetry breaking occurs when the hexagonal symmetry is compromised by substantial variation in the pore spacing in localized regions on the valve surface[98]. These pores can be identified by counting the number of pore-to-pore connections determined through the Delaunay triangulation. Defects pores typically present themselves in pairs of five and seven connections which significantly deforms the surrounding hexagon patterns from their regular shape and influences the overall periodic structure of the valve[95].

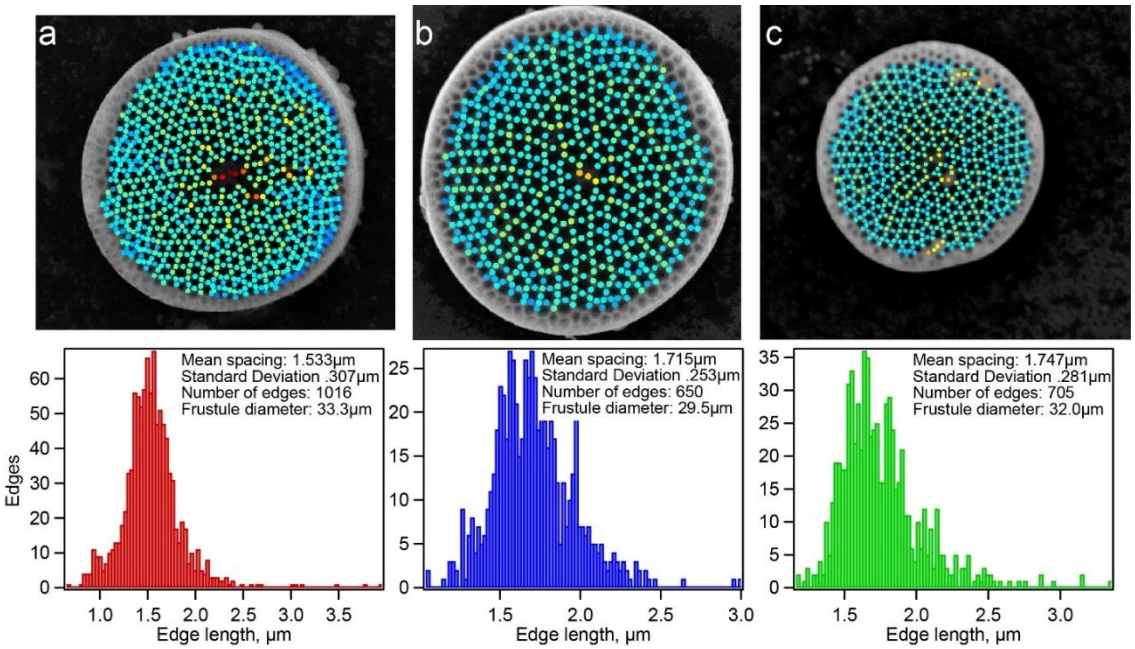

Figure 6.3: Heat maps, histogram, and statistical data of *Coscinodiscus radiatus* diatoms analyzed from Figure 6.1 images. The length to pixel scaling for each image is 43.1 nm/px, 41.3 nm/px, and 74.3 nm/px respectively.

Alternatively, these pores can be identified by generating a Voronoi diagram of the pore network. Voronoi diagrams are the dual graph to the Delaunay triangulation calculated from the pore locations. The Voronoi diagram is generated from the Delaunay triangulation by drawing perpendicular lines which bisect each edge of the Delaunay triangulation. Each node of the Voronoi diagram will be found inside the face of each triangle of the Delaunay triangulation[95,96]. This graph is analogous to the Wigner-Seitz cell of a Bravais lattice used in crystallography to describe similar periodic lattices[97]. The polygons which compose the Voronoi diagram enclose each physical pore of the diatom valve and represent the set of points closest to the encapsulated pore. For a regular six-fold lattice the Voronoi polygon which encloses the pore will be hexagonal in shape, when the Voronoi polygon has five or seven sides the site can be labeled as a defect[98].

6.3 Results

This technique has been applied to images of multiple different diatoms which best demonstrate the effectiveness for extracting different types of data from the diatom valve structure. Diatoms have been chosen which accentuate the technique's ability to extract pore spacing information and best visualize the defect pore locations.

Coscinodiscus radiatus was used to generate statistics of the pore spacing distribution across the diatom valve surface. *C. radiatus* has a simple hexagonal pore network structure with relatively stable parameters. The simple regular structure will make any deviation from the normal spacing apparent. The *C. radiatus* samples used were obtained from the National Center for Marine Algae and Microbiota and further cultured at the University of Arizona. Multiple *C. radiatus* from the same culture were imaged using SEM. The images have been analyzed and results are displayed in Figure 6.3. The original image and threshold image of the same diatoms are also seen in Figure 6.1. The original image is overlaid with a point heat map. Each point corresponds to an edge and the shade corresponds to the distance between each pore center. Light points represent shorter edges and more dark points represent longer edges relative to the scene (Figure 6.3). Each diatom is accompanied by a histogram of edge length along with statistical information on their edge distribution in Figure 6.3. This technique can generate a large number of sample edges which provides accurate statistics on the mean pore spacing. The standard error of the mean pore spacing for the three *C. radiatus* valves analyzed varies from 9.6nm to 10.6nm depending on the frustule.

Certain diatom frustules have some curvature to their surface which may slightly effect the actual measured pore spacing across the entire valve. If necessary, this can be accurately accounted for by projecting the two dimensional

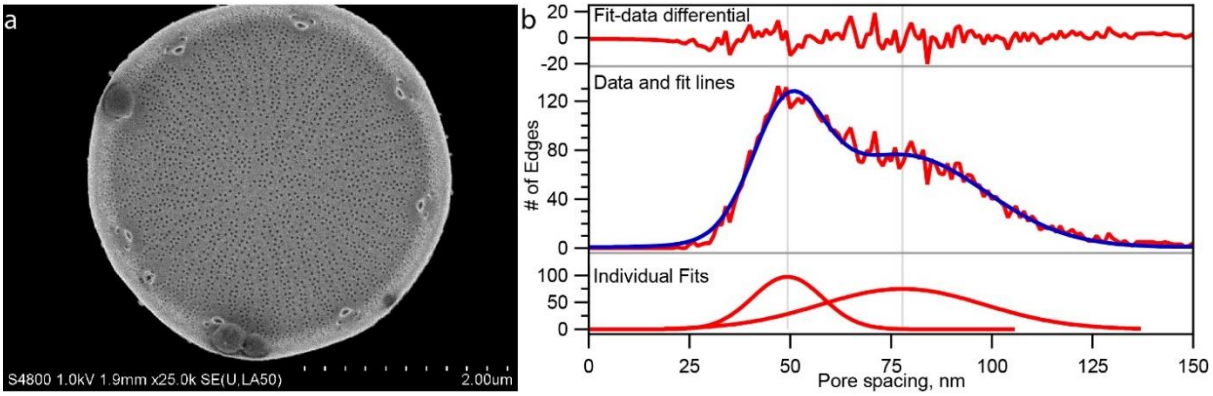

Figure 6.4: a) *Thalassiosira pseudonana* SEM image used for our analysis. B): Results of multi-peak fitting routine performed on the pore spacing distribution histogram obtained from the above image of *T. pseudonana*. The fit-data differential displays the difference between the real data and the fit. The individual peak fits panel displays the distributions fit to each individual peak. Each peak corresponds to a different class of pore spacings as described in the main text: pore-to-pore and track-to-track spacing.

image and spacing data onto a surface height profile of the diatom frustule obtained by atomic force microscopy or another form of 3 dimensional or stereoscopic imaging. Both *C. radiatus* and *C. wailesii* are known to have a flat valvar surface and narrow mantle nearly orthogonal with the valvar surface[99–101]. The mantle region is poorly imaged with a top down perspective in both diatoms. In *C. radiatus* the mantle contains only one or two rows of pores[99] and is largely not included in the above statistics. These pores are not included due to poor image quality and the different morphological role of the mantle and valvar surface. Pores which have been inadvertently included in the statistical analysis contribute to the sampling error. This is quantified as a component of the standard error.

Thalassiosira pseudonana was used to demonstrate the ability of this technique to analyze diatoms with pore network structures which do not exhibit a regular periodic pattern. This species has been extensively studied and was the first diatom species to have the full genome analyzed[102]. *T. pseudonana* is a smaller diatom with a diameter of 3 – 4 μm. The valve has large portulas around

the rim and a series of nanometer scale train-track like pores that are directed across the valve surface[87]. The pore network on this diatom lacks the periodic layout seen in the other diatoms we have analyzed so far. For *T. pseudonana,* the analysis has shown that there are two distinct spacing classes: between the pores of the track and between the tracks themselves. The distribution of pore spacing is analyzed using statistical analysis software with multi-peak fitting capabilities. The mean spacing of the pores in individual tracks was found to be 49.3 nm. The distribution of edges which connect pores between each individual track corresponds to 77.9 nm. The original SEM image and statistical data are seen in Figure 6.4. Identifying these two pore-spacing classes can be used as a morphological signature to highlight variation within the species.

Optical microscope images of *Coscinodiscus rothii* were used to visualize defect pores across the entire valve surface. The images used for analysis are by Stuart Stildoph as part of The Stuart R. Stildoph Diatom Atlas and were acquired from Plankton*Net repository[90]. The defect pore locations are identified and marked in red and green (Figure 6.5). The red and green markers correspond to pores with seven and five neighboring connections, respectively. The analysis of this valve brings forward a spoke-and-wheel like structure outlined by the marked defect node connections. It also shows a higher defect density at the center of the valve.

6.4 Discussion and conclusion

The technique presented above has the ability to accurately gather a large scale of statistical information which describes the morphological structure of diatom frustules through image processing and computational geometry. All the image processing and geometrical analysis is done using MATLAB, but can easily

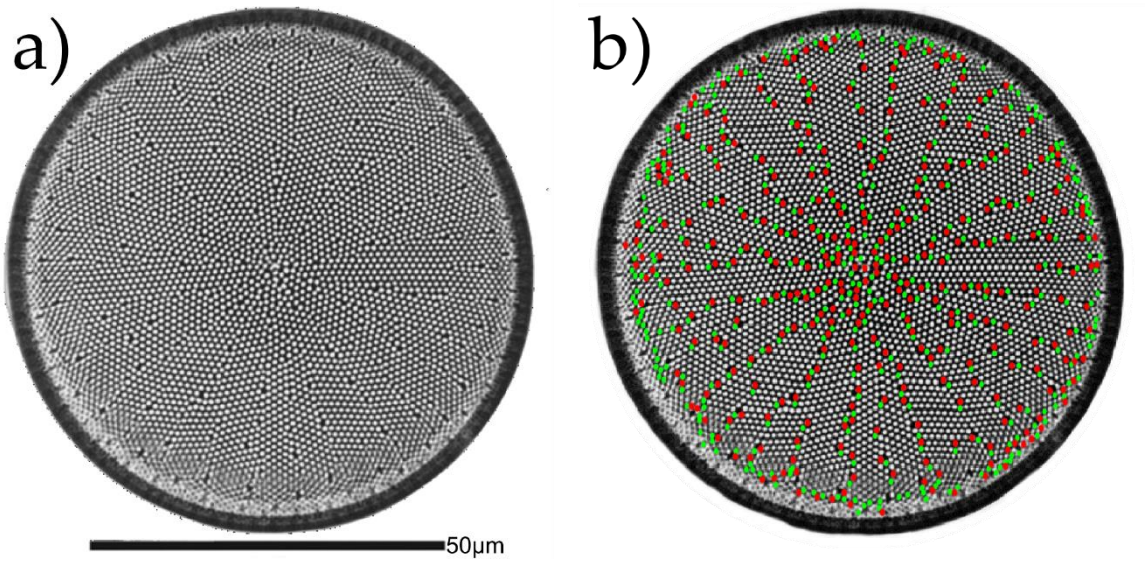

Figure 6.5: Top: Microscope image of *Coscinodiscus rothii* photographed by Stuart Stildoph [90]. Bottom: Analyzed image showing defects in the diatom and slice like structure of periodic regions of pores in the valve. The red and green defect locations correspond to the same labeled defect Voronoi polygons as in Figure 6.2.

be implemented in other languages which have image processing and computational geometry packages available. The data collected can help scientists approach the morphology of diatom species in a statistically rigorous manner. Analysis of diatom morphology is important for taxonomic classification and differentiation of diatom species[103,104]. The ability to generate robust statistics is also relevant to improving sediment analysis for climate change and environmental studies[104,105]. With a full database of statistics describing diatom species under study researchers can identify variations in diatom morphology due to changes in environmental growth conditions[106–108].

It has been established that pore spacing and position are directly related to the optical properties of the diatom[82–84]. A map of the physical structure of specific diatoms can be used to better estimate photonic properties of diatom frustules. Analysis of biological functions and cell organelles is possible by the application of other imaging techniques such as multi-photon[109] or confocal fluorescence[110,111] microscopy. Coupling these other imaging modalities with

a structural map of the diatom could unlock further information regarding the biological functioning of the diatom cell[112].

This framework for analyzing diatom morphology is a novel powerful method for understanding the biology of diatom species. It has the ability to improve diatom research by providing accurate statistics on diatom morphology. There are numerous applications that can benefit from our analysis, ranging from biology and environmental science to optics and photonics.

Chapter 7: Photonics simulations and visualization of diatom structures

7.1 Introduction

As described in the previous chapter diatom pore morphology constitutes a unique structure that resembles a man-made photonic crystal. Photonic crystals are periodic structures of real dielectric constant materials (i.e. lossless insulators such as glass) on a micron scale that effect the propagation of light through the structure. This can be a simple one-dimensional structure like a thin film stack, or a more complex patterned two dimensional structure. The analysis of photonic crystals mimics that of the traditional semiconductor physics of real crystals where the optical lattice is analogous to a potential well lattice and EM wave propagation is analogous to electron wave propagation. In fact, the wave equation describing waveguide modes takes the same form as the Schrodinger equation where the index of refraction, n, takes the place of potential, V.

Photonic crystals can be fabricated as a single crystal or defects can be incorporated into the structure to create waveguides and optical cavities. Optical cavities are formed in two-dimensional photonic crystals by removing a hole or locally changing the spacing of the holes, which creates a defect[113]. The Q-factor for these types of optical cavities is typically much lower than that of whispering gallery mode microresonators, but recently nanostructured photonic crystal resonators have hit a record Q-factor of 9×10^6[114]. The photonic crystal properties

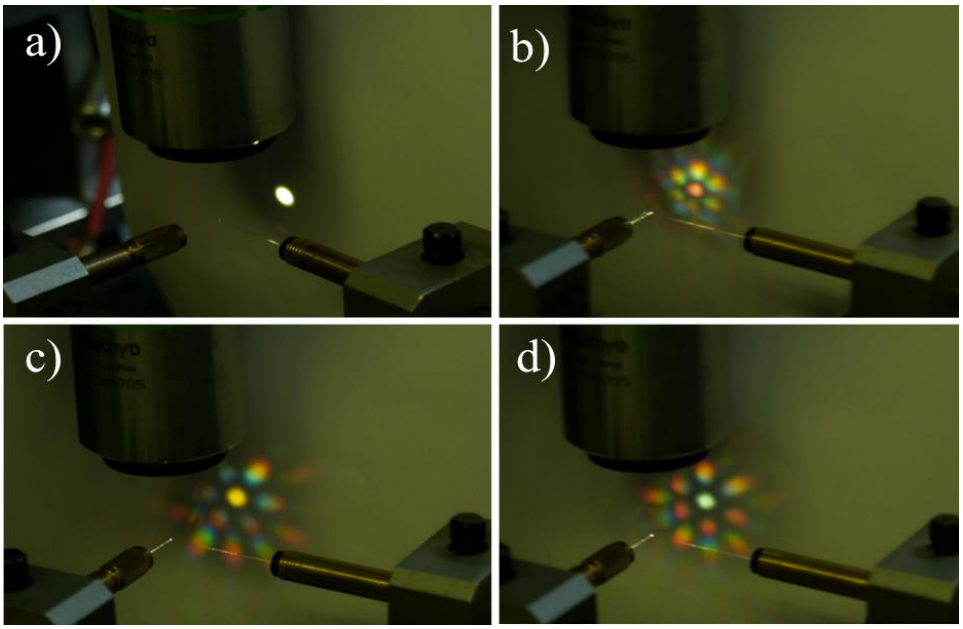

Figure 7.1: Diffraction by a diatom frustule. a) supercontinuum beam with no diatom in place b-d) diatom in different positions on the frustule showing wavelength dependent diffraction due to the differing color of the central m=0 diffraction order.

of a structure manifest themselves as diffraction, confinement, or absorption of light depending on the input frequency, polarization state, and angle to the structure[115,116].

Previous to this work, optical filtering by diatom frustules was studied experimentally by our group. In this experiment, supercontinuum light was passed through the face of a diatom frustule, similar to those explored in the previous chapter. The species used for these experiments was *Coscinodiscus wailesii.* Light diffracts due to the periodic structure of the pores on the diatom frustule causing the pattern shown in Figure 7.1. At different positions on the diatom frustule the spectral dependence of the diffraction efficiency changes. The wavelength passed through the central order depends on the pore spacing of the frustule. The light from the central order was collected with an optical fiber and the spectrum as measured with an optical spectrum analyzer.

7.2 Fourier optics beam propagation through a diatom

Fourier optics was the first method used for trying to understand the optical properties of diatom frustules. The beam propagation method is a straightforward method for simulating the propagation and diffraction of light through interfaces and objects to see the effects of aperture and index geometries. The goal of this simulation is to model the structure of a diatom as a thin phase mask and examine the far-field diffraction pattern as a result of phase and absorption. This simulation is executed in MATLAB.

The first step is to generate the initial field past the diatom. This is given by,

$$E_o(r) = A(x,y)e^{ik_0 n(x,y)d} \qquad (7.1)$$

where A is the beam aperture and $k_0 = 2\pi/\lambda$. The refractive index profile n describes the frustule geometry and can either be generated as a lattice or taken directly from the binary images generated in the previous chapter. The refractive index profile is a complex number that also accounts for optical loss due to the diatom geometry and material. This can be from absorption or scattering and lets only the coherent light interact with the model. The propagator used is

$$K(k) = e^{i\left(k - \frac{\left(k_x^2 + k_y^2\right)}{2k}\right)z} \qquad (7.2)$$

The propagator, K, is convolved with the initial field in Fourier space:

$$E(k) = FFT(E_o(r)) * K(k) \qquad (7.3)$$

The inverse Fourier transform is then calculated to determine the final field, *E*, after propagation for a distance of *z*[117].

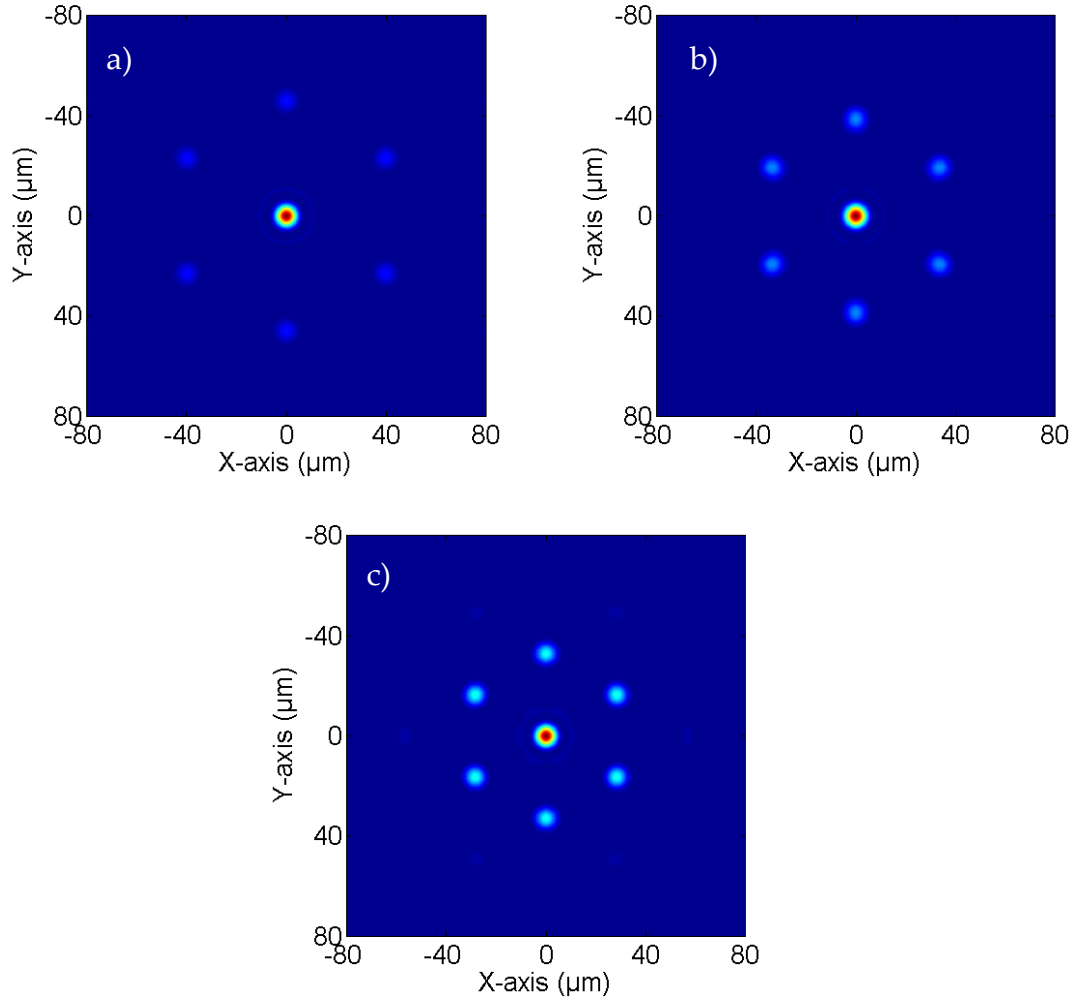

Figure 7.2: Far-field diffraction of simulated diatom structure with a mean pore spacing of a) 2.5 µm, b) 3.0 µm, and c) 3.5 µm.

This method for propagating electromagnetic waves was used to look at the structure of diatoms and the diffraction that occurs when light propagates through the frustule surface. The simulation setup generates a hexagonal lattice with random perturbations to simulate the diatom surface and define the complex electric field $E_o(r)$ beyond the diatom frustule. When light propagates through the hexagonal diatom frustule it creates a hexagonal diffraction pattern. A longer lattice spacing brings the diffraction pattern closer together. The diffraction patterns shown in Figure 7.2 represent the field at only one wavelength, 633nm. In the analogous experiment, the diatom was illuminated with a supercontinuum

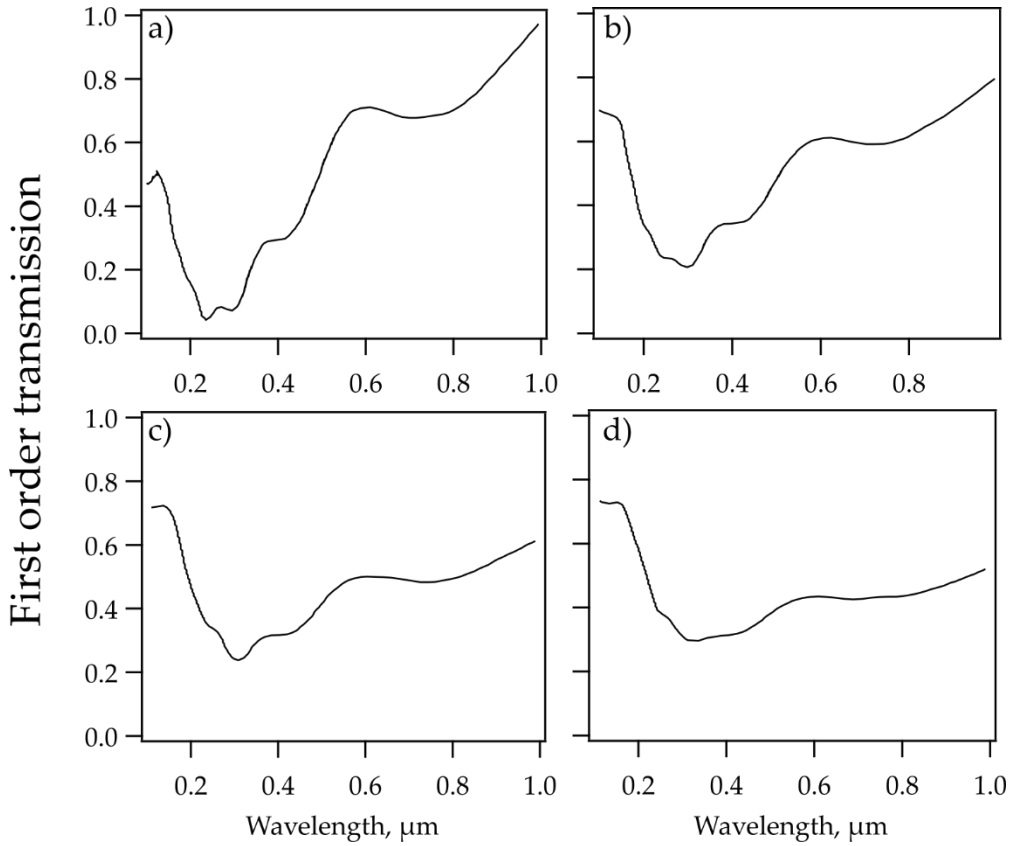

Figure 7.3: Simulated transmission of light through diatom frustules of different hole spacing. The light in the central diffraction order is normalized to the total transmission. The spacing ranges from 2.5 μm to 4.0 μm in 0.5 μm steps.

light source via optical fiber. The light collected beyond the diatom is collected by a single mode optical fiber which only samples the central region of the diffraction pattern. The light is analyzed by an optical spectrum analyzer to see the transmission spectrum.

To simulate this experiment, the propagation code is run at each wavelength from 100 nm to 1000 nm. A 10 μm aperture samples and integrates the field intensity, $|E|^2$, at the central order and normalizes this value to the intensity of the entire diffraction image to see an approximation of the wavelength dependent diffraction efficiency. The results are similar to what is being measured in the actual physical experiment. The simulated results are plotted in Figure 7.3 and show that as the pore spacing increases the minima of first order light

gradually shifts and the width of the dip widens. The reduced portion of the light in the first order corresponds to more light being diffracted by the diatom at that wavelength. When the spectrum broadens and flattens this signifies the lack of preferential diffraction at specific wavelengths.

7.3 Structure of high index converted diatoms

Diatom frustules are composed primarily of silica, which has been a primary motivation for investigating optical properties of the diatom. The index of silica is relatively low. Photonic crystal structures typically are made using materials with a high index contrast to define the features. The high index contrast allows for a more defined and complete band gap. A high index contrast can create a total band gap as opposed to a partial band gap; with these properties, full rejection of light in the stop band is expected.

If diatom frustules with a high refractive index are used in similar experiments to the original wavelength filtering experiments performed, it is expected that we would have different and more prominent wavelength filtering properties. To create diatom frustules with a high refractive index the original silica frustules can be converted into a high index material such as Mg_2Si.

This conversion process was performed by collaborators at Georgia Tech. The multi-step process converts a diatom of species *C. wailesii* in stages from the initial silica (SiO_2) to a porous silicon. The pores are filled with MgO creating an MgO:Si diatom frustule. The final step fully converts the diatom frustule to Mg_2Si. A single diatom frustule was tracked during each step of the conversion process. The frustule was imaged by SEM and elemental analysis was performed with EDX. The images of the diatom frustule were analyzed using the software

described in the previous chapter. This analysis shows that the diatom morphology and scale are well preserved during the chemical conversion process. Throughout the conversion process the mean pore spacing remains at 2.0 μm with deviation from this on the order of tens of nanometers. The images and pore distributions are shown in Figure 7.4. The converted diatoms are then used for optical filtering experiments as described above.

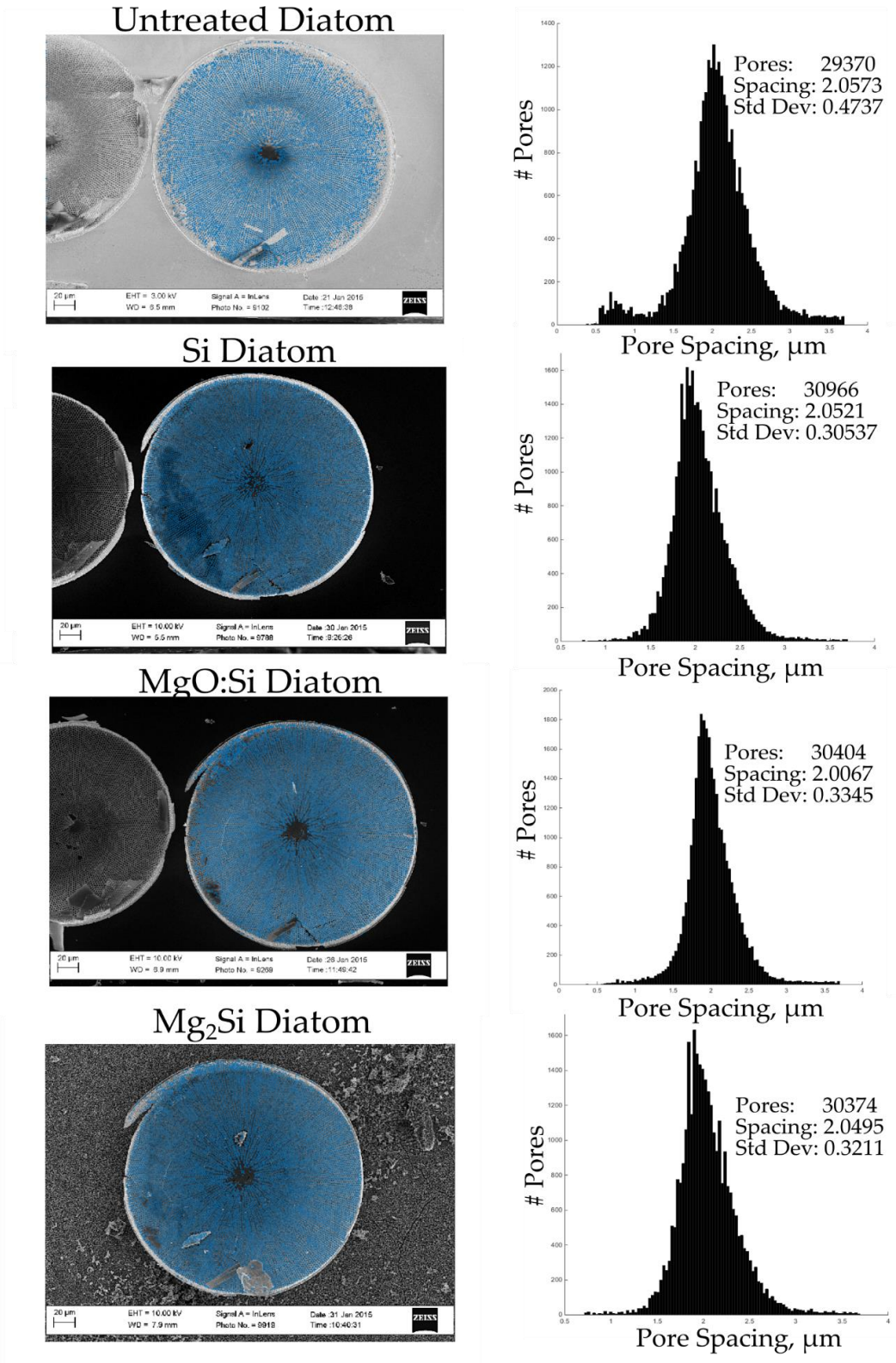

Figure 7.4: Pore spacing statistics and analyzed images of single diatom frustules during conversion process from silica to Mg_2Si.

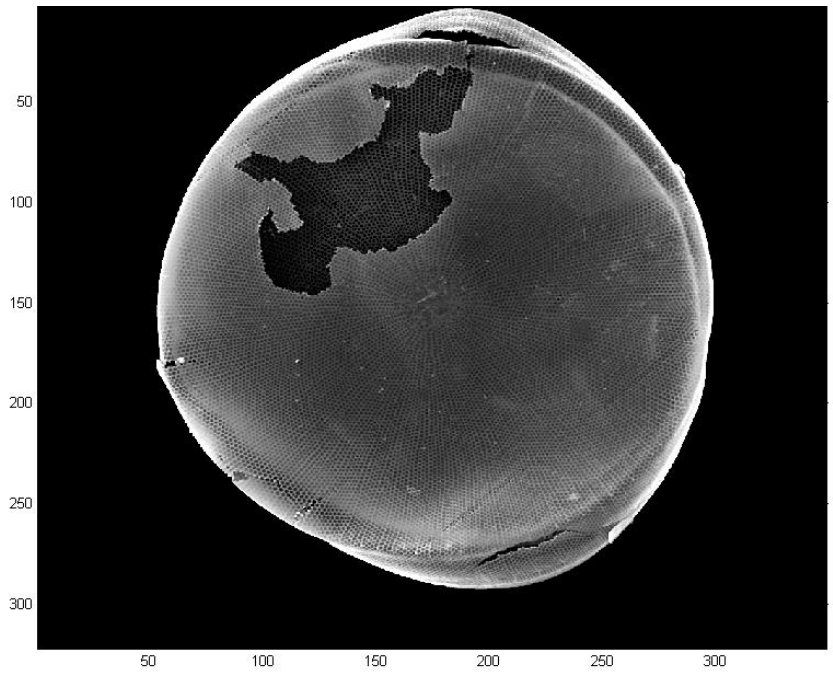

Figure 7.5: SEM of converted diatom used in wavelength filtering experiments

7.4 Visualizing diatom frustules for optics

It is now straightforward to generate a significant amount of data describing a particular diatom frustule's morphology. However, reducing the data to a useful form can be difficult and is subjective to the user and application. The immediate reduction is seen directly in the statistics of the pore spacing distribution. The mean and variance adequately describe the diatom, but lack the locality that may be expected in some fields of research. On the other end of the spectrum, each pore can be visualized as a point in a heat map as seen in Figure 7.6. This is a good qualitative display of the morphology and is useful for identifying structural patterns on the surface of the diatom.

Identifying each individual pore-to-pore connection may be excess information. One is likely interested in gaining some quantitative information to describe each region of the diatom frustule; this is especially true in optics. The

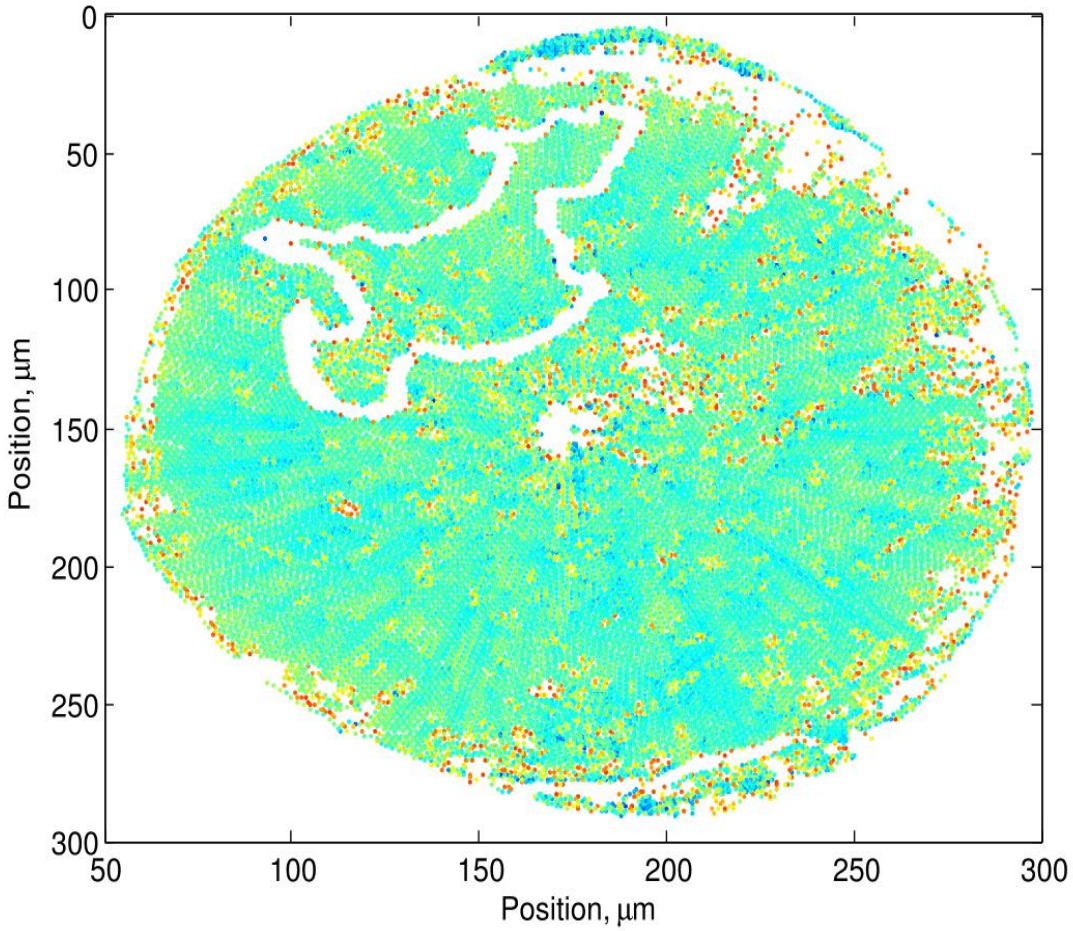

Figure 7.6: Heat map of converted diatom. Each pore-to-pore connection is represented by a colored dot. Red dots are longer and blue dots are shorter. The mean pore spacing is: 2.162µm; the standard deviation is: .706µm; and n=39372 edges

light which interacts with the diatom frustule typically has a spot size of less than 10 µm.

It is beneficial to partition the diatom into segments on this scale and display the statistics of each local region. The image of the diatom is partitioned into a rectangular spatial grid in which the mean pore spacing in each grid area is calculated and displayed as a pixelated heat map. Another, similar method for visualizing the same data is seen in Figure 7.8. In this figure the diatom is partitioned into a 15 µm grid and each grid square has the mean hole spacing in microns displayed with a color. When we threshold the local means with the

global mean we can see sections that have an overall smaller or larger than average pore spacing. This would indicate regions where the optical wavelength filtering would be different in an experiment as Section 7.1 describes.

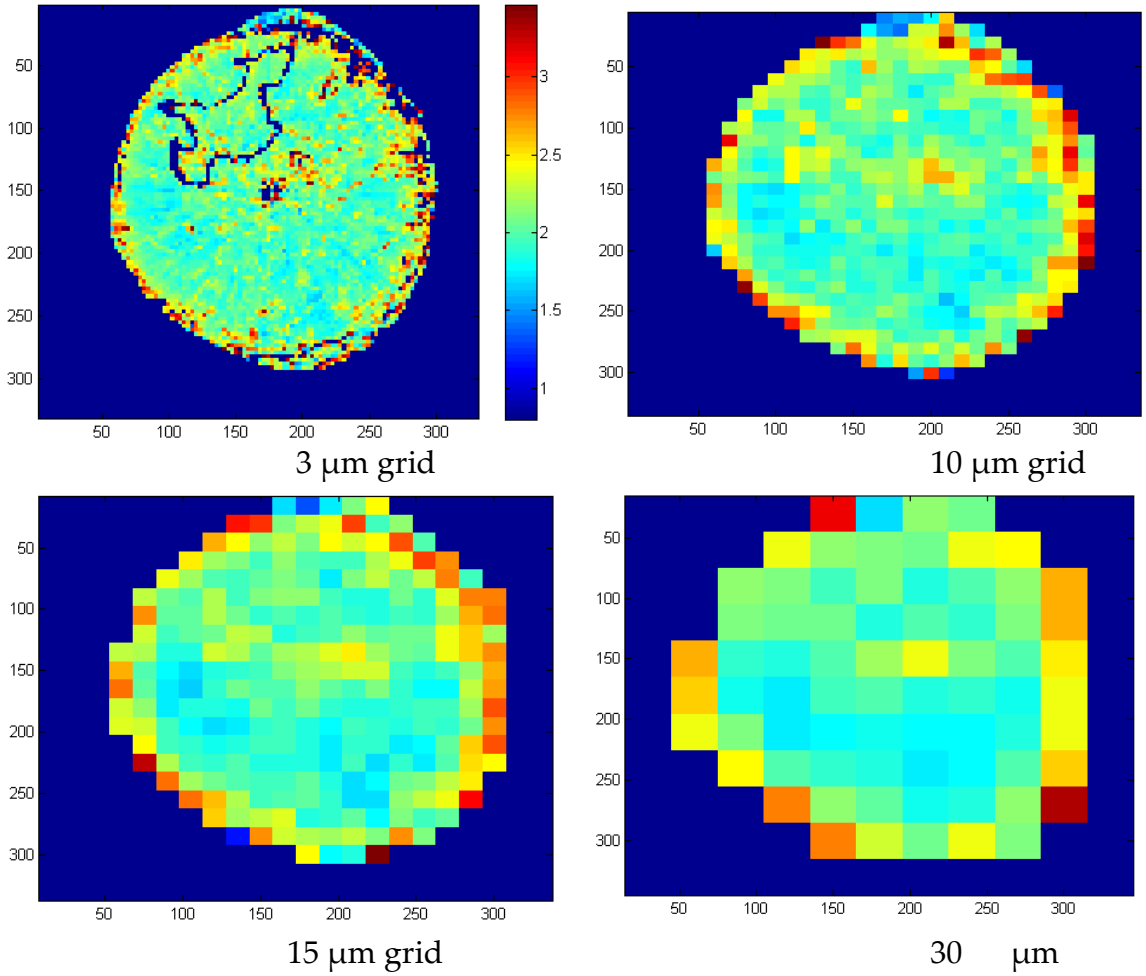

Figure 7.7: Partitioned diatoms shown with different grid partition sizes ranging from 3 μm to 30 μm. The heat map shows mean pore spacing for each partition in units of μm.

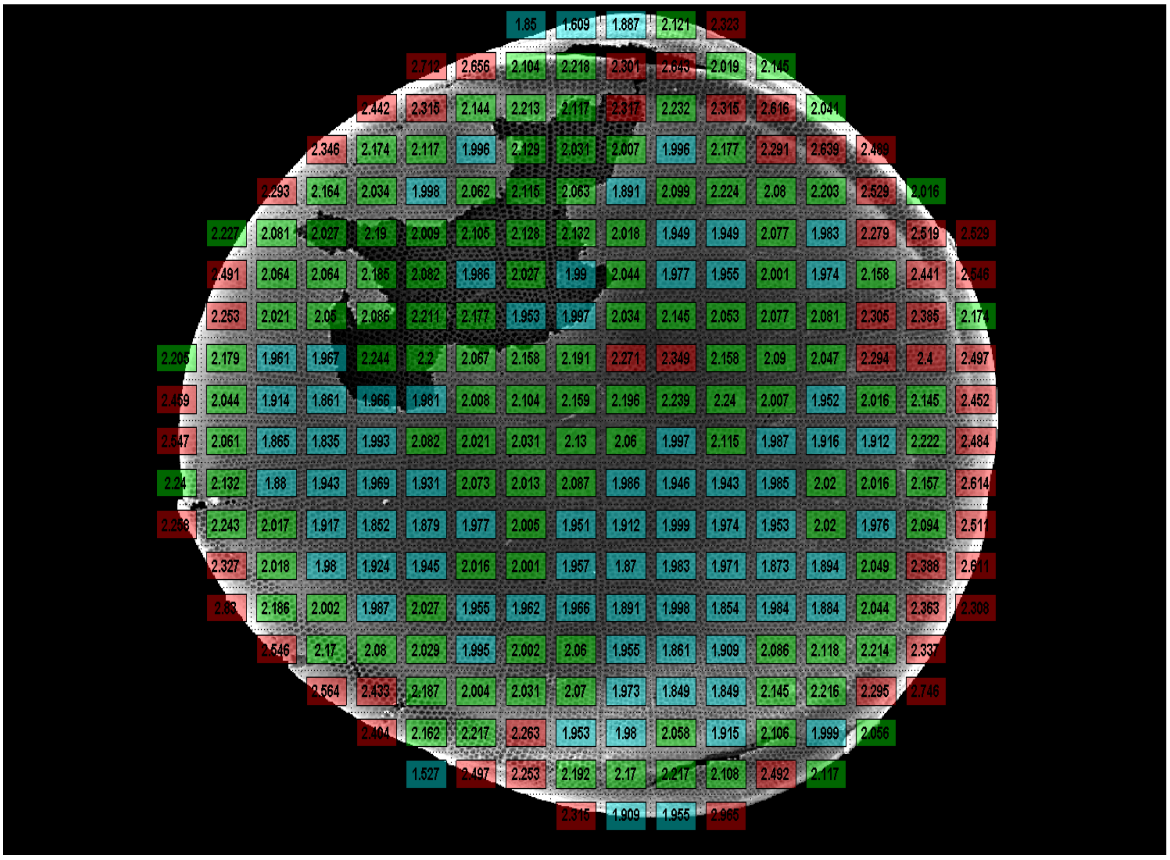

Figure 7.8: Same diatom with partitions labeled and color coded by mean pore spacing of the region. The median numbers are shown in green, while the red and blue indicate regions with mean pore spacing that is significantly higher or lower than the mean pore spacing respectively.

7.5 FDTD Simulation of *C. wailesii*

To confirm the phenomena found in the optical filtering experiments simulations are necessary to confirm the trends seen. These experiments are recreated using finite difference time domain (FDTD) simulation software (Lumerical). FDTD is a widely used computational method for solving Maxwell's equations. Maxwell's equations are solved over a simulation grid composed of Yee cells named after the mathematician who pioneered the FDTD method. Yee cells are spatially offset cells which contain information on the **E** and **H** field at each

location to aid in calculation in local differentials. The **E** and **H** fields are calculated and updated for each time step and the results of the fields through simulation time can be analyzed. Propagating ultrashort pulses of the **E** and **H** fields in time steps allows for frequency analysis over a spectrum of wavelengths without having to individually simulate each wavelength[118].

The implementation of the FDTD algorithm in Lumerical software allows for simulation geometries to be created through a computer aided drafting (CAD) interface or by generating the simulation through scripting the geometry. To analyze diatom structures using FDTD, an SEM image of the diatom is used to generate the geometry. The SEM segments used are seen in the pore location and radius information is determined using the same image processing and analysis techniques described in the previous chapter. The mean pore spacing distributions and statistics for each region of the diatom used are seen in Figure 7.11 and Figure 7.14.

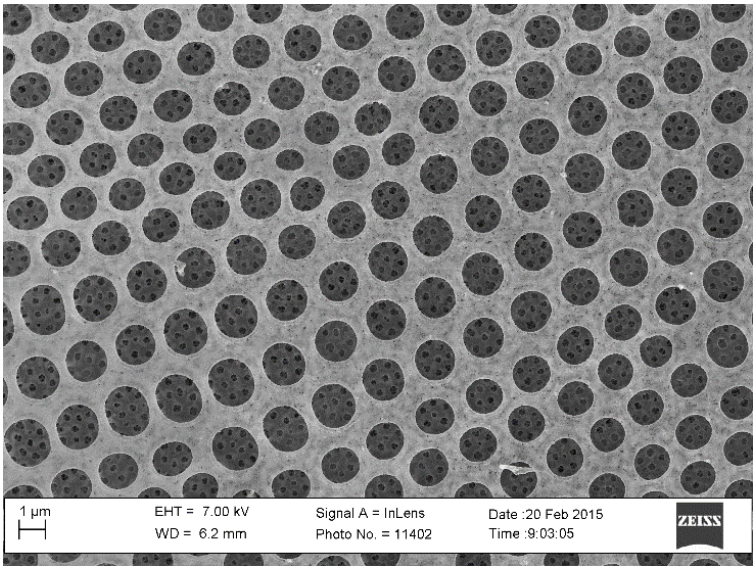

Figure 7.9: SEM image of section of converted diatom.

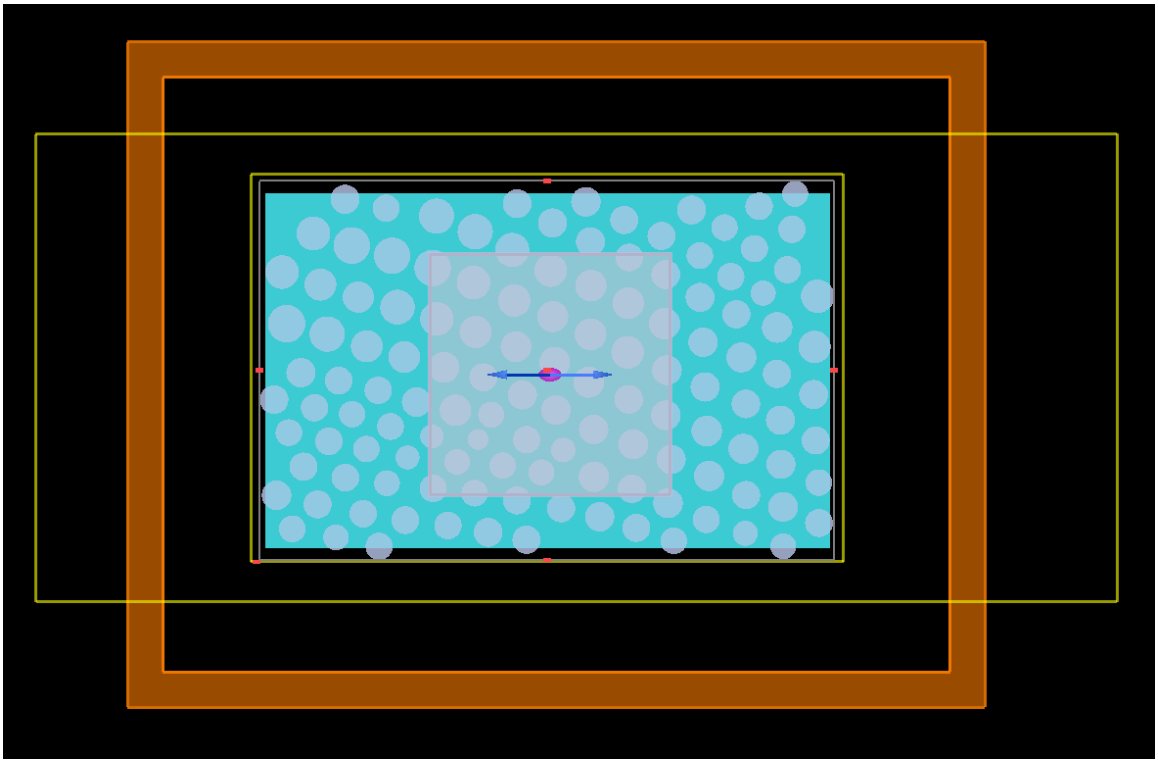

Figure 7.10: SEM simulation geometry for diatom section seen in Figure 7.9.

This data is imported into the Lumerical software and a script generates a circle of objects of a given radius at each location. The circles represent the etching of a rectangular material in each location which defines the pores (n = 1 in these locations). The refractive index (n) of the material can be defined as needed; in the simulations n is swept from 1.45 to 3.60 to represent the natural silica diatom and the refractive index of the converted Mg_2Si diatom as well as the region in between.

The input light source is a pulse with a spatially Gaussian profile. The beam radius if 5 μm. The pulse is short enough to span the wavelength bandwidth of 400 nm to 1400 nm which mimics the wavelengths used in the experimental setup. The thickness of the rectangular slab which represents the frustule surface is 200 nm, as determined by SEM measurements. The input light source passes perpendicular through the frustule surface and then the light is collected by a

detector behind the frustule; this is represented as a yellow rectangle in Figure 7.10 and Figure 7.13.

The simulation is set to run a parameter sweep of incident angle including 0^o, 13.3^o, and 26.6^o and a refractive index sweep of 1.45, 2.16, 2.83, and 3.60. The simulations run for 12 separate configurations for each diatom region.

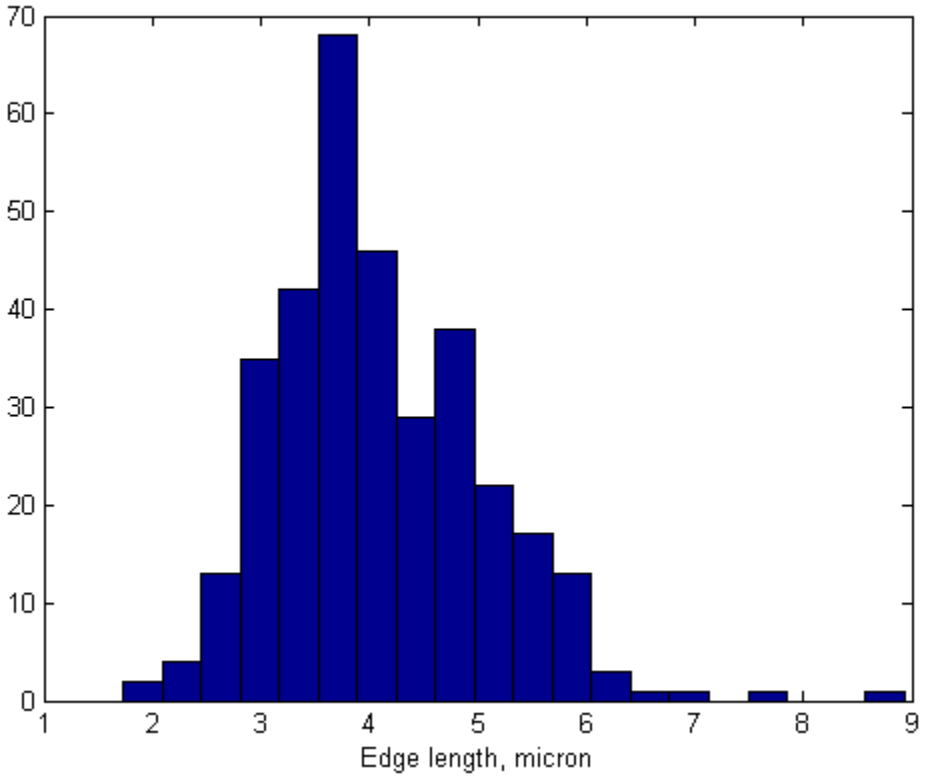

Figure 7.11: Distribution of pore-to-pore spacing in microns for diatom in Figure 7.9. The mean pore spacing is 4.0802 μm and variance .9606 μm. The number of edges used is 336.

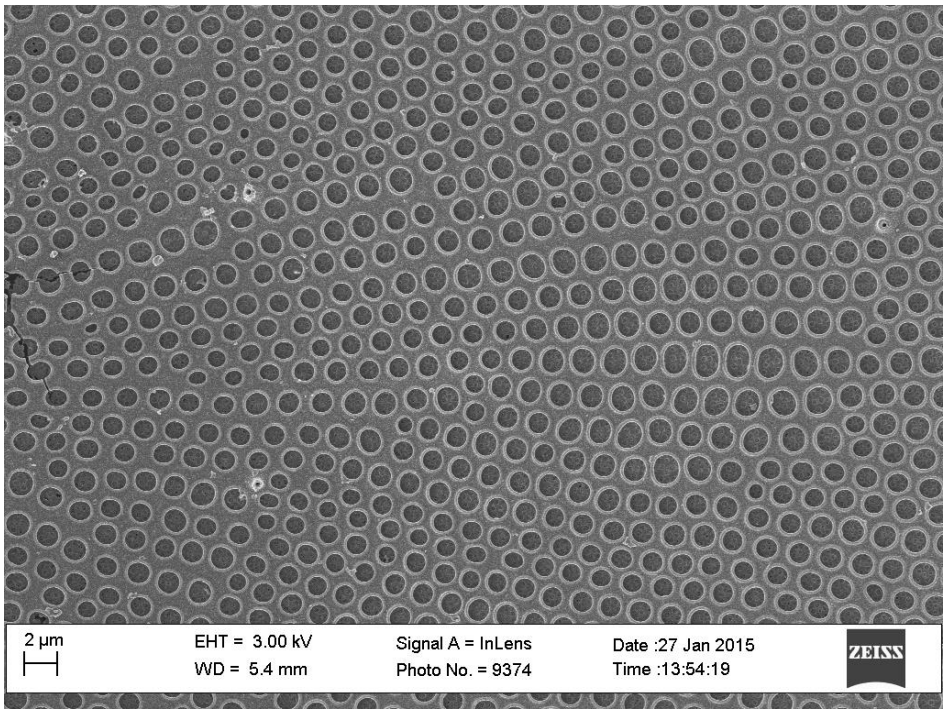

Figure 7.12: SEM image of second region of converted diatom used for FDTD simulation.

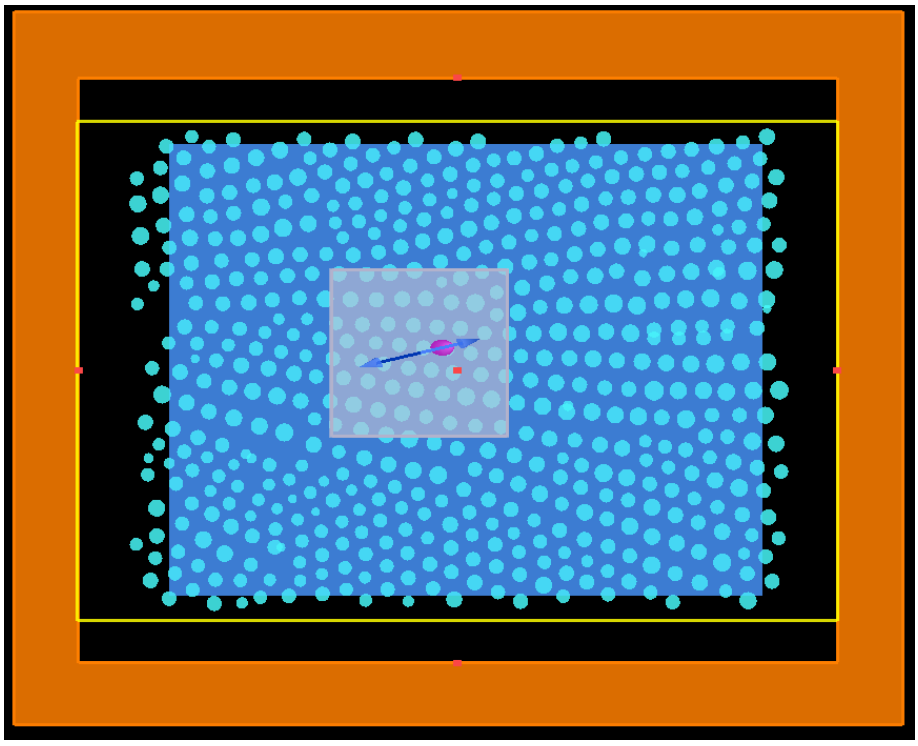

Figure 7.13: Simulation region generated for diatom in Figure 7.12.

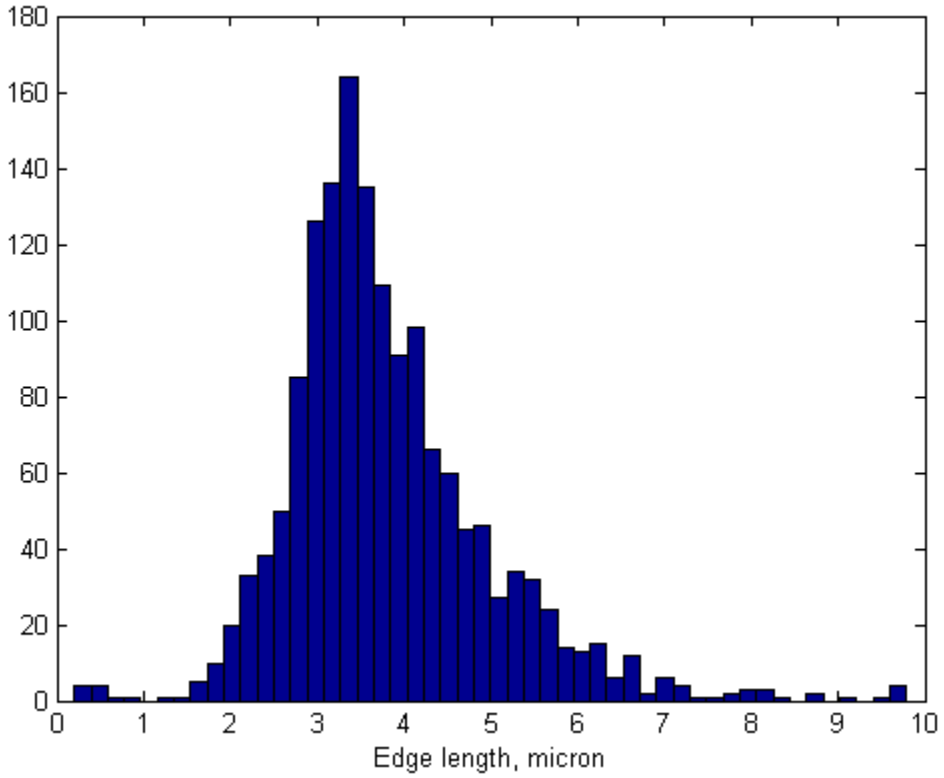

Figure 7.14: Distribution of pore-to-pore spacing in microns for diatom in Figure 7.12. The mean pore spacing is 3.8088 μm and standard deviation is 1.17 μm. The number of edges used is 1537.

The light propagates through the structured diatom frustule and some of the light is reflected or trapped and guided by the frustule. The light that is allowed to pass through the frustule surface is measured by a detector and the transmission of the initial light field is calculated. The results for each angle and refractive index simulated for the two diatom SEM images are shown in Figure 7.15 and Figure 7.16. Higher index materials cause a more pronounced stop band as expected. The FDTD simulation results show a shift in pass-band wavelength as a function of angle. These results qualitatively match the results of the corresponding physical experiment.

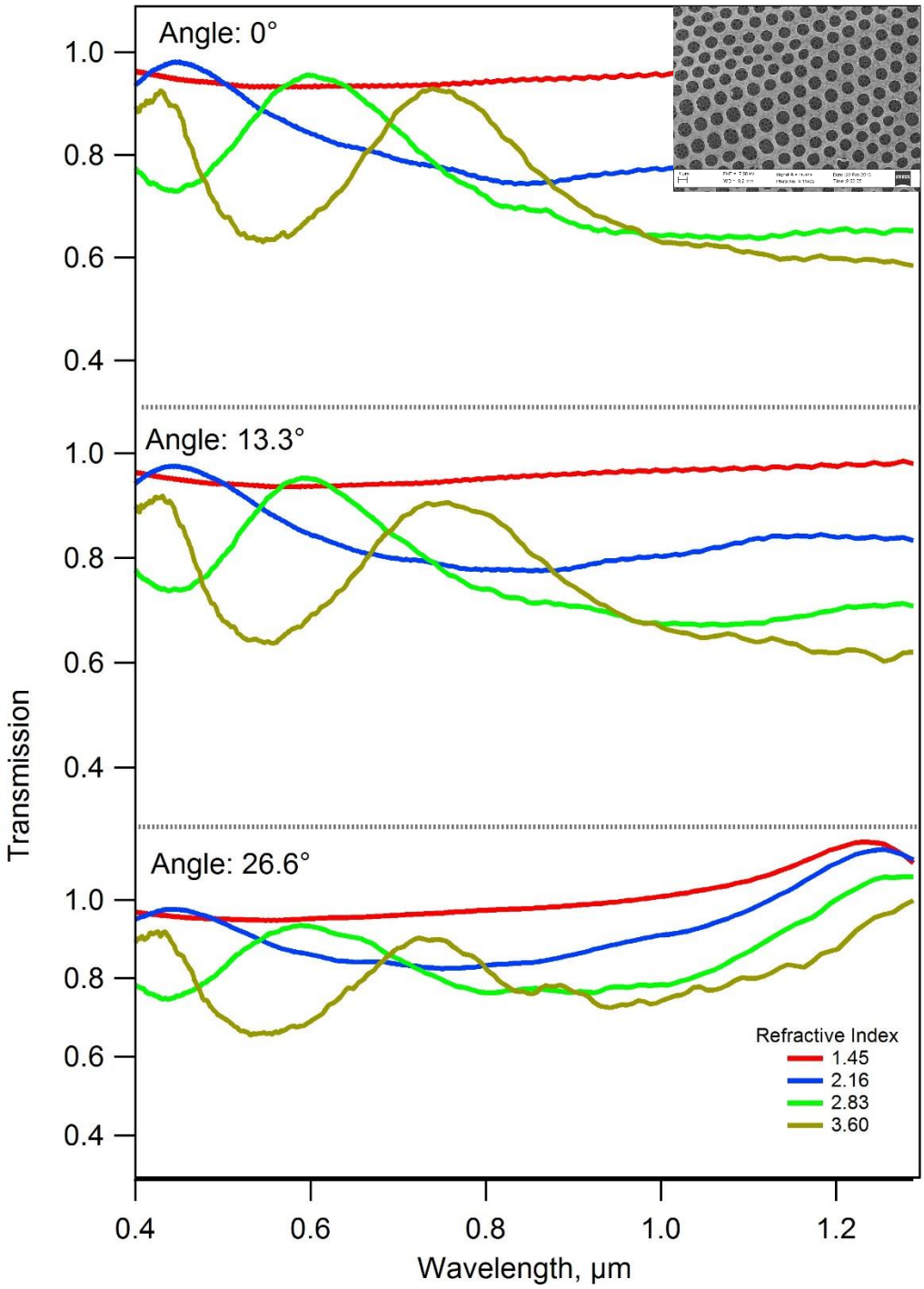

Figure 7.15: Transmission of light calculated by FDTD simulation of the diatom region shown in Figure 7.9.

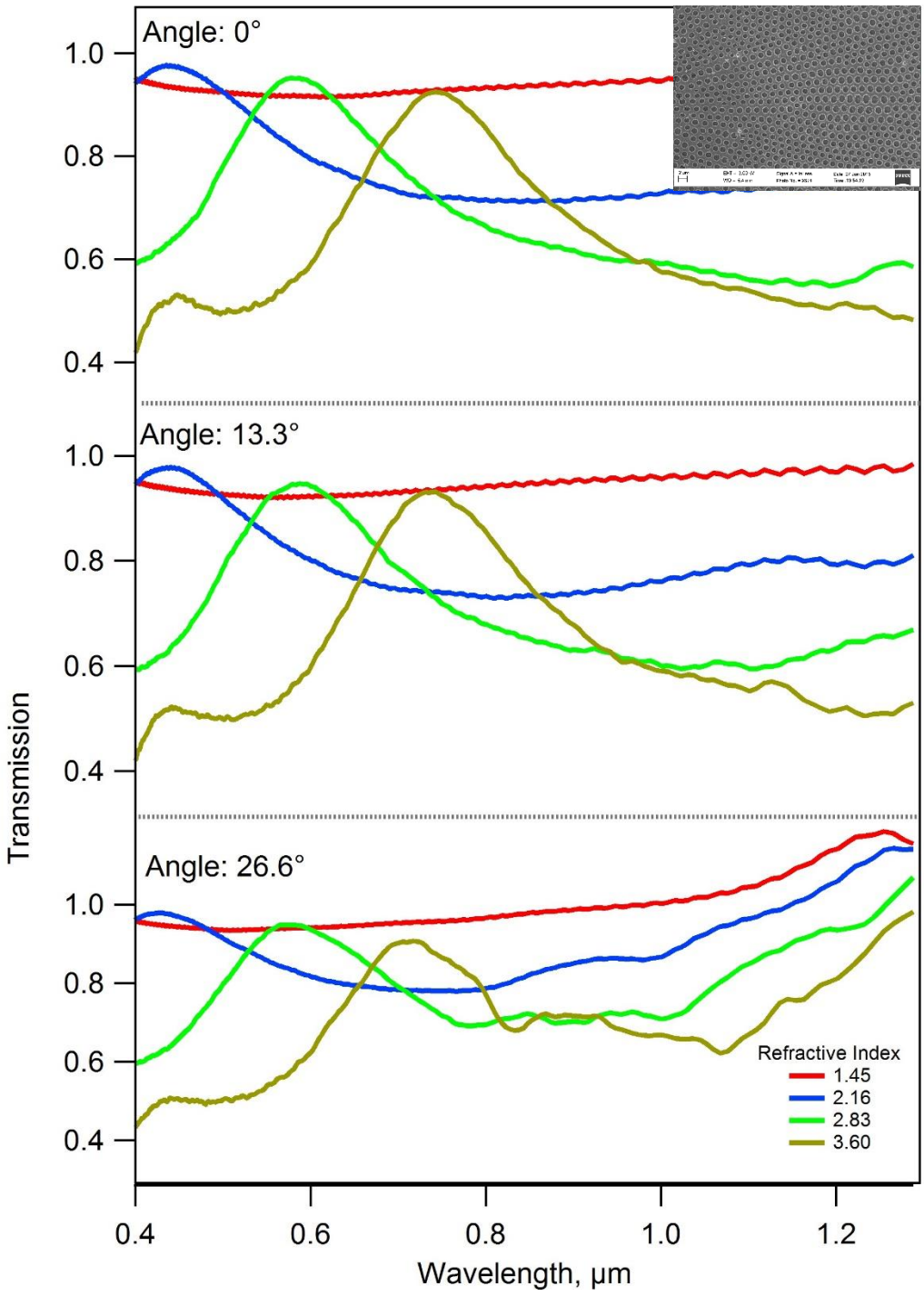

Figure 7.16: Transmission of light calculated by FDTD simulation of the diatom region shown in Figure 7.12.

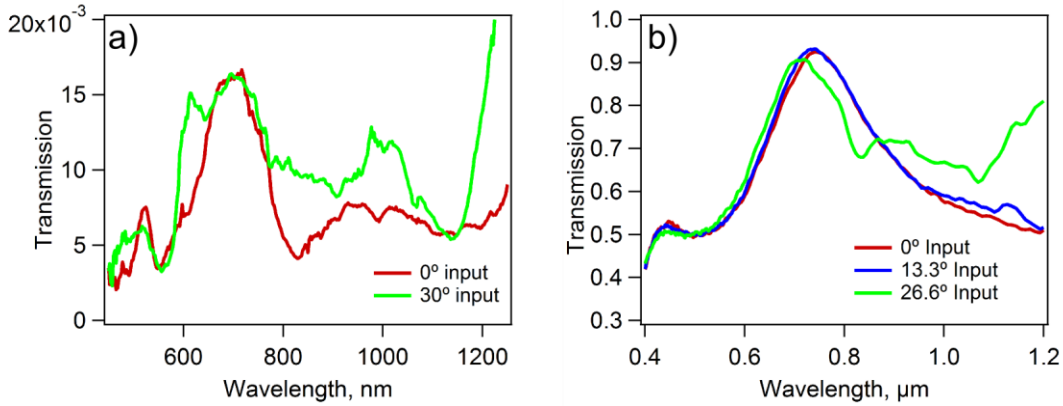

Figure 7.17: a) Experimental plot of transmission through converted diatom frustule at an input angle of 0° and 30°. b) Simulated data from Figure 7.16 of one refractive index (3.60) at various input angles.

The simulated data qualitatively matches the experimental data. There is a slight blue shift of peak edges in both the experimental and simulated data. Another peak also begins to appear at higher angles. This data is shown side by side in Figure 7.17 and a zoomed in version of the simulated data can be found in Figure 7.18. Although this effect is very minor it helps to verify the FDTD simulations.

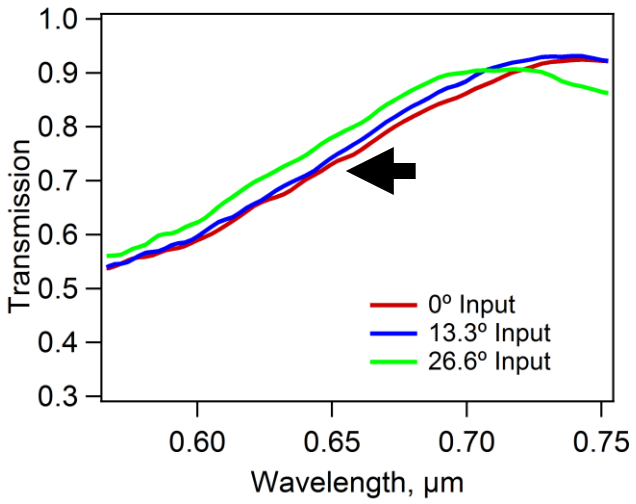

Figure 7.18: Zoomed in plot of simulated diatom propagation at various input angles shows the slight blue shift of the peak edges as incident angle increases.

Bibliography

1. Farnesi, D., Barucci, a., Righini, G. C., Berneschi, S., Soria, S. & Nunzi Conti, G. 2014 Optical Frequency Conversion in Silica-Whispering-Gallery-Mode Microspherical Resonators. *Phys. Rev. Lett.* **112**, 093901. (doi:10.1103/PhysRevLett.112.093901)

2. Schließer, A. 2009 Cavity optomechanics and optical frequency comb generation with silica whispering-gallery-mode microresonators. *Thesis LMU München*

3. Spillane, S., Kippenberg, T. & Vahala, K. 2002 Ultralow-threshold Raman laser using a spherical dielectric microcavity. *Nature* **415**, 621–623.

4. Grudinin, I. S., Matsko, A. B., Savchenkov, A. a., Strekalov, D., Ilchenko, V. S. & Maleki, L. 2006 Ultra high Q crystalline microcavities. *Opt. Commun.* **265**, 33–38. (doi:10.1016/j.optcom.2006.03.028)

5. Chormaic, S., Wu, Y. & Ward, J. 2012 Whispering gallery mode resonators as tools for non-linear optics and optomechanics. *Spie Lase* **8236**, 1–8. (doi:10.1117/12.906665)

6. Saleh, B. E. A. & Teich, M. C. 1997 Fundamentals of Photonics , 2nd Edition. *Wiley-Interscience*

7. Dantham, V. R. & Bisht, P. B. 2009 High-Q whispering gallery modes of doped and coated single microspheres and their effect on radiative rate. *J. Opt. Soc. Am. B* **26**, 290. (doi:10.1364/JOSAB.26.000290)

8. Ausman, L. K. & Schatz, G. C. 2008 Whispering-gallery mode resonators: Surface enhanced Raman scattering without plasmons. *J. Chem. Phys.* **129**, 054704. (doi:10.1063/1.2961012)

9. Vollmer, F. & Arnold, S. 2008 Whispering-gallery-mode biosensing: label-free detection down to single molecules. *Nat. Methods* **5**, 591–596. (doi:10.1038/NMETH.1221)

10. Chen, Y., Lei, L., Zhang, K., Shi, J., Wang, L., Li, H., Zhang, X. M., Wang, Y. & Chan, H. L. W. 2010 Optofluidic microcavities: Dye-lasers and biosensors. *Biomicrofluidics* **4**, 043002. (doi:10.1063/1.3499949)

11. Noto, M., Khoshsima, M., Keng, D., Teraoka, I., Kolchenko, V. & Arnold, S. 2005 Molecular weight dependence of a whispering gallery mode biosensor. *Appl. Phys. Lett.* **87**, 223901. (doi:10.1063/1.2137902)

12. Bahl, G., Kim, K. H., Lee, W., Liu, J., Fan, X. & Carmon, T. 2013 Brillouin cavity optomechanics with microfluidic devices. *Nat. Commun.* **4**, 1994. (doi:10.1038/ncomms2994)

13. Hyun Kim, K., Bahl, G., Lee, W., Liu, J., Tomes, M., Fan, X. & Carmon, T. 2013 Cavity optomechanics on a microfluidic resonator with water and viscous liquids. *Light Sci. Appl.* **2**, e110. (doi:10.1038/lsa.2013.66)

14. Righini, G. C., Dumeige, Y., Féron, P., Ferrari, M., Conti, G. N., Ristic, D. & Soria, S. 2011 Whispering Gallery Mode microresonators: Fundamentals and applications. *Riv. del Nuovo Cim.* **34**, 435–488. (doi:10.1393/ncr/i2011-10067-2)

15. Matsko, a. B. & Ilchenko, V. S. 2006 Optical resonators with whispering-gallery modes-part I: basics. *IEEE J. Sel. Top. Quantum Electron.* **12**, 3–14. (doi:10.1109/JSTQE.2005.862952)

16. Matsko, A. B., Savchenkov, A. A., Strekalov, D., Ilchenko, V. S. & Maleki, L. 2005 Review of Applications of Whispering-Gallery Mode Resonators in Photonics and Nonlinear Optics. *Prism* **42**, 1–51. (doi:citeulike-article-id:10634121)

17. Braginsky, V., Gorodetsky, M. & Ilchenko, V. 1989 Quality-factor and nonlinear properties of optical whispering-gallery modes. *Phys. Lett. A* **137**, 393–397.

18. Spillane, S. M., Kippenberg, T. J., Painter, O. J. & Vahala, K. J. 2003 Ideality in a fiber-taper-coupled microresonator system for application to cavity quantum electrodynamics. *Phys. Rev. Lett.* **91**, 043902. (doi:10.1103/PhysRevLett.91.043902)

19. Knight, J. C., Cheung, G., Jacques, F. & Birks, T. A. 1997 Phase-matched

excitation of whispering-gallery-mode resonances by a fiber taper. *Opt. Lett.* **22**, 1129–31.

20. Gorodetsky, M. L., Savchenkov, a a & Ilchenko, V. S. 1996 Ultimate Q of optical microsphere resonators. *Opt. Lett.* **21**, 453–5.

21. Armani, D., Kippenberg, T., Spillane, S. & Vahala, K. 2003 Ultra-high-Q toroid microcavity on a chip. *Nature* **421**, 925–928. (doi:10.1038/nature01432.1.)

22. Fürst, J. U., Strekalov, D. V., Elser, D., Lassen, M., Andersen, U. L., Marquardt, C. & Leuchs, G. 2010 Naturally phase-matched second-harmonic generation in a whispering-gallery-mode resonator. *Phys. Rev. Lett.* **104**, 1–4. (doi:10.1103/PhysRevLett.104.153901)

23. Savchenkov, A. A., Matsko, A. B., Liang, W., Ilchenko, V. S., Seidel, D. & Maleki, L. 2011 Kerr combs with selectable central frequency. **5**, 293–296. (doi:10.1038/NPHOTON.2011.50)

24. Ilchenko, V. S., Savchenkov, A. a, Matsko, A. B. & Maleki, L. 2004 Nonlinear optics and crystalline whispering gallery mode cavities. *Phys. Rev. Lett.* **92**, 043903. (doi:10.1103/PhysRevLett.92.043903)

25. Lin, H. B., Huston, a L., Justus, B. L. & Campillo, a J. 1986 Some characteristics of a droplet whispering-gallery-mode laser. *Opt. Lett.* **11**, 614–616. (doi:10.1364/OL.11.000614)

26. Zhang, J.-Z. & Chang, R. K. 1989 Droplets, Generation and suppression of stimulated Brillouin scattering in single liquid. *J. Opt. Soc. Am. B* **6**, 151–153.

27. Humphrey, M. J., Dale, E., Rosenberger, a. T. & Bandy, D. K. 2007 Calculation of optimal fiber radius and whispering-gallery mode spectra for a fiber-coupled microsphere. *Opt. Commun.* **271**, 124–131. (doi:10.1016/j.optcom.2006.10.018)

28. Love, J. & Henry, W. 1991 Tapered single-mode fibres and devices. I. Adiabaticity criteria. *… , IEE Proc. J*

29. Cohoon, G. a., Kieu, K. & Norwood, R. a. 2014 Multiphoton excitation of organic chromophores in microbubble resonators. *SPIE Photonics West 2014-*

LASE Lasers Sources **8960**, 89600L. (doi:10.1117/12.2038053)

30. Kieu, K. Q. & Mansuripur, M. 2006 Biconical fiber taper sensors. *IEEE Photonics Technol. Lett.* **18**, 2239–2241. (doi:10.1109/LPT.2006.884742)

31. Birks, T. A. & Li, Y. W. 1992 The Shape of Fiber Tapers. *J. Light. Technol.* **10**, 432–438.

32. Lützler, C. 2012 Fabrication of Optical Microfibers.

33. Black, R. & Lacroix, S. 1991 Tapered single-mode fibres and devices. II. Experimental and theoretical quantification. *… , IEE Proc. J* **138**, 355–364.

34. Henze, R., Seifert, T., Ward, J. & Benson, O. 2011 Tuning whispering gallery modes using internal aerostatic pressure. *Opt. Lett.* **36**, 4536. (doi:10.1364/OL.36.004536)

35. Vetsch, E., Reitz, D., Sagué, G., Schmidt, R., Dawkins, S. T. & Rauschenbeutel, a. 2010 Optical interface created by laser-cooled atoms trapped in the evanescent field surrounding an optical nanofiber. *Phys. Rev. Lett.* **104**, 1–4. (doi:10.1103/PhysRevLett.104.203603)

36. Vetsch, E., Dawkins, S. T., Mitsch, R., Reitz, D., Schneeweiss, P. & Rauschenbeutel, A. 2012 Nanofiber-Based Optical Trapping of Cold Neutral Atoms. *IEEE J. Sel. Top. Quantum Electron.* **18**, 1763–1770. (doi:10.1109/JSTQE.2012.2196025)

37. Yalla, R., Nayak, K. P. & Hakuta, K. 2012 Fluorescence photon measurements from single quantum dots on an optical nanofiber. *Opt. Express* **20**, 2932. (doi:10.1364/OE.20.002932)

38. Ward, J. M., Maimaiti, A., Le, V. H. & Chormaic, S. N. 2014 Contributed Review: Optical micro- and nanofiber pulling rig. *Rev. Sci. Instrum.* **85**, 111501. (doi:10.1063/1.4901098)

39. OpenSCAD. Available from: www.openscad.org

40. RepRap. Available from: www.reprap.org

41. Slic3r. Available from: http://slic3r.org/

42. Oberg, E., Jones, F. D., Horton, H. L., Ryffel, H. H., Green, R. E. & McCauleym, C. J. 1996 *Machinery's Handbook*. 25th edn. New York, USA: Industrial Press, Inc.

43. Zhang, C., Anzalone, N. C., Faria, R. P. & Pearce, J. M. 2013 Open-source 3D-printable optics equipment. *PLoS One* **8**, e59840. (doi:10.1371/journal.pone.0059840)

44. Rowland, D. R. & Love, J. D. 1993 Evanescent-wave coupling of whispering-gallery modes of a dielectric cylinder. *Iee Proceedings-J Optoelectron.* **140**, 177–188. (doi:10.1049/ip-j.1993.0028)

45. Chembo, Y. K., Baumgartel, L. & Yu, N. 2012 Exploring the frequency stability limits of whispering gallery mode resonators for metrological applications. *Laser Reson. Microresonators, Beam Control Xiv* **8236**, 2–7. (doi:82360q 10.1117/12.908990)

46. Carmon, T., Yang, L. & Vahala, K. 2004 Dynamical thermal behavior and thermal self-stability of microcavities. *Opt. Express* **12**, 4742–50.

47. Vollmer, F. & Arnold, S. 2008 Whispering-gallery-mode biosensing : label-free detection down to single molecules. *Nat. Methods* **5**, 591–596. (doi:10.1038/NMETH.1221)

48. Del'Haye, P., Schliesser, a, Arcizet, O., Wilken, T., Holzwarth, R. & Kippenberg, T. J. 2007 Optical frequency comb generation from a monolithic microresonator. *Nature* **450**, 1214–7. (doi:10.1038/nature06401)

49. Sumetsky, M., DiGiovanni, D. J., Dulashko, Y., Fini, J. M., Liu, X., Monberg, E. M. & Taunay, T. F. 2011 Surface nanoscale axial photonics: robust fabrication of high-quality-factor microresonators. *Opt. Lett.* **36**, 4824–6.

50. Lin, J., Yu, S., Ma, Y., Fang, W., He, F. & Qiao, L. 2012 On-chip three-dimensional high-Q microcavities fabricated by femtosecond laser direct writing. *Opt. Lett.* **20**, 5676–5681.

51. Gattass, R. R. & Mazur, E. 2008 Femtosecond laser micromachining in transparent materials. *Nat. Photonics* **2**, 219–225. (doi:10.1038/nphoton.2008.47)

52. Ashcom, J. B., Gattass, R. R., Schaffer, C. B. & Mazur, E. 2006 Numerical aperture dependence of damage and supercontinuum generation from femtosecond laser pulses in bulk fused silica. *J. Opt. Soc. Am. B* **23**, 2317. (doi:10.1364/JOSAB.23.002317)

53. Schaffer, C. B., Brodeur, A., García, J. F. & Mazur, E. 2001 Micromachining bulk glass by use of femtosecond laser pulses with nanojoule energy. *Opt. Lett.* **26**, 93–5.

54. Tada, K., Cohoon, G. A., Kieu, K., Mansuripur, M. & Norwood, R. A. 2013 Fabrication of High-Q Microresonators by Femtosecond Laser Micromachining of Optical Fiber. *Photonics Technol. Lett.* **25**, 430.

55. Senthil Murugan, G., Wilkinson, J. S. & Zervas, M. N. 2012 Optical microdiscus resonators by flattening microspheres. *Appl. Phys. Lett.* **101**, 071106. (doi:10.1063/1.4746256)

56. Sumetsky, M., Dulashko, Y. & Windeler, R. S. 2010 Optical microbubble resonator. *Opt. Lett.* **35**, 898–900.

57. Senthil Murugan, G., Petrovich, M. N., Jung, Y., Wilkinson, J. S. & Zervas, M. N. 2011 Hollow-bottle optical microresonators. *Opt. Express* **19**, 20773–84.

58. White, I. M., Zhu, H., Suter, J. D., Fan, X. & Zourob, M. 2009 Label-free detection with the liquid core optical ring resonator sensing platform. *Methods Mol. Biol.* **503**, 139–165. (doi:10.1007/978-1-60327-567-5)

59. Lee, W., Sun, Y., Li, H., Reddy, K., Sumetsky, M. & Fan, X. 2011 A quasi-droplet optofluidic ring resonator laser using a micro-bubble. *Appl. Phys. Lett.* **99**, 091102. (doi:10.1063/1.3629814)

60. Berneschi, S., Farnesi, D., Cosi, F., Conti, G. N., Pelli, S., Righini, G. C. & Soria, S. 2011 High Q silica microbubble resonators fabricated by arc discharge. *Opt. Lett.* **36**, 3521–3.

61. Sumetsky, M., Dulashko, Y. & Windeler, R. S. 2010 Super free spectral range tunable optical microbubble resonator. *Opt. Lett.* **35**, 1866–8.

62. Watkins, A., Ward, J., Wu, Y. & Chormaic, S. N. 2011 Single-input spherical

microbubble resonator. *Opt. Lett.* **36**, 2113–5.

63. Shopova, S. I., Zhou, H., Fan, X. & Zhang, P. 2007 Optofluidic ring resonator based dye laser. *Appl. Phys. Lett.* **90**, 221101. (doi:10.1063/1.2743884)

64. Bansal, N. P. & Doremus, R. H. 1986 *Handbook of Glass Properties*. San Diego: Academic Press.

65. Budynas, R. & Nisbett, K. 2009 *Shigley's Mechanical Engineering Design, SI Version*.

66. Kaiser, W. & Garrett, C. 1961 Two-Photon Excitation in CaF_{2}: Eu^{2+}. *Phys. Rev. Lett.* **7**, 229–231. (doi:10.1103/PhysRevLett.7.229)

67. Makarov, N. S., Drobizhev, M. & Rebane, A. 2008 Two-photon absorption standards in the 550-1600 nm excitation wavelength range. *Opt. Express* **16**, 4029–47.

68. Xu, C. & Webb, W. W. 1996 Measurement of two-photon excitation cross sections of molecular fluorophores with data from 690 to 1050 nm. *J. Opt. Soc. Am. B* **13**, 481. (doi:10.1364/JOSAB.13.000481)

69. Kaneda, Y. & Kubota, S. 1997 Theoretical treatment, simulation, and experiments of doubly resonant sum-frequency mixing in an external resonator. *Appl. Opt.* **36**, 7766–75.

70. Paul, J., Kaneda, Y., Wang, T.-L., Lytle, C., Moloney, J. V & Jones, R. J. 2011 Doppler-free spectroscopy of mercury at 253.7 nm using a high-power, frequency-quadrupled, optically pumped external-cavity semiconductor laser. *Opt. Lett.* **36**, 61–63. (doi:10.1364/OL.36.000061)

71. Polzik, E. S. & Kimble, H. J. 1991 Frequency doubling with KNbO_3 in an external cavity. *Opt. Lett.* **16**, 1400. (doi:10.1364/OL.16.001400)

72. Boyd, G. D. & Kleinman, D. A. 1968 Parametric Interaction of Focused Gaussian Light Beams. *J. Appl. Phys.* **39**, 3597. (doi:10.1063/1.1656831)

73. Kenny, R., Birks, T. & Oakley, K. 1991 Control of optical fibre taper shape. *Electron. Lett.* , 1–3.

74. Kozlovsky, W. J., Nabors, C. D. & Byer, R. L. 1988 Efficient second harmonic generation of a diode-laser-pumped CW Nd:YAG laser using monolithic MgO:LiNbO/sub 3/ external resonant cavities. *IEEE J. Quantum Electron.* **24**, 913–919. (doi:10.1109/3.211)

75. Sperber, P. & Penzkofer, A. 1986 S0-Sn two-photon absorption dynamics of rhodamine dyes. *Opt. Quantum Electron.* **18**, 381–401. (doi:10.1007/BF02032565)

76. Kwok, A., Gillespie, J. & Serpengüzel, A. 1992 Two-photon-pumped lasing in microdroplets. *Opt. Lett.* **17**, 1435–1437.

77. Round, F. E., Crawford, R. M. & Mann, D. G. 1990 *The Diatoms: Biology & Morphology of the Genera*. Cambridge University Press.

78. Hamm, C. E., Merkel, R., Springer, O., Jurkojc, P., Maier, C., Prechtel, K. & Smetacek, V. 2003 Architecture and material properties of diatom shells provide effective mechanical protection. *Nature* **421**, 841–843. (doi:10.1038/nature01416)

79. Wilken, S., Hoffmann, B., Hersch, N., Kirchgessner, N., Dieluweit, S., Rubner, W., Hoffmann, L. J., Merkel, R. & Peeken, I. 2011 Diatom frustules show increased mechanical strength and altered valve morphology under iron limitation. *Limnol. Oceanogr.* **56**, 1399–1410. (doi:10.4319/lo.2011.56.4.1399)

80. Losic, D., Rosengarten, G., Mitchell, J. G. & Voelcker, N. H. 2006 Pore architecture of diatom frustules: potential nanostructured membranes for molecular and particle separations. *J. Nanosci. Nanotechnol.* **6**, 982–989. (doi:10.1166/jnn.2006.174)

81. Kopanska, K. S., Tesson, B., Lin, H., Meredith, J. C., Hildebrand, M. & Davis, A. 2014 Morphological Factors Involved in Adhesion of Acid-Cleaned Diatom Silica. *Silicon* , 1–13. (doi:10.1007/s12633-014-9178-2)

82. Kieu, K., Li, C., Fang, Y., Cohoon, G., Herrera, O. D., Hildebrand, M., Sandhage, K. H. & Norwood, R. A. 2014 Structure-based optical filtering by the silica microshell of the centric marine diatom Coscinodiscus wailesii. *Opt. Express* **22**, 15992–9.

83. Yamanaka, S., Yano, R., Usami, H., Hayashida, N., Ohguchi, M., Takeda, H. & Yoshino, K. 2008 Optical properties of diatom silica frustule with special reference to blue light. *J. Appl. Phys.* **103**. (doi:10.1063/1.2903342)

84. Noyes, J., Sumper, M. & Vukusic, P. 2011 Light manipulation in a marine diatom. *J. Mater. Res.* **23**, 3229–3235. (doi:10.1557/JMR.2008.0381)

85. Fuhrmann, T., Landwehr, S., El Rharbl-Kucki, M. & Sumper, M. 2004 Diatoms as living photonic crystals. *Appl. Phys. B Lasers Opt.* **78**, 257–260. (doi:10.1007/s00340-004-1419-4)

86. Cox, E. 2004 Pore occlusions in raphid diatoms - a reassessment of their structure and terminology, with particular reference to members of the Cymbellales. *Diatom* **20**, 33. (doi:10.11464/diatom1985.20.0_33)

87. Hildebrand, M., York, E., Kelz, J. I., Davis, A. K., Frigeri, L. G., Allison, D. P. & Doktycz, M. J. 2006 Nanoscale control of silica morphology and three-dimensional structure during diatom cell wall formation. *J. Mater. Res.* **21**, 2689–2698. (doi:10.1557/jmr.2006.0333)

88. Hasle, G. & Fryxell, G. 1970 Diatoms: cleaning and mounting for light and electron microscopy. *Trans. Am. Microsc. Soc.* **89**, 469–474. (doi:10.1126/science.35.895.309)

89. Ma, J. C. W. & Jeffrey, L. M. 1978 Description and comparison of a new cleaning method of diatom frustules for light and electron microscope studies. *J. Microsc.* **112**, 235–238. (doi:10.1111/j.1365-2818.1978.tb01170.x)

90. Stidolph, S. R. 2011 Coscinodiscus rothii. [cited 2014 Oct. 1] Available from: http://planktonnet.awi.de/index.php?contenttype=image_details&itemid=61009

91. Dass, R. & Devi, S. 2012 Image Segmentation Techniques. *Int. J. Electron. Commun. Technol.* **3**, 66–70.

92. Davies, E. R. 2012 *Computer & Machine Vision: Theory, Algorithms, Practicalities*. 4th edn. Oxford: Academic Press.

93. Sezgin, M. & Sankur, B. 2004 Survey over image thresholding techniques and quantitative performance evaluation. *J. Electron. Imaging* **13**, 146.

(doi:10.1117/1.1631315)

94. Sahoo, P., Soltani, S. & Wong, A. K. C. 1988 A survey of thresholding techniques. *Comput. Vision, Graph. Image Process.* **41**, 233–260. (doi:10.1016/0734-189X(88)90022-9)

95. de Berg, M., Cheong, O., van Kreveld, M. & Overmars, M. 2008 *Computational Geometry: Algorithms and Applications*. 3rd edn. Springer.

96. Aurenhammer, F. 1991 Voronoi Diagrams — A Survey of a Fundamental Data Structure. *ACM Comput. Surv.* **23**, 345–405. (doi:10.1145/116873.116880)

97. Kittel, C. 2004 *Introduction to solid state physics*. 8th edn. Wiley.

98. Kaplan, C. S. 2009 *Introductory tiling theory for computer graphics*. San Rafael: Morgan & Claypool Publishers.

99. Fryxell, G. A. & Ashworth, T. K. 1988 The Diatom Genus Coscinodiscus Ehrenberg: Characters Having Taxonomic Value. *Bot. Mar.* **31**, 359–374. (doi:10.1515/botm.1988.31.4.359)

100. Fernandes, L. F., Zehnder-Alves, L. & Bassfeld, J. C. 2001 The recently established diatom Coscinodiscus wailesii (Coscinodiscales, Bacillariophyta) in Brazilian waters. I: Remarks on morphology and distribution. *Phycol. Res.* **49**, 89–96. (doi:10.1046/j.1440-1835.2001.00226.x)

101. Sancetta, C. 1987 Three Species of Coscinodiscus Ehrenberg from North Pacific Sediments Examined in the Light and Scanning Electron Microscopes. *Micropaleontology* **33**, 230–241. (doi:10.2307/1485639)

102. Armbrust, E. V. et al. 2004 The genome of the diatom Thalassiosira pseudonana: ecology, evolution, and metabolism. *Science* **306**, 79–86. (doi:10.1126/science.1101156)

103. Mann, D. G. 1999 The species concept in diatoms. *Phycologia* **38**, 437–495. (doi:10.2216/i0031-8884-38-6-437.1)

104. Sar, E. A., Sunesen, I. & Jahn, R. 2010 Coscinodiscus perforatus revisited and compared with Coscinodiscus radiatus (Bacillariophyceae). *Phycologia* **49**, 514–524. (doi:10.2216/09-03.1)

105. Fritz, S. C., Juggins, S., Battarbee, R. W. & Engstrom, D. R. 1991 Reconstruction of past changes in salinity and climate using a diatom-based transfer function. *Nature* **352**, 706–708. (doi:10.1038/352706a0)

106. Cohn, S. A., Nash, J. & Pickett-Heaps, J. D. 1989 The effect of drugs on diatom valve morphogenesis. *Protoplasma* **149**, 130–143. (doi:10.1007/BF01322985)

107. Schmid, A. M. & Volcani, B. E. 1983 Wall morphogenesis in Coscinodiscus wailesii gran and angst. *J. Phycol.* **19**, 387–402. (doi:10.1111/j.0022-3646.1983.00387.x)

108. Falasco, E., Bona, F., Ginepro, M., Hlúbiková, D., Hoffmann, L. & Ector, L. 2009 Morphological abnormalities of diatom silica walls in relation to heavy metal contamination and artificial growth conditions. *Water SA* **35**, 595–606. (doi:10.4314/wsa.v35i5.49185)

109. Kieu, K., Mehravar, S., Gowda, R., Norwood, R. A. & Peyghambarian, N. 2013 Label-free multi-photon imaging using a compact femtosecond fiber laser mode-locked by carbon nanotube saturable absorber. *Biomed. Opt. Express* **4**, 2187. (doi:10.1364/BOE.4.002187)

110. Michels, J. 2013 Confocal Laser Scanning Microscopy – Detailed Three-Dimensional Morphological Imaging of Marine Organisms. In *Imaging Marine Life: Macrophotography and Microscopy Approaches for Marine Biology* (ed E. G. Reynaud), pp. 68–91. Wiley-VCH Verlag GmbH & Co. KGaA. (doi:10.1002/9783527675418.ch4)

111. Kucki, M. & Fuhrmann-Lieker, T. 2012 Staining diatoms with rhodamine dyes: control of emission colour in photonic biocomposites. *J. R. Soc. Interface* **9**, 727–33. (doi:10.1098/rsif.2011.0424)

112. Hale, M. S. & Mitchell, J. G. 2001 Functional morphology of diatom frustule microstructures: Hydrodynamic control of brownian particle diffusion and advection. *Aquat. Microb. Ecol.* **24**, 287–295. (doi:10.3354/ame024287)

113. Painter, O., Vučkovič, J. & Scherer, a. 1999 Defect modes of a two-dimensional photonic crystal in an optically thin dielectric slab. *J. Opt. Soc. Am. B* **16**, 275. (doi:10.1364/JOSAB.16.000275)

114. Sekoguchi, H., Takahashi, Y., Asano, T. & Noda, S. 2014 Photonic crystal nanocavity with a Q-factor of ~9 million. *Opt. Express* **22**, 916–924. (doi:10.1364/OE.22.000916)

115. Yablonovitch, E. 1993 Photonic band-gap structures. *J. Opt. Soc. Am. B* **10**, 283. (doi:10.1364/JOSAB.10.000283)

116. Joannopoulos, J. ., Villeneuve, P. R. & Fan, S. 1997 Photonic crystals:putting a new twist on light. *Nature*. **386**, 7. (doi:10.1038/386143a0)

117. Tyo, J. S. & Alenin, A. S. 2015 *Field guide to linear systems in optics*. SPIE.

118. Schneider, J. B. 2010 Understanding the Finite-Difference Time-Domain Method Title. [cited 2015 Jan. 2] Available from: www.eecs.wsu.edu/~schneidj/ufdtd